NASA/CR—1998–206893

High Energy Particle Acceleration and Turbulent Magnetic Field Amplification in Shell-Type Supernova Remnants

A Thesis Submitted to the Faculty of the Graduate School of the University of Minnesota

Jonathan Wilmore Keohane

Laboratory for High Energy Astrophysics

National Aeronautics and
Space Administration

Goddard Space Flight Center
Greenbelt, Maryland 20771

July 1998

Available from:

NASA Center for AeroSpace Information
7121 Standard Drive
Hanover, MD 21076–1320
Price Code: A17

National Technical Information Service
5285 Port Royal Road
Springfield, VA 22161
Price Code: A10

High Energy Particle Acceleration and Turbulent Magnetic Field Amplification in Shell-Type Supernova Remnants

A THESIS

SUBMITTED TO THE FACULTY OF THE GRADUATE SCHOOL

OF THE UNIVERSITY OF MINNESOTA

BY

Jonathan Wilmore Keohane

IN PARTIAL FULFILLMENT OF THE REQUIREMENTS

FOR THE DEGREE OF

DOCTOR OF PHILOSOPHY

July 1998

Preface

My hope is that this thesis is *academic* in the positive sense of the word, without the pejorative connotation. With this goal in mind, I have attempted to investigate topics or relevance to the broader astronomical community, and I have provided a summary of my most general conclusions on page 7. I have also created an index for quick reference and have made every effort to include my work *as published*, so that the reader clearly knows how to cite it.

Jonathan Keohane

July 6, 1998

Acknowledgements

I would like to begin by thanking my peers in the Astronomy Department at the University of Minnesota, including Martha Anderson, Bish Ishibashi, Debora Katz-Stone, Chip Kobulnicky, Barron Koralesky, and especially Allie Cliffe who carefully read this thesis. I appreciate all the help I received from Iona Quesnell and Terry Foley. I wish to thank my thesis committee, including Fred Finley, Roger Johnson, Terry Jones and especially Tom Jones for serving as chair. And last but not least, Larry Rudnick who taught me how to be a scientist.

Thanks to Steve Holt for visiting Minnesota, and encouraging me to pursue X-ray astronomy at Goddard Space Flight Center. And thanks to Glenn Allen, Keith Arnaud, Matthew Baring, Kazik Borkowski, Eric Gotthelf, Don Horner, K.D. Kuntz, Jim Lochner, Craig Markwardt, Richard Mushotzky, Andy Ptak, Jeonghee Rho, Samar Safi-Harb, Robin Shelton, Steve Sturner, T-club and everyone else I have worked with at Goddard. And thanks especially to Rob Petre, my thesis advisor, who has always given me both the resources, and the freedom, to conduct my own research.

I would also like to thank those members of the supernova remnant community who have taken an interest in my work and provided me with their insight, including John Dickel, Miller Goss, and Namir Kassim. And I especially want to thank Steve Reynolds, who introduced me to the issue of X-ray synchrotron radiation, and who has always been willing to give me excellent advice and constructive criticism.

In addition to my astronomical colleagues, I would like to thank David Green and

Ted Oakley for making high school physics teaching something I would want to return to, and John Kolena for his help in figuring this out and making it happen.

Finally I want to thank my entire family, including my sister and brothers, Sarah, Stephan and Nat, and my parents, Ann, Bob and Nan, who, along with my grandmothers, understood and fostered my strange scientific curiosity. And most of all, I want to thank my two energetic children, Jacob and Ike, and my wife, Laura, for all her love and support.

Dedication

To Laura, Jacob and Ike

Table of Contents

List of Tables

List of Figures

Chapter 1

Introduction

1.1 What is a Supernova Remnant?

One of the most energetic explosive events known is a supernova (SN),* of which there are two physical types (type I & type II).†

Type I supernovae (SNe) are believed to occur in binary star systems, where mass flows from a red giant star to its white dwarf companion. As matter flows onto the white dwarf, its mass grows until it reaches about the Chandrasekhar mass ($1.4\,M_{\odot}$). At this point thermonuclear runaway occurs and about 10^{51} ergs (10^{28} mega-tons) of energy is released — mostly in the form of kinetic energy.

A type II SN, on the other hand, occurs at the end of a massive ($M>8\,M_{\odot}$) star's lifetime when its nuclear fuel is exhausted and its core is no longer supported by the release of nuclear energy — and thus collapses under the force of gravity. When the core collapses, approximately 10^{53} ergs of total energy is released; about 99% of this

*A good introduction to SNe for the non-astronomer is Marschall (1988), while a good review of research on the physics of SNe is Woosley & Weaver (1986). Information in this introduction was taken from both sources.

†Here we will use the physical definition of type I and type II. Here, type I corresponds to observational type Ia, while type II indicates observational types Ib, Ic and II.

energy is in the form of neutrinos. These neutrinos largely do not interact with matter, so they escape without affecting the material surrounding the SN. Despite containing only 1% of the total gravitational energy, the energy contained in the expanding material is nevertheless enormous, having about 10^{51} ergs of energy (coincidentally about the same as a type I SN). This explosion will generate a shock which will first plow through the the star's atmosphere, then the circumstellar material and finally into the interstellar medium (ISM).

While many SNe have been seen in nearby galaxies, they are relatively rare events in our Galaxy, occurring once a century or so on average.[‡] The last nearby SN (Cas A) was observed by John Flamsteed in 1680, but it was thought to be a star at the time and caused a discrepancy in the observer's star catalogue which historians only later resolved (Ashworth 1980). The two just before that were observed by the astronomers Tycho and Kepler in 1572 and 1604 respectively (Brahe 1573; Kepler 1606). In addition, Asian astronomers observed many "guest stars," some of which are thought to have been supernovae (e.g., SN 386, SN 393, SN 1006, SN 1054, SN 1181)[§]

SNe are one of the most important elements of the ecology of our Galaxy, supplying the primary source of metals and turbulent energy to the ISM. SNe not only disperse the elements made in stars, but also synthesize elements, including those elements which are produced through endothermic nuclear processes (such as all elements heavier than iron). In addition, SNe provide the most significant source of kinetic energy to the Galaxy (at a rate of $\sim 10^{51}$ ergs per century), which goes into heating and stirring the ISM — as well as accelerating cosmic rays.

Once the shock wave created by the SN interacts significantly with the surrounding medium, it becomes known as a supernova remnant (SNR). SNRs are sorted into the

---

[‡]Within the whole Milky Way, SNe most likely occur more often. However, obscuration by dust can cause many to have been missed.

[§]The classic book on the historical supernovae is Clark & Stephenson (1977).

following basic categories:

Shell type remnants These SNRs appear more-or-less circular on the sky. As the shock wave from the SN explosion plows through space, any interstellar material it encounters becomes swept up, heated and stirred up – thus producing an expanding shell of hot material in space. We see the ring-like structure because of classic limb brightening: when we look at the edge of the shell there is a longer path-length of luminous gas along our line of sight than when we look through the middle. (e.g., Cas A, Tycho & Kepler).

Plerions These SNRs contain a central pulsar whose jets of very fast moving material interact with the surrounding SNR. These remnants look more like a "blob" than a "ring," in both the radio and X-ray. Plerions exhibit fairly flat radio spectral indicies[¶] ($\alpha \lesssim 0.3$), high radio polarization and non-thermal X-ray spectra (e.g., the Crab Nebula and 3C58).

Composite Remnants These remnants contain both a shell and a central plerion. Often a SNR will be classified as shell-type based on its radio and soft X-ray morphology, but a hidden central plerion will become revealed in the hard X-ray (e.g., SN 386, see p. 92).

Mixed-Morphology SNRs These SNRs are classified as shell-type SNRs in the radio, however they appear center-filled in the X-ray. The central X-rays are usually dominated by soft thermal emission (e.g., IC 443, see chapter 8).

While pulsar/SNR interactions are interesting for the study of matter in extreme conditions, they affect the Milky way less than the SNR shock. To avoid the added

---

[¶]In this thesis, we define the spectral index, α, such that $S_\nu \propto \nu^{-\alpha}$, where S_ν is the energy flux density. The photon index, Γ, is similarly defined such that $F_E \propto E^{-\Gamma}$, where $E = h\nu$ and F_E is the photon flux density. Therefore, $\Gamma = \alpha + 1$. In addition we use γ as the electron index (i.e., $N_e \propto E_e^{-\gamma}$). Therefore, $\alpha = \frac{\gamma-1}{2}$ and $\Gamma = \frac{\gamma+1}{2}$.

complications associated with pulsars, this thesis will concentrate on those SNRs which are classified as shell-type from radio observations (i.e., in Green's catalogue), regardless of their X-ray morphology.

In particular, we will use X-ray and radio observations of individual shell-type SNRs to investigate broader issues in modern astrophysics, including:

- the amplification of magnetic fields in a turbulent medium (PART I)
- the origin of cosmic rays and the physics of particle acceleration (PART II)

1.2 Thesis Overview

1.2.1 PART I: The Striking X-ray and Radio Correlation of Cas A

In PART I of this thesis, we discuss the spatial correlation between the X-ray and radio morphologies of Cas A, and in the process address a few issues concerning our Galaxy's youngest known SNR. These issues include:

- the effect of inhomogeneous absorption on the apparent X-ray morphology
- the interaction between the SNR and a molecular cloud
- the rapid move toward equipartition between the magnetic and gas energy densities

Cas A's high radio and X-ray flux has made it a useful background source for investigating the ISM. In chapter 3, I compare three existing absorption maps of Cas A: H I, OH and X-ray (ASCA). From these we estimate the ratio of of OH to H_2, and thus calibrate the abundances of a number of molecular species in the ISM.

These absorption studies reveal a strong gradient across the face of Cas A, with a particularly opaque molecular cloud covering the radio bright western edge. In chapter 4

we show that when this absorption is taken into account, the gross X-ray morphology becomes better correlated with the radio.

It is not simply a coincidence that the brightest region of Cas A is also the side blocked by a molecular cloud. By comparing radio proper motion studies (Anderson & Rudnick 1995; Rudnick et al. 1996) and foreground absorption, this thesis suggests (§4.3.2) that the the same cloud which is absorbing the western edge of the SNR, is also physically interacting with Cas A.

Discussion of the X-ray/radio correlation continues in chapter 5, where we present a new, deep, ROSAT HRI image of Cas A. These high quality data allow us to measure the X-ray/radio correlation on scales down to 4″ (0.07 pc), which remains remarkably good. We argue that this is evidence for proportionate partition[‖] between the magnetic field and the X-ray emitting plasma on small scales — which is what one would expect for a fully turbulent plasma.

1.2.2 PART II: X-ray Synchrotron Radiation

The Evidence for X-ray Synchrotron Radiation

Electrons of 1–100 TeV energies, interacting with a typical magnetic field, produce X-ray synchrotron radiation (see p. 68). SNRs are believed to produce the bulk of cosmic rays up to the "knee" at about 1,000 TeV,[*] so observing TeV electrons within SNRs would support this idea.

The evidence that the supernova of 1006 AD is dominated by synchrotron radiation is now overwhelming (see p. 72). SN 1006 appears to be highly unusual,[†] not because

---

[‖]We use the term *proportionate partition* to mean that the magnetic and gas pressures are proportional to each other ($B^2 \propto U_{\rm gas} \propto n_{\rm gas}$) — see page 60.

[*]At about 1,000 TeV the cosmic ray spectrum slightly steepens (see p. 65). This is called the "knee," and is shown in the figure on page 66.

[†]As is also mentioned in §6.2.2 (p. 72), there is now a second example of a synchrotron dominated historical SNR — SN 393.

of its strong synchrotron emission (it is not extremely bright), but because of its weak thermal line emission. In other words, if the younger historical shell SNRs (Tycho, Kepler, Cas A) contained X-ray to radio synchrotron continua similar to SN 1006, their strong emission lines would still dominate their X-ray spectra (see Tab. 7.28, p 125).

Chapter 6 introduces the topic of X-ray synchrotron radiation from SNR shells, and investigates evidence for it in a few cases. The approach taken in chapter 6 assumes that thermal models are more-or-less correct, and looks for excess hard emission using ASCA GIS data. This is a similar technique to that used by Petre et al. (1997) for SNRs in the Large Magellanic Cloud.

The application of this technique for distinguishing synchrotron radiation from thermal radiation has not been wholly successful. Thermal models, in general, can be applied to any ASCA spectrum which contains lines. ASCA's spectra, by themselves, can investigate the plausibility of a non-thermal spectral component, but they cannot prove or rule out a significant synchrotron continuum. A harder passband is needed, as is reviewed in §6.2.3 (p. 72).

Upper Limits on X-ray Synchrotron Radiation

As mentioned above, ASCA spectra cannot definitively distinguish synchrotron radiation from thermal radiation. In chapter 6 we assume that the continuum is primarily thermal, and look for a necessary additional component. Chapter 7 takes the opposite approach; we assume that the continuum is primarily synchrotron radiation, and interpret the results as upper limits. One advantage of this approach is that model synchrotron spectra are already well constrained by the radio flux and spectral index. While thermal models have at least two parameters which affect the shape and flux level of the X-ray continuum, the synchrotron model used in chapter 7 has only one free parameter.

Chapter 7 presents ASCA spectra, with non-thermal spectral fits for 13 of the

youngest SNRs in the Galaxy. Some of these spectra are well fit by synchrotron models, which hints that their continua may have a significant non-thermal component. Other SNRs, however, require additional continuum components and still show a poor fit. In all cases, upper limits are found to the flux of the X-ray synchrotron spectral component. These upper limits constrain the radio to X-ray roll-off frequencies,[‡] which, in turn, constrain the maximum energy of the cosmic ray electrons within each SNR (see p. 125). This maximum electron energy is typically between 10 TeV and 100 TeV, which is 1-2 decades below the knee in the cosmic ray spectrum.

The Supernova Remnant IC 443

Unlike the smaller historical SNRs, IC 443's size ($\lesssim 1°$) makes it a perfect candidate for ASCA's spatially resolved spectroscopy. Using ASCA, we have discovered spatially distinct regions of hard X-ray continuum (chapter 8). We argue that these features are X-ray synchrotron emission from a region of enhanced cosmic ray acceleration due to the interaction of the SN shock wave with the surrounding molecular cloud structure.

1.3 The Broader Implications of this Work

Out of the work presented here, a few generalizations arose. These conclusions are summed up in the following four points:

1. SNRs are often modeled with simple 1 D hydrodynamics, assuming a homogeneous ISM. This is known to be simplistic, but it is also assumed to be a reasonable approximation. It is not — at least in the case of Cas A. Core-collapse SNR go through a turbulent phase (which Cas A is in now), where their magnetic field is significantly enhanced. A new breed of turbulent models needs to be worked out, which are simple to use, yet qualitatively correct. (chapter 5)

[‡]The model used in chapter 7 is the maximally curved extreme case. Thus, even if all the continuum emission is synchrotron, the model still puts only an upper limit on the maximum electron energy.

2. X-ray spectra from most young shell-type SNRs reveal strong emission lines. X-ray astronomers usually assume that because line emission exists, the continuum is entirely thermal. This is naive. Physical parameters resulting from such assumptions for young SNRs, such as abundance measurements,[§] should be interpreted as limiting cases only. (chapter 6)

3. SNRs have long been known to accelerate cosmic rays up to GeV range energies. They are generally assumed to produce the majority of Galactic cosmic rays with energies below the knee in the cosmic ray spectrum. The origin of higher energy cosmic rays is more speculative, but young core-collapse SNRs are a common explanation for CRs to energies as high as 10^{18} eV. This is not so, at least for electrons. Some young shell-type SNRs can accelerate particles up to the 10^{14} eV range, but they do not accelerate electrons to higher energies. In short, SNRs are still the most likely source of CRs up to the "knee," but no further. (chapter 7)

4. Finding hard X-ray compact objects within SNRs has become a "cottage industry" since the launch of ASCA. Many of these sources have been shown to be pulsars, or other compact objects, through timing analysis. On the other hand, many have not. Perhaps most of these hard features are pulsars, but it is naive to assume that all are compact objects. The interaction between shocks and clouds can produce a whole suite of possible structures, including hard tails from localized regions. (chapter 8)

[§]If part of the continuum is non-thermal, line equivalent widths will be under-estimated. This will usually result in too low chemical abundance measurements.

Part I

The Striking X-ray and Radio Correlation of Cassiopeia A

Chapter 2

Introduction to PART I

2.1 Introduction

Cassiopeia A (Cas A) is the natural starting point for a study of astrophysical fluid dynamics and particle acceleration for a number of reasons. Cas A is the youngest (1680 A.D., Ashworth 1980) and brightest* SNR, so it has been well observed and is often considered the canonical young SNR. The question of whether Cas A is typical is best answered through comparative studies with extragalactic supernova remnants (e.g., Lacey, Duric, & Goss 1997). At any rate, a few fundamental issues regarding Cas A (such as its basic structure) need to be resolved before we can obtain a complete understanding of young supernova remnants.

*With a 1 GHz flux density of 2720 Jy, Cas A is the brightest object outside the solar system in the radio sky.

2.2 Cas A's Soft X-ray Emission & Absorption

X-ray emission from shell-like SNRs is primarily thermal in nature, so it traces hot ($kT \approx 1\,\mathrm{keV}$) gas that has been recently shocked.[†] Therefore, X-rays are the most indicative observable characteristic of the SNR's basic hydrodynamic structure. X-ray observations are often limited by the "catch 22" that cameras have limited spectral resolution, while spectrometers have limited spatial resolution[‡]. Because the effective X-ray absorption cross-section[§] is a function of photon energy, one can interpret X-ray "color" variations as either due to temperature or foreground column density (N_{H})[¶] variations. Therefore, images of extended objects close to the Galactic plane, as Galactic SNRs generally are, are sometimes significantly altered by interstellar absorption, thus leading to incorrect interpretations. It is possible, however, to distinguish variations in column density from those in temperature using an X-ray spectrometer.

Using the EINSTEIN observatory, Fabian et al. (1980) imaged Cas A with the IPC instrument, and noticed a significant difference between the hardness of photons in the western and eastern portions of the remnant. Acknowledging that both temperature and absorption differences across the remnant would explain the observed phenomenon, they nevertheless calculated the temperature structure of the remnant assuming uniform absorption. The assumption of uniform absorption had been made by every X-ray morphology paper about Cas A until Jansen et al. (1988) used 1979 H I WSRT data

---

[†]In soft X-rays, most shell-type SNRs are line dominated. The strengths of particular lines are complex functions of the hydrodynamics and chemistry of the particular SNR involved. However the hot gas is collisionally excited, so the intensity of broad-band soft X-rays is proportional to the density squared. Appendix B shows a number of model X-ray spectra which show the line-dominated soft X-ray emission.

[‡]With the Solid State Imaging Spectrometer (SIS) on ASCA, high resolution spectra can be imaged to about $1'$ resolution. However, rarely does one obtain a long enough exposure to create accurate spatially resolved spectra.

[§]The effective cross-section of X-ray absorption per hydrogen atom. Unlike in the optical, the harder the X-rays, the smaller the effective cross-section. The majority of X-rays are not absorbed by hydrogen, but rather by inner-shell transitions of metals such as Carbon, Nitrogen and Oxygen.

[¶]N_{H} represents the total column density of hydrogen. Neglecting H II, $N_{\mathrm{H}} = N_{\mathrm{H\,I}} + N_{\mathrm{H}_2}$.

(Schwarz, Goss, & Kalberla 1997) to independently correct EXOSAT data to obtain the temperature structure to $1'$ resolution. Unfortunately, the true structure was still unrevealed, because subsequent molecular absorption work found that the primary $N_{\rm H}$ variations toward Cas A are caused by molecular clouds (Batrla, Walmsley, & Wilson 1984; Bieging & Crutcher 1986; Bieging, Goss, & Wilcots 1991; Gaume, Wilson, & Johnston 1994), which are not traced by λ21 cm observations.[‖]

In chapter 4, a ROSAT HRI image of Cas A is deabsorbed using not only the $30''$ resolution H I data of Schwarz, Goss, & Kalberla (1997), but also including the molecular component as observed in OH absorption data by Bieging & Crutcher (1986) with the VLA. By correcting for all the absorption components, we have obtained the first morphologically correct map of the soft X-ray emission from Cas A. In chapter 5 a much deeper ROSAT HRI image of Cas A is deabsorbed in the same manner as in chapter 4. When in conflict chapter 5 supersedes chapter 4.

2.3 Radio and X-ray Comparisons

Synchrotron radiation has long been known to dominate the radio spectra of SNRs, primarily because of the polarized emission and steep power-law spectra. Therefore, the radio surface brightness is a function of the density of relativistic electrons and the magnetic field strength. By spatially comparing the radio and X-ray emission, we can probe the correlation between the magnetic field strength and the hot gas structure.

Dickel et al. (1982) compared the X-ray (EINSTEIN HRI) and radio surface brightness of Cas A and Tycho. They found a higher degree of correlation in Cas A than Tycho. Later, Braun (1987) compared $2'$ resolution maps of X-ray, optical, IR and radio of Cas A, Tycho and Kepler. Even though the Cas A X-ray and radio maps have gross morphological differences, they appear much more similar to each other than to

[‖]Not only do λ21 cm observations not trace the molecular species, but they are not correlated with them either.

either the optical or IR maps. In addition, the X-ray and radio radial profiles peak at the same location, and look surprisingly similar. Therefore, it was clear that some sort of correlation between the X-ray and radio exists, but it was also clear that there were significant differences as well.

By comparing corrected 30″ (Chapter 4) and 4″ (Chapter 5) resolution X-ray and radio maps of Cas A, we find a tighter correlation than was previously observed. In chapter 5 we repeat the analysis discussed in chapter 4, but with a much deeper image of Cas A. This new image reveals a good correlation on small scales, with a very tight constraint on the slope of the log-log correlation. This log-log slope is consistent with the hot gas and magnetic field pressures being in proportionate partition* on small scales.

2.4 Impact on Theoretical Models

The field of astrophysical fluid dynamics is flourishing. There are many complex computer codes which are able to simulate a host of phenomena (e.g., binary stars, jets, supernovae). However, realistic modeling of any of these phenomena requires a great deal of computer time and is therefore prohibitively expensive. Even very simple, purely hydrodynamic, and inherently symmetrical systems show significant qualitative differences when computed on fine grid scales (e.g., Bassett & Woodward 1995), or using a fully 3D computer code. These effects are compounded greatly when one simulates a complex three dimensional object and especially when including other dynamically important processes such as magnetic fields. For these reasons, theoretical studies of complex objects must make simplifying assumptions in order to produce results. Unfortunately, it is not always clear which simplifying assumptions will cause the simulation to deviate significantly from reality, and which are less important.

---

*We use the term *proportionate partition* to mean that the magnetic and gas pressures are proportional to each other ($B^2 \propto U_{\rm gas} \propto n_{\rm gas}$) — see page 60.

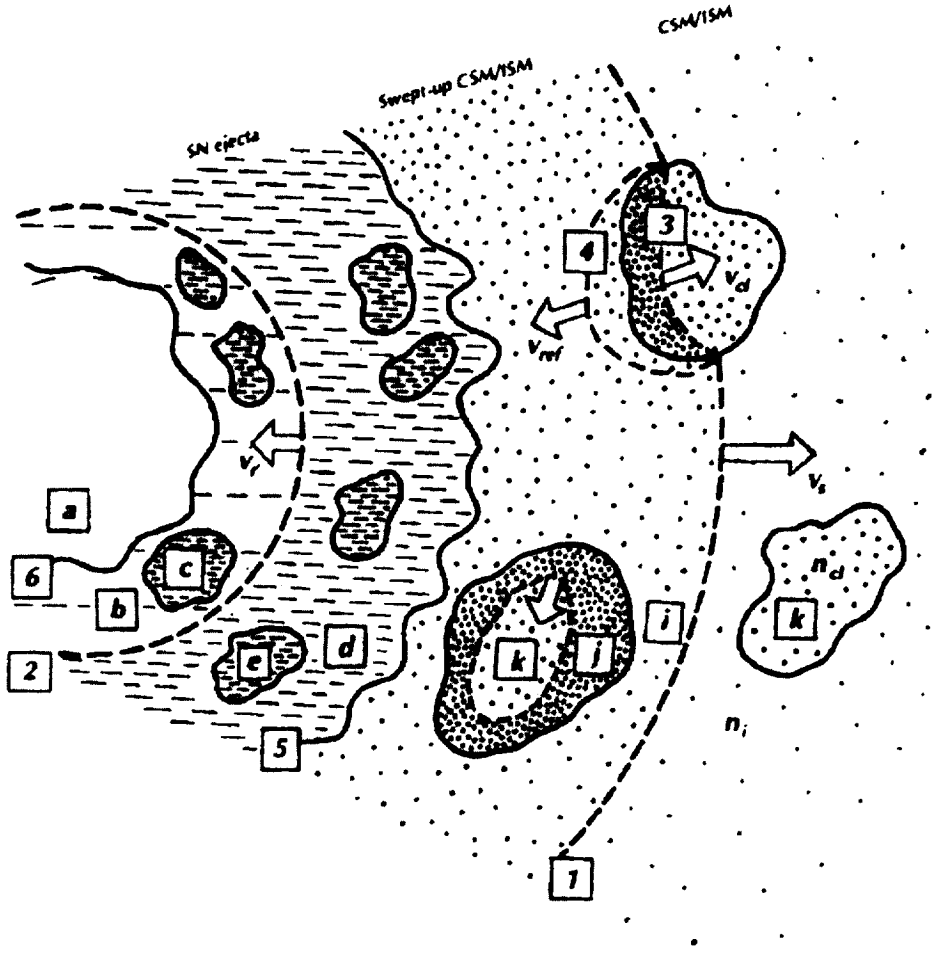

Figure 2.1: Sketch of a young SNR (from Fig. 47 of Lozinskaya 1992). Selected labels are: 1) blast wave propagating into ISM; 2) reverse shock; 3) secondary shock wave moving in dense cloud; 4) shock reflected off of a cloud; 5) contact discontinuity between swept-up gas and SN ejecta. For additional details about this figure, we refer the reader to page 191 of Lozinskaya.

In the standard cartoon picture of a young supernova remnant (illustrated in figure 2.4), the supersonic ejecta are usually modeled as a piston driving a shock front (label 1) radially outward. In this picture, a reverse shock forms (label 2) and propagates through the ejecta. Because the SNR then consists of both hot gas just behind the fore-shock, and slightly cooler gas heated by the reverse shock, a contact discontinuity (label 5) forms between the two plasmas.

This cartoon picture is overly simplistic for a number of reasons, particularly that the contact discontinuity is Rayleigh-Taylor (R-T) unstable.[†] Fingers of dense material protrude out into the less dense hot material, causing mixing and turbulence in the vicinity of the contact discontinuity. By applying the standard assumption that the magnetic field lines are "frozen in" to the plasma, one can see how this turbulence could quickly stretch, wrap around and amplify the magnetic field. Thus, one expects the bright radio ring to represent the contact discontinuity region.[‡] By assuming that the magnetic field and relativistic electrons are in large scale equipartition, Gull (1973b,a), reproduced approximate radio and X-ray luminosities of Cas A and Tycho by using a reasonable set of initial parameters, and a very simple model. Since Gull's 1973 papers, great advances in the sophistication of hydrodynamic codes and computer speed has enabled detailed modeling of the R-T instability at the contact discontinuity. Jun, Norman, & Stone (1995) used MHD simulations to study magnetic field magnification at the contact discontinuity. They concluded that the R-T instability is sped up by making the primarily radial field dynamically important, thus adding to the R-T mixing and field line stretching. From an MHD model (like Jun's), magnetic field strengths

[†]The whole mass is decelerating, and the inside gas is more dense then the hot outside gas (constant pressure across contact discontinuities). This is similar to when a heavy fluid sits on top of a lighter fluid – they try to exchange places.

[‡]This naturally assumes that the magnetic field, not the relativistic electron density, determines the radio morphology. This is most likely true for Cas A.

are calculated in addition to the standard hydrodynamic variables. Therefore, by assuming a uniform distribution of relativistic electrons, the radio and the X-ray surface brightness can be modeled.

The more and more complex computer codes (i.e., high resolution MHD codes) used to simulate young SNRs are one of the most powerful tools currently available to study SNRs, however they are too cumbersome for wide-spread use. If, on the other hand, full turbulence can be assumed, the system becomes simpler overall. Following each fluid element still requires enormous computer power, but the cascade of energy from large to small scales is now a well-defined phenomenon. The observations presented in this PART supports this assumption of turbulence.

The X-ray/radio correlation discussed in chapters 4 & 5 is extremely good — especially with the highest angular resolution. We conclude in chapter 5 that the magnetic field is amplified toward equipartition with the thermal plasma on the smallest scales. So, simply because of the pervasive turbulence, the X-ray and radio emission is highly correlated.

Chapter 3

Measuring Molecular Abundances of the Interstellar Medium in the Direction of Cassiopeia A by Comparing X-ray and Radio Absorption Studies

Published in **Cosmic Abundances**: *Proceedings of the Sixth Annual October Astrophysics Conference in College park, Maryland on 9-11 October 1995 as Keohane, J.W.*

ASCA derived column densities are compared with λ21 cm H I and λ18 cm OH optical depths in the direction of Cas A. The H I spin temperature and the ratio N_{OH}/N_{H_2} are measured. Revised abundance ratios are calculated for the molecules: ^{13}CO, ^{12}CO, H_2CO and NH_3.

Subject headings: ISM: clouds, atoms, molecules, supernova remnants, individual: Cas A — radio lines: ISM — X-rays: ISM

3.1 Introduction

Using Cas A as a background source, the interstellar medium has been well-studied in radio absorption. A high resolution (7″) VLA λ21 cm absorption study of the Perseus arm velocity feature was carried out by Bieging, Goss and Wilcots (1991). 30″ resolution H I absorption data over a wider velocity range were obtained by Goss and collaborators with the Westerbork array (Schwarz et al. 1995, hereafter SGK). In addition there have been numerous molecular absorption studies — in H_2CO (Goss et al. 1984), in CO (Wilson et al. 1993, hereafter WMMPO), NH_3 (Batrla et al. 1984 and Gaume et al. 1994) and OH (Bieging & Crutcher 1986, hereafter BC). The absorption patterns in the various *molecules* are similar to each other, but very different than that of the H I .

(Rasmussen 1996, hereafter R96) studied the spatial dependence of X-ray model parameters using the ASCA satellite, resulting in a total column density (N_H) map. In this paper, we compare the radio absorption data of BC and SGK to the N_H map of R96. From this we measure the scaling relation between column density and equivalent line widths from the radio absorption measurements of SGK and BC. This allows measurements of the average H I spin temperature and the N_{OH}/N_{H_2} abundance of the ISM to be calculated.

3.2 Analysis

In order to measure the column density (N_H) toward Cas A, we found the equivalent widths ($EW \equiv \int \tau dV$) of the H I and OH absorption measurements of SGK and BC respectively. The total column density can then be given by the relation:

$$N_{\mathrm{H_{Radio}}} = D\,(EW_{\mathrm{HI}}) + E\,(EW_{\mathrm{OH}}) + F$$

where the column density is measured in units of $10^{22}\mathrm{cm}^{-2}$ and the equivalent widths are measured in km/s. The goal of this analysis is to measure the parameters D, E and F.

In order to match the resolution of SGK's data, we smoothed BC's line and continuum maps to a resolution of 30″, before calculating the optical depths and equivalent widths. This resulted in our obtaining 30″ images of EW_{HI} and EW_{OH}, as well as their respective error maps calculated using standard methods.

R96 performed spatially resolved spectral fits to the 0.5–12 keV ASCA data, resulting in independently derived column density maps from those discussed above. Spectral fitting works very well to find the total column density towards an X-ray source, because the effective X-ray cross-section is a strong and unique function of photon energy (Morrison & McCammon 1983). The images are shown in figure 3.1 on page 23.

The position of the ASCA field was aligned with our radio images by maximizing the cross-correlation of R96's $N_{\mathrm{H_{ASCA}}}$ image with the radio absorption using an initial estimate of parameters D and E.

Because an error image was not provided by R96, we were unable to calculate true χ^2 differences. We, therefore, defined our reduced χ^2 such that:

$$\chi^2_{\mathrm{reduced}}(D,E,F) \equiv \frac{\sum (N_{\mathrm{H_{ASCA}}} - N_{\mathrm{H_{Radio}}})^2}{\min\left(\sum (N_{\mathrm{H_{ASCA}}} - N_{\mathrm{H_{Radio}}})^2\right)}$$

The best fit values for parameters D,E and F are: $(7.1 \pm 3.8) \times 10^{-3}$, 0.213 ± 0.141, and 0.69 ± 0.19 respectively (70% confidence); the χ^2 dependence on D,E and F is shown

in figure 4.5 on page 36. There were 25 independent beams (22 degrees of freedom).

3.3 Discussion

The column densities of H I and OH are given by the following equations:

$$N_{\rm HI} = \left(1.83 \times 10^{-4}\ EW_{\rm HI}\right)\left(\frac{T_{\rm spin}}{^\circ{\rm K}}\right) \times 10^{22}{\rm cm}^{-2}$$
$$N_{\rm OH} = \left(2.2 \times 10^{-8}\ EW_{\rm OH}\right)\left(\frac{T_{\rm ex}}{^\circ{\rm K}}\right) \times 10^{22}{\rm cm}^{-2}$$

Therefore the average spin temperature of the H I that SGK measured should be given by

$$T_{\rm spin} = D/(1.83 \times 10^{-4}) = (39 \pm 21)^\circ{\rm K}\,.$$

This is consistent with the previously estimated spin temperature of 60 °K which Kalberla, Schwarz, & Goss (1985) measured toward a different line of sight.

Figure 4.5 (p. 36) shows that there is very little correlation between parameter E and either parameter D or F. This implies that our best fit parameter E is robust. If we assume a molecular excitation temperature of $T_{\rm ex} = 20^\circ$K (WMMPO), we find the abundance of OH to be:

$$\frac{N_{OH}}{N_{H_2}} = (4.1 \pm 2.7) \times 10^{-6} \left(\frac{T_{\rm ex}}{20^\circ{\rm K}}\right)\,. \tag{3.1}$$

In WMMPO's CO study, they compare their data with the existing literature to find relative abundances of each molecular species studied up to that time. Because there have been no direct measurements of N_{H_2}, their abundances relative to H_2 are uncertain. We calculate new molecular abundances of the ISM using WMMPO's inter-species abundance ratios and the $^{12}{\rm C}/^{13}{\rm C}$ ratio of Penzias and Langer (1993) (see Tab. 3.1 on p. 22).

Species	N_X/N_{H_2}		
OH	4.1×10^{-6}	$\pm$	2.7×10^{-6}
^{13}CO	3.2×10^{-5}	$\pm$	2.5×10^{-5}
^{12}CO	2.0×10^{-3}	$\pm$	1.6×10^{-3}
H_2CO	2.1×10^{-7}	$\pm$	2.1×10^{-7}
NH_3	6.3×10^{-8}	$\pm$	6.2×10^{-8}

Table 3.1: The relative abundances of various molecular species assuming WMMPO's molecular excitation temperature ($T_{ex} = 20°K$) and their inter-species abundance ratios ($^{13}CO/H_2CO = 150 \pm 90$, $^{13}CO/OH = 7.7 \pm 3.3$, $^{13}CO/NH_3 = 500 \pm 300$ and $^{12}CO/^{13}CO = 62 \pm 4$). All values will scale directly with the OH excitation temperature.

3.4 Conclusion

By comparing X-ray and radio spectroscopic absorption measurements, the H I spin temperature and molecular abundances were measured. Future studies of Cas A and other radio and X-ray bright extended objects can significantly enhance our understanding of the ISM, by comparing spatially resolved column densities from either the ROSAT PSPC or ASCA with radio atomic and molecular line absorption data.

This work was supported, in part, by the NSF through grants AST-8720285 and AST-9100486. Funding was also provided by NASA/GSFC's Laboratory for High Energy Astrophysics through the Graduate Student Researchers Program. OH absorption data were kindly provided by John Bieging. H I absorption Westerbork data were kindly provided by W. Miller Goss. ASCA data were kindly provided by Andrew P. Rasmussen. I would also like to thank Lawrence Rudnick who contributed a good deal of advice regarding this work.

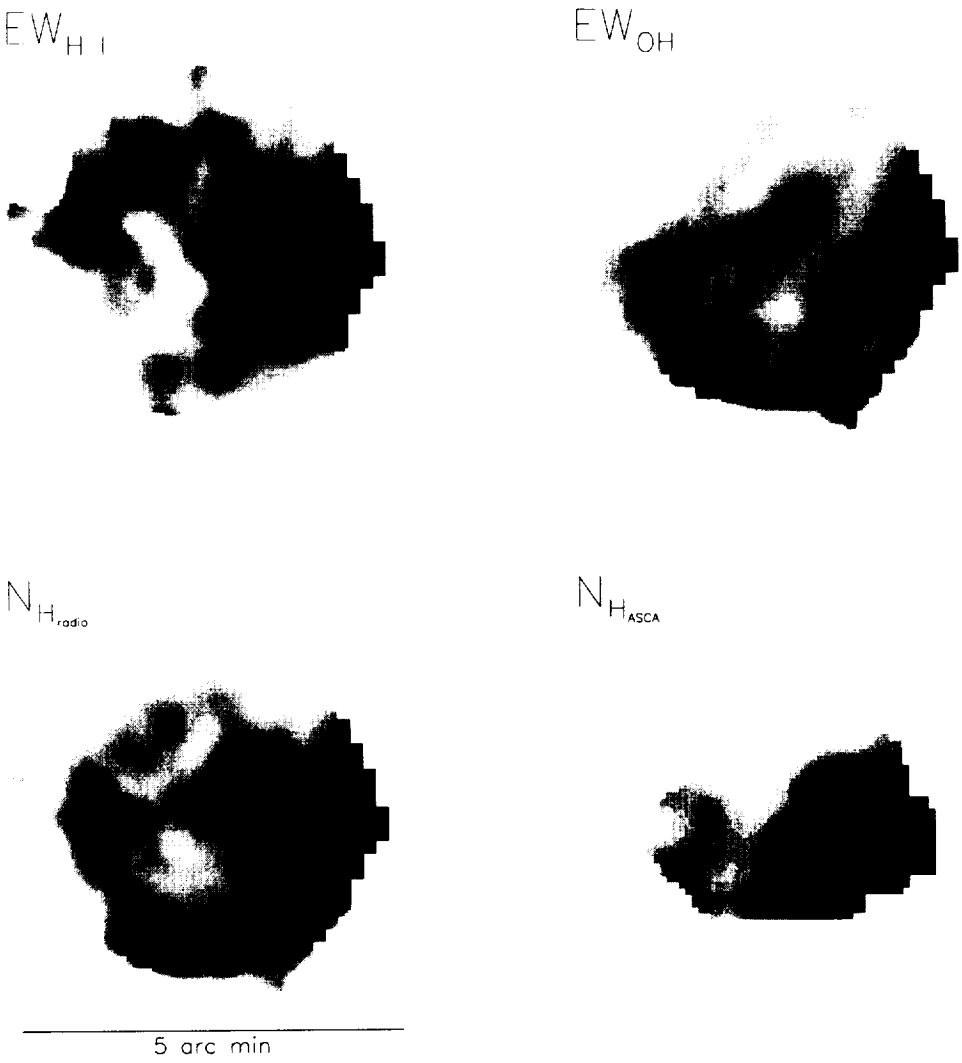

Figure 3.1: 30″ resolution images of ISM absorption toward Cas A.

Chapter 4

A Comparison of X-ray and Radio Emission from the Supernova Remnant Cassiopeia A

Published in the Astrophysical Journal as
Keohane, J.W., Rudnick, L. & Anderson, M.C.
(Vol. 466, pp. 309-316, July 20, 1996)

We compare the radio and soft X-ray brightness as a function of position within the young supernova remnant Cassiopeia A. A moderately strong correlation (r = 0.7) was found between the X-ray emission (corrected for interstellar absorption) and radio emission, showing that the thermal and

relativistic plasmas occupy the same volumes and are regulated by common underlying parameters. The logarithmic slope of the relationship, $\ln(S_{\rm X-ray}) = 1.2 \times \ln(S_{\rm radio}) + \ln(k)$ implies that the variations in brightness are primarily due to path length differences. The X-ray and radio emissivities are both high in the same general locations, but their more detailed relationship is poorly constrained and probably shows significant scatter.

The strongest radio and X-ray absorption is found at the western boundary of Cas A. Based on the properties of Cas A and the absorbing molecular cloud, we argue that they are physically interacting.

We also compare ASCA derived column densities with λ21 cm H I and λ18 cm OH optical depths in the direction of Cas A, in order to provide an independent estimate of ISM properties. We derive an average value for the H I spin temperature of $\approx 40°K$ and measure the ratio OH/H_2 , which is nominally larger than previous estimates.

Subject headings: ISM: clouds, atoms, molecules, supernova remnants, individual: Cas A — radio lines: ISM — X-rays: ISM — radio continuum: ISM

4.1 Introduction

The basic hydrodynamical structure of idealized young supernova remnants (SNRs) seems well-understood from a theoretical standpoint (Gull 1973b; Chevalier 1982). We expect to find an outer shock, a contact discontinuity between the shocked circumstellar medium and the ejecta, and a reverse shock moving into and decelerating the ejected material. Each of these should give rise to radio and X-ray radiation, with different emissivities depending on the local physical processes.

Observationally, the situation is far from this ideal. In the best studied young SNR, Cas A, none of these structures can be clearly identified (Anderson & Rudnick

1995, , hereafter A&R). There are also questions about the nature of the outer shock, where the expected tangential magnetic fields are not seen for Kepler and Tycho (e.g. Kepler & Tycho respectively — Dickel et al. 1989; Dickel, Van Breugel, & Strom 1991). Inhomogeneities on a variety of scales also complicate the observational as well as the theoretical pictures (e.g., Borkowski, Blondin, & Sarazin 1992; Cliffe & Jones 1994; Jun & Norman 1995).

We need to clarify the nature of actual SNR structures both to understand the hydrodynamics and also to begin addressing important physical issues such as magnetic field amplification and relativistic particle acceleration. Although reasonable theoretical mechanisms exist for these processes Gull (1973a); Reynolds & Ellison (1992), the observational signatures are far from clear (e.g., Anderson et al. 1994). One fruitful approach to addressing such questions may be a careful examination of the relationship between the X-ray and radio emissivities within a remnant, because of the different physical processes involved.

The bulk of the X-ray emission at low energies results from thermal line emission (Becker et al. 1979; Holt et al. 1994, hereafter HGTN) depending primarily on the temperature ($\approx$ 3 keV) and density ($\approx$ 10 cm^{-3}) of the plasma carrying most of the mass and momentum (Fabian et al. 1980, hereafter F80). On the other hand, the radio emission is synchrotron radiation from relativistic electrons ($\epsilon \approx 0.05 - 8$ GeV) in magnetic fields of $\approx 100\,\mu$G (Cowsik & Sarkar 1980). In one remnant, SN1006, X-ray synchrotron radiation is probably present at keV energies (Koyama et al. 1995), although this is an exceptional case.

Very little quantitative work has been done on the comparison of X-ray and radio emissivities in SNRs. The canonical wisdom is that the two are well-correlated on large scales, but show little correlation at smaller spatial scales (F80; Matsui et al. 1984, hereafter MLDG). MLDG studied these relations in Kepler, where they divided the remnant into twelve sectors and found a moderate correlation of the form ln ($S_{\rm X-ray}$) $\approx$

(1.1 to 2.5) $\times$ ln($S_{\rm radio}$) + ln(scale factor).

We chose Cas A for study because of the availability of both high quality radio and X-ray data. In the cm wavelength range, Cas A is the brightest object in the sky outside of the solar system. At an age of 300 years, it is believed to be in a pre-Sedov phase, and is situated $3.4^{+0.3}_{-0.1}$ kpc away (Reed et al. 1995), at the far edge of the Perseus arm. The column densities of hydrogen between here and Cas A ($N_{\rm H} \approx 10^{22}$ cm^{-2}) are such that the optical depths of 1-2 keV X-rays are of order unity. Therefore, column densities inhomogeneously distributed across the remnant, such as due to structures local to Cas A and the Perseus arm, can play a large role in determining the apparent soft X-ray morphology. For these same reasons, Cas A is an excellent choice as a background source for radio and X-ray interstellar medium (ISM) studies.

The ISM has been well-studied in λ21 cm absorption (Mebold & Hills 1975; Bieging, Goss, & Wilcots 1991; Schwarz, Goss, & Kalberla 1997, hereafter MH75, BGW & SGK respectively). Although BGW's VLA* study was the highest resolution and most detailed, it only covered the velocity range of the Perseus arm. SGK's Westerbork study, though only at a resolution of 30′, covered both the Orion and Perseus spiral arms. In addition there have been numerous molecular absorption studies using Cas A — in H_2CO (Goss, Kalberla, & Dickel 1984), in CO (Troland et al. 1985, hereafter TCH and Wilson et al. 1993, hereafter WMMPO) (Troland, Crutcher, & Heiles 1985; Wilson et al. 1993, hereafter TCH & WMMPO respectively), NH_3 (Batrla, Walmsley, & Wilson 1984; Gaume, Wilson, & Johnston 1994) and (Bieging & Crutcher 1986, hereafter BC). The absorption patterns in the various *molecules* are similar to each other, but very different than that of the H I. However, C II seems to be correlated with the H I instead of the molecules Anantharamaiah et al. (1994).

(Rasmussen 1996, hereafter R96) studied the spatial dependence of X-ray model

*The Very Large Array is a facility of the National Science Foundation operated under operative agreement by Associated Universities, Inc.

parameters using the ASCA satellite, resulting in a total column density ($N_{\rm H}$) map. In this paper, we compare the radio absorption data of BC and SGK to the $N_{\rm H}$ map of R96. From this we measure the scaling relation between column density and equivalent line widths from the radio absorption measurements of SGK and BC. This allows measurements of the average H I spin temperature and the $N_{\rm OH}/N_{\rm H_2}$ abundance of the ISM to be calculated.

4.2 Analysis

4.2.1 Comparing Cas A's X-ray and Radio Surface Brightnesses

In order to compare the HRI X-ray ($S_{\rm HRI}$) and radio ($S_{\rm radio}$) surface brightnesses, we must first correct for the soft X-ray optical depths, which are of order unity. The higher energy ASCA data do not suffer from this problem, but a full analysis of those data at sufficient resolution has not yet been done. In order to estimate the X-ray optical depths, we made use of BC's λ18 cm OH and SGK's λ21 cm H I absorption data (see Fig. 4.1 A & B and Fig. 4.2) to calculate the total column density ($N_{\rm H}$, Fig. 4.1C and Fig. 4.2) of hydrogen along each line of sight to the remnant. Once an $N_{\rm H}$ map has been calculated, a corrected image of unabsorbed soft X-ray emission ($S_{\rm X_{ctd}}$, Fig. 4.1E) can be derived. Next, we can compare the actual thermally produced X-ray surface brightness ($S_{\rm X_{ctd}}$) with Cas A's well-known radio synchrotron morphology ($S_{\rm radio}$, Fig. 4.1F). We first describe a direct method for carrying out these corrections, and then the alternative scheme we found it necessary to use.

We start by writing the X-ray optical depth as

$$\tau_{\rm X} \equiv \sigma_{\rm X}^{\rm HRI} \times N_{\rm H} \tag{4.1}$$

where $\sigma_{\rm X}^{\rm HRI}$ is the cross-section per hydrogen atom averaged over the HRI bandpass; $N_{\rm H}$

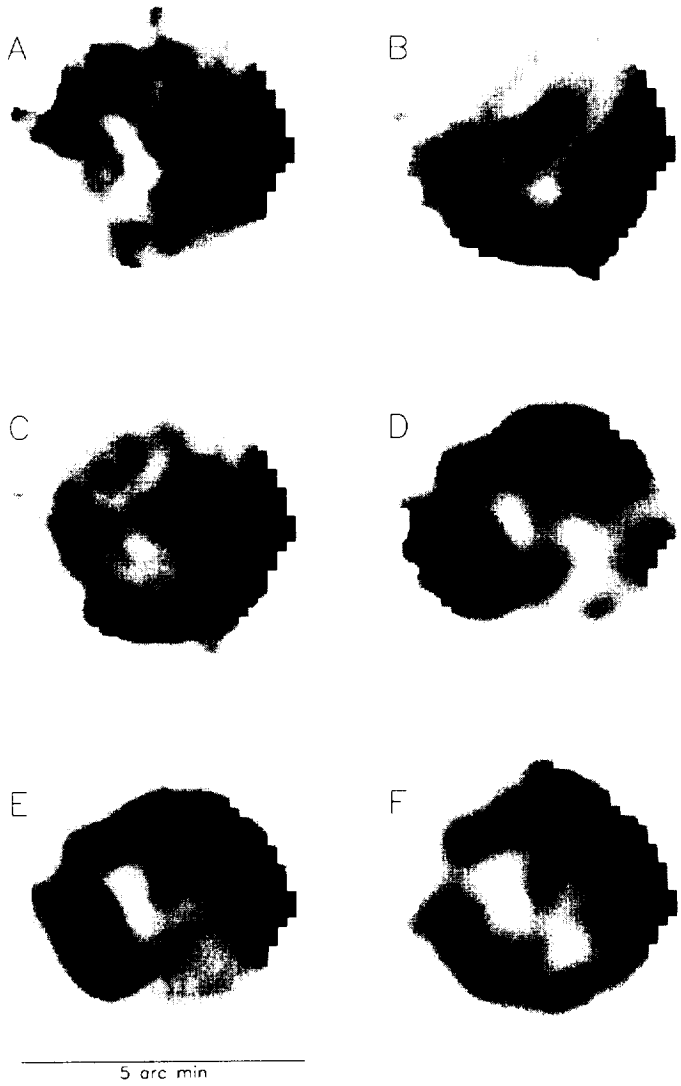

Figure 4.1: 30″ resolution images of Cas A. The histogram-equalization method of scaling was used to enhance the images. The quantities represented are: (A) the equivalent width of the λ21 cm line; (B) the equivalent width of the λ18 cm (OH) line; (C) the total column density as derived from images A and B; (D) the logarithm of the ROSAT HRI image; (E) the logarithmic HRI image corrected for absorption; (F) a logarithmic λ20 cm VLA continuum map. Histograms of the quantities shown in images A, B and C are shown in figure 4.2; image D ranges from -2.6 – -0.8 ln(cts s^{-1} $beam^{-1}$); a plot of image E versus image F is shown in figure 4.4.

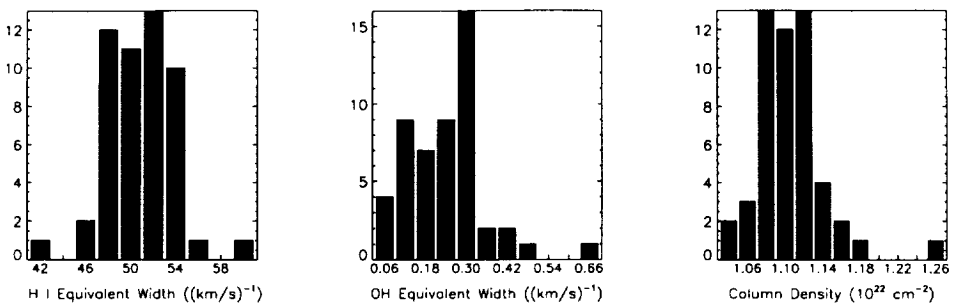

Figure 4.2: Histograms of $\lambda 21$ cm equivalent width, $\lambda 18$ cm equivalent width and the derived column density ($N_{\rm H} = D\,(EW_{\rm HI}) + E\,(EW_{\rm OH}) + F$).

is the total number of hydrogen atoms along the line of sight. We can then calculate

$$N_{\rm H} = N_{\rm H\,I} + 2 \times N_{\rm H_2} \tag{4.2}$$

For the atomic hydrogen,

$$N_{\rm H\,I} = \left(1.83 \times 10^{18}\ EW_{\rm HI}\right) \left(\frac{T_{\rm spin}}{^\circ{\rm K}}\right)\ {\rm cm}^{-2} \tag{4.3}$$

where $T_{\rm spin}$ is the spin temperature of the atomic hydrogen, and the equivalent width in H I is calculated by integrating the observed optical depths τ_v over all velocities

$$EW_{\rm HI} \equiv \int \tau_v \, {\rm d}v \tag{4.4}$$

In the case of the molecular hydrogen, for which direct measurements are not available, we can use the OH absorption data, and write

$$N_{\rm H_2} = \frac{N_{\rm H_2}}{N_{\rm OH}} \times \left(2.2 \times 10^{14}\ EW_{\rm OH}\right) \left(\frac{T_{\rm ex}}{^\circ{\rm K}}\right)\ {\rm cm}^{-2} \tag{4.5}$$

with equivalent width defined as above.

This approach (of finding the X-ray absorbing column densities *a priori* from radio line data) is the straight forward one, but it has several problems because of uncertainties in the scaling constants that must be used. The effective X-ray cross-section has been modeled by (Morrison & McCammon 1983, hereafter M&M), who showed

that the monoenergetic cross section depends strongly on photon energy and changes discontinuously at quantum thresholds. Therefore, $\sigma_{\rm X}^{\rm HRI}$ is highly dependent on Cas A's soft X-ray spectrum, and thus has significant uncertainties. In addition, it is difficult to know what value to use for the H I spin temperature, as was demonstrated by MH75. Another major uncertainty comes from the OH abundance value. These issues will be discussed more fully in section 4.2.2.

We therefore adopted a different approach, simultaneously determining the X-ray-radio relationship and the absorption corrections by minimizing the quantity

$$\chi^2 \equiv \frac{[\ln(S_{\rm X_{ctd}}) - \eta \ln(S_{\rm radio}) - \ln(k)]^2}{\sigma^2_{\rm X_{ctd}} + (\eta_{i-1} \times \sigma_{\rm radio})^2} \tag{4.6}$$

with respect to the parameters η, A, B, and $[C - \ln(k)]$, where the logarithmic *corrected* X-ray image is given by:

$$\begin{aligned} \ln(S_{\rm X_{ctd}}) &= \ln(S_{\rm HRI}) + \tau_{\rm X} \\ &= \ln(S_{\rm HRI}) + A \times EW_{\rm H\,I} \\ &\quad + B \times EW_{\rm OH} + C\,. \end{aligned} \tag{4.7}$$

The parameter η measures the logarithmic scaling between the X-ray and radio emission. The parameter $[C - \ln(k)]$ contains both information on the normalization of emissivities (equation 4.6, parameter $\ln(k)$), as well as allowing for absorption that is not well-modeled by the H I and OH optical depths (equation 4.7, parameter C). This could be due, e.g., to H I saturation, variations in $T_{\rm spin}$, which are not reflected in X-ray absorption, and the likely existence of Orion Arm molecular gas outside of the BC measurements.

Because the errors in the data are a function of the radio and X-ray flux, it is important that the error images are included in the determination of χ^2 (equation 4.6).

As a simplifying procedure, we performed the fits iteratively, holding the errors fixed as propagated from the previous best fit parameters (A_{i-1}, B_{i-1}, and η_{i-1}):

$$\sigma^2_{\rm X_{ctd}} = \sigma^2_{\ln(S_{\rm HRI})} + (A_{i-1} \times \sigma_{EW_{\rm H\,I}})^2 \tag{4.8}$$

$$+(B_{i-1} \times \sigma_{EW_{OH}})^2 .$$

Prior to performing the χ^2 analysis, the maps were prepared as follows. In order to match the resolution of the H I data, we smoothed the OH line and continuum maps to a resolution of 30″, before calculating the optical depths and equivalent widths. We also smoothed the epoch 1990 (3.4 ks live-time) ROSAT HRI image (obtained from the HEASARC public archive) and the epoch 1987 λ20 cm VLA continuum map described by A&R, to 30″ resolution. Errors in each map were calculated using standard methods. The resulting maps contain 51 independent beams, and are shown in figure 4.1. Histograms of the radio absorption values are shown in figure 4.2.

The minimum value of $\frac{\chi^2}{N}$ was 47, showing that there is a large amount of scatter still unaccounted for in the X-ray/radio relation. The number of degrees of freedom, N, coincidentally, also equals 47. In order to calculate 70% and 99% confidence limits $(\delta_{X70}, \delta_{X99})$ for parameter X, we determined the value of

$$\chi^2(X \pm \delta_{X70,X99}) \equiv \chi^2_{\rm min} \times (1.097, 1.542) \tag{4.9}$$

where $\chi^2_{\rm min}$ is the global minimum value of χ^2. Following Bevington & Robinson (1992), while parameter X is being varied, all other parameters are allowed to float to minimize χ^2 for that value of X. Figure 4.3 shows contour plots of the confidence levels, as a function of parameters A and B, η and $[C - \ln(k)]$.

Figure 4.4 shows the correlation between the thermal X-ray emission $\ln(S_{\rm X_{ctd}})$ and radio synchrotron radiation $(\ln(S_{\rm radio}))$. The best fit slope is $\eta = 1.21 \pm 0.41$, (70% confidence limit), with the error probably dominated by real scatter in the X-ray/radio relation. In section 4.3, we will discuss the competing effects of emissivity and path length that can contribute to such differences.

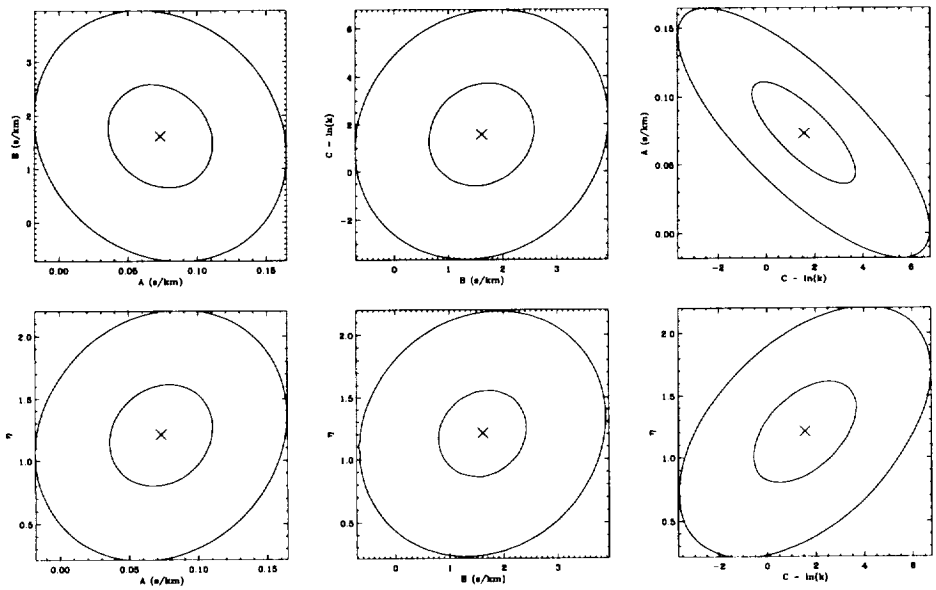

Figure 4.3: 70% and 99% confidence levels derived from the goodness of fit χ^2 obtained by fitting a power-law relation between the radio and corrected X-ray morphological distributions. They are shown here as a function of the parameters A, B, $[C - \ln(k)]$ and η as defined in the text. The $\times$ in each plot represents the minimum χ^2.

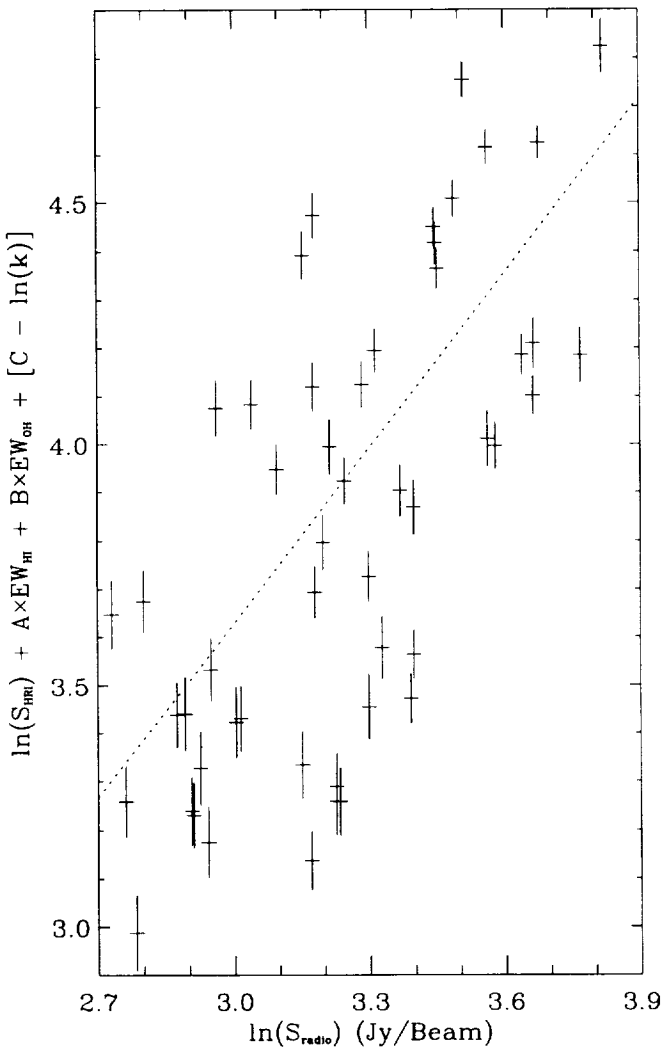

Figure 4.4: Plot of the logarithmic soft X-ray emission corrected for absorption using the best fit values for parameters A, B, and $[C - \ln(k)]$ as defined in equation 4.7 versus the logarithmic $\lambda 20$ cm emission. The line represents our the best fit model: $\ln(S_{\mathrm{X_{ctd}}}) - \ln(k) = \eta \ln(S_{\mathrm{radio}})$.

4.2.2 Interstellar Medium Parameters

In this section, we introduce a technique for determining physical parameters of the ISM. Although our results have large uncertainties, the method is useful in confirming previous estimates, and could be extended to higher accuracy. Using the above procedure, we simultaneously determined the scaling parameters between H I and OH optical depths and soft X-ray absorption due to the line-of-sight ISM column density. The best fit values are $A = 0.073 \pm 0.039$ (km/s)$^{-1}$, $B = 1.6 \pm 1.0$ (km/s)$^{-1}$ and $[C - \ln(k)] = 1.6 \pm 2.2$ (Fig. 4.3).

The X-ray absorption and the total column density can also be measured more directly through X-ray spectral fitting. With spectral fitting, the effective X-ray cross-section, which changes strongly as a function of photon energy (M&M), can be explicitly included. R96 assumed Cas A's X-ray spectrum to consist of power-law emission plus many Gaussian spectral emission lines (see HGTN), absorbed by the ISM assuming M&M's effective cross-sections. This resulted in a 32×32 map (19 ″/pixel) for each parameter fit, including the column density. A factor of 2 oversampling was used, so the "beam size" is approximately 40″; this is also a function of ASCA's complex point spread function (Tanaka, Inoue, & Holt 1994). However, since these fits did not cover the whole image of Cas A, and because they rely on a "super-resolution" of the data, we chose not to use them for the original correction of the X-ray maps. We will, however, use the ASCA data to derive parameters of the interstellar medium.

In this section, we compare our optical depth image to R96's ASCA $N_{\rm H}$ image to derive a second set of scaling parameters for EW_{Hi} and $EW_{\rm OH}$. Combining this with the previously determined scaling parameters, and using equations 4.3 and 4.5, we can then determine both the effective ROSAT HRI cross section as well as some important ISM parameters.

To perform this analysis, we first aligned the ASCA field with our radio images by maximizing the cross-correlation of R96's $N_{\rm H_{ASCA}}$ image with our optical depth image

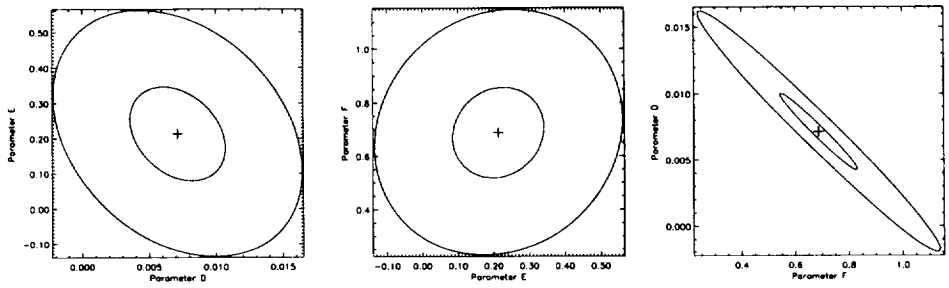

Figure 4.5: The χ^2 between the ASCA and radio absorption line derived column densities as a function of the scaling parameters D, E and F, which are defined such that $N_H = D\,(EW_{\rm HI}) + E\,(EW_{\rm OH}) + F$. At each point in the plots, the parameter not shown was set to the value which would minimize χ^2 there. Contour levels represent confidence levels of 70% and 99%.

$(A \times EW_{Hi} + B \times EW_{\rm OH})$. This yielded a total of 25 independent 30″ beams with which to compare the X-ray and radio absorption. With $N_{\rm H_{ASCA}}$ in real physical units ($10^{22}{\rm cm}^{-2}$) and the equivalent widths in km/s, we then minimized the quantity:

$$\chi^2(D,E,F) \equiv \sum (N_{\rm H_{ASCA}} - N_{\rm H_{Radio}})^2 \tag{4.10}$$

where D, E, and F are defined by

$$N_{\rm H_{Radio}} = D\,(EW_{\rm HI}) + E\,(EW_{\rm OH}) + F \tag{4.11}$$

The best fit values for parameters D,E and F are: $(7.1 \pm 3.8) \times 10^{-3}$, 0.213 ± 0.141, and 0.69 ± 0.19 respectively (70% confidence); the χ^2 dependence on D,E and F is shown in Figure 4.5. The confidence limits are defined as:

$$\chi^2(X \pm \delta_{X70,X99}) \equiv (1.134, 1.831) \times \chi^2_{\rm min} \tag{4.12}$$

as appropriate for 22 degrees of freedom. The use of $\chi^2_{\rm min}$ is necessary because R96 did not provide an error image.

At this point, we have two sets of scaling parameters for $EW_{\rm HI}$ and $EW_{\rm OH}$. One set depends on the HRI cross section; the other does not. We can therefore use equations

4.7 and 4.11 to find that

$$\sigma_{\rm X}^{\rm HRI} = \frac{A}{D} = \frac{B}{E} \tag{4.13}$$

This yields $\frac{A}{D} = 10.3 \pm 7.7$ and $\frac{B}{E} = 7.6 \pm 6.8$ with a weighted average of $\sigma_{\rm X}^{\rm HRI} = (8.8 \pm 5.1)$; all are in units of $10^{-22}{\rm cm}^2$. This value of $\sigma_{\rm X}^{\rm HRI}$ is several times larger than the rough estimate we made by averaging the M&M cross-section values over the bandpass, weighted by the HRI effective area, and assuming a flat spectrum for Cas A. If this discrepancy is real, then it indicates that on average, Cas A's source spectrum is probably decreasing with increasing energy in the HRI bandpass.

From our measured parameters D and E, and assuming that we have isolated the contributions due to H I and OH in our χ^2 analysis, we can then use equations 4.3 and 4.5 and the values of D and E to calculate $T_{\rm spin}$ and $N_{\rm OH}/N_{\rm H_2}$. However, the presence of a significant non-zero value for F shows that we have not successfully modeled all of the X-ray absorption, and we will have to take this into account.

First, we consider the molecular hydrogen component. Figure 4.5 shows that there is very little correlation between parameter E and either parameter D or F. This implies that our best fit parameter E is robust to uncertain contributions to the absorption from other ISM components. We therefore find the fraction of OH in the Perseus spiral arm as:

$$\frac{N_{\rm OH}}{N_{\rm H_2}} = (4.1 \pm 2.7) \times 10^{-6} \left(\frac{T_{\rm ex}}{20^\circ{\rm K}}\right) . \tag{4.14}$$

This derived ratio is nominally higher than the $(2.9 \pm 2.7) \times 10^{-7}$ quoted by WMMPO.

The contribution of the atomic component (parameter D) is more problematic, because of its correlation with parameter F (see Fig. 4.5). Formally, we can calculate an average spin temperature for the H I as

$$T_{\rm spin} = D/(1.83 \times 10^{-4}) = (39 \pm 21)\,^\circ{\rm K} . \tag{4.15}$$

This temperature is the same as the spin temperature derived by Payne, Anantharamaiah, & Erickson (1994) towards Cas A and in the range of those found by Kalberla,

Schwarz, & Goss (1985), toward 3C147. The major contribution to the error in D actually comes from its correlation with F.

There are three likely sources for a non-zero F: Orion arm molecular gas (not measured by BC), saturated H I and hot inter-cloud H I.

TCH observed Orion arm ^{13}CO column densities to be approximately 20% of the Perseus arm column density. This implies that only about 6×10^{20} cm^2 of $N_{H_{ASCA}}$ ($\approx$ 10% of parameter F) can be accounted for by molecular gas outside of BC's velocity range.

BGW named the highly saturated H I absorption feature near a velocity of -48 km/s "the curtain", because of its spatial uniformity and high optical depth (mostly above 5). Here SGK's H I equivalent width measurements underestimate the actual absorption. If SGK accounted for about half of the H I in "the curtain", the unmeasured portion should account for about 1-2 $\times$ 10^{21} cm^2 of $N_{H_{ASCA}}$ or $\approx$ 15% of parameter F).

MH75 used the Effelsberg 100m telescope to observe the λ21 cm line in both emission and absorption toward Cas A. Their observations are consistent with a two-temperature H I model; where the hot component has spin temperatures in excess of about 3500 °K, which would be observed only minimally by SGK (equation 4.3). MH75's estimated cloud/inter-cloud mass ratio is about 1:2, which could account for all of our measured parameter F.

These factors complicate our determination and interpretation of T_{spin}, as described above, so it should be considered simply as a characteristic value for the cooler gas.

4.3 Discussion

4.3.1 The X-ray/Radio Emissivity Relation

The long-term objective of comparing the X-ray and radio emission in Cas A is to identify the state and structure of the thermal and relativistic plasmas and the physical

connections between them. The X-ray emission spectrum from Cas A is itself believed to come from two different plasmas (Jansen et al. 1988). The low temperature plasma ($kT < 1$ keV) is most likely reverse-shocked ejecta; models of the emission in the ROSAT band show that the emissivity is a mixture of thermal bremsstrahlung and line emission. The higher temperature plasma ($kT \approx 3$ keV) is most likely circumstellar matter shocked by the blast wave. The reverse shock in Cas A is believed to currently dominate the soft X-ray emission (Jansen et al. 1988, F80;); the factors that influence the relative luminosity of these two shocks are discussed in detail by Masai (1994). We have shown here the importance of absorption for the low energy X-rays; analyses based on hardness ratios (e.g., HGTN) must first correct for this effect.

In the radio band, most of the emission comes from the bright ring, which is identified with either the reverse shock, the contact discontinuity, or both (Gull 1973b,a). There is also a lower surface brightness radio plateau beyond the ring and a wealth of structures on smaller scales, including knots, bow shocks, filaments, etc, with lifetimes of order 30 years.

To interpret the observed radio/X-ray correlation, we must now distinguish between surface brightness and emissivity. If the emissivities in a remnant do not vary spatially, then all variations in surface brightness must be due to variations in path length (or filling factor), and the X-ray and radio brightnesses should be proportional to each other (logarithmic slope of 1). Some of the brightness variations in Cas A are clearly due to path length differences, such as the bright ring itself. However, even within the bright ring, the local radio brightness may largely be due to the path length through the emitting material at that position, rather than large variations in the intrinsic emissivity. The observations of Reed et al. (1995) show that the apparently complete Cas A shell is very non-uniform in optical line emission. The analysis of A&R show the presence of major dynamical asymmetries which are probably coupled to spatial variations. The large velocity gradients in the X-ray data from ASCA (HGTN) also

demand large-scale non-spherical structures in the X-ray emitting material.

Given the major role played by path length variations through the emitting material, our observed logarithmic slope of 1.2 for the X-ray/radio *surface brightness* relationship can be understood only as a lower limit to the slope relating the actual *emissivities*. If the variations in emissivity are much less than the variations in path length, the emissivity slope could be much higher. We are therefore unable to comment on how the various processes leading to soft X-ray and radio emission vary with one another. The same problem might easily affect the results of MLDG, whose X-ray/radio logarithmic slope could be as low as 1.1. At present, it is not clear how to isolate true variations in emissivity.

The modeling of the radio/X-ray emissivity relationship in an inhomogeneous rapidly-evolving remnant such as Cas A is also quite uncertain. It is important to avoid the simple scaling relations based on X-ray thermal bremsstrahlung, such as discussed by MLDG, because such relations ignore the dependence of line emission on factors other than density. In addition, we know from recent numerical simulations that the magnetic field amplification (Jun & Norman 1996b) and relativistic particle acceleration (Jones, Kang, & Tregillis 1994) reflect the history of the plasma and cannot be simply described by current state parameters such as density and temperature. Jun (1995) has modeled the radio synchrotron radiation and the thermal bremsstrahlung component of X-ray emission in his 3D MHD simulations of young supernova remnants. Although he finds the same major features in the X-ray and radio emission, e.g., the clumpy bright ring, there is only a weak correlation between the two (B. I. Jun 1996, private communication). This is due to the strong dependence of only the radio emission on the local magnetic field. Therefore, in order to effectively use such observations as presented here and in MLDG, we need both more sophisticated time-dependent analyses of the X-ray radiative transfer and an understanding of the relationship on various scales between the magnetic field and other hydrodynamical parameters.

4.3.2 The Western Molecular Cloud

The western edge of Cas A is unusual in a number of ways, suggesting an interaction between the expanding SNR and a local molecular cloud. Considering the properties of Cas A itself, we first note that the brightest radio and X-ray emission is found in this region. HGTN show that the western region has significantly lower X-ray equivalent widths than the other major emission regions. They interpret this as due to relatively stronger emission from the outer shock, which would be expected if it were moving into an area of higher density. A&R found that the motions of bright radio knots in the west showed extreme departures from the relatively uniform expansion seen in other regions. Many western knots are actually moving back toward the center of expansion - these must be due to an external interaction. This is also a region of steep radio spectral indices, implying that the conditions for relativistic particle acceleration are different here (Anderson & Rudnick 1996).

On the opposite side of the remnant, there is a break in the shell, and groups of fast moving radio (A&R) and optical (Fesen, Becker, & Goodrich 1988) knots. This so-called "jet" could result from expansion into a lower density region opposite the molecular cloud. A similar situation is modeled by (Tenorio-Tagle, Bodenheimer, & Yorke 1985).

Turning now to the external material, figure 4.1 (image C) is the derived $N_{\rm H}$ map, which shows strong absorption on the western side of Cas A. This dense cloud also shows up as the extreme value in the column density histogram in Fig. 4.2. The cloud is at an LSR velocity of $\approx$ -40 km/s, placing it in the Perseus arm (BC; TCH; WMMPO; Batrla, Walmsley, & Wilson 1984; Goss, Kalberla, & Dickel 1984). The OH column density maps of BC around -40 km/s trace out the regions of anomalous radio knot velocities and steep spectral indices discussed above. A trace of this cloud may also be visible in the H I measurements of BGW and SGK.

Gaume, Wilson, & Johnston (1994) studied the NH_3 and CO absorption towards

the bright western region. For the -39 km/s cloud, they determined the density to be $n_{H_2} \approx 1000\,\mathrm{cm}^{-3}$ characteristic of dark dust clouds, but found a higher than average kinetic temperature ($\approx 18\,^{\circ}$K) and line width (3.5 km/s). They suggested that the high temperature could be due to either an increased level of cosmic rays, or by cloud-cloud collisions. On the basis of both the unusual properties of Cas A in the west and the unusual cloud conditions there, it thus seems quite likely that an interaction is currently in progress.

Wilson & Mauersberger (1994) pointed out that the circular shape of Cas A argues for a lack of external interaction. However, the bright radio ring illuminates material that has just recently been decelerated, because it is found in the same area as the optical fast moving knots, which are travelling several times faster (A&R). Dohm-Palmer & Jones (1996) have performed 2D numerical simulations of an SNR expanding into a sharp ISM gradient. They find that at the time when the reverse shock on the high density side has reversed the velocity of some compact features, the overall ring deviates from being circular only by $\approx 10\%$. This is the same degree of non-circularity observed for Cas A's bright ring, and so removes this objection to an external interaction.

4.4 Conclusion

In this paper we have presented a technique to correct for spatially inhomogeneous absorption of soft X-rays in Cas A using radio absorption data. We find a good correlation between the soft X-ray and radio synchrotron emission from Cas A, but with significant scatter. The correlation is probably dominated by variations in path length, implying that the X-ray and radio emissions both occupy the same volumes. However, we have no evidence for a more detailed relation between their emissivities. A quantitative interpretation of these results requires more sophisticated modeling of both the X-ray radiative transfer and the relativistic plasma evolution in young SNRs.

Future X-ray/radio comparisons of Cas A should concentrate in at least the following two directions: studies at higher spatial resolution with deeper HRI measurements and comparisons with ASCA's spatially resolved spectroscopy. With a deeper ROSAT HRI observation, it may be possible to separate emissivity from path length variations. In addition, X-ray proper motions could be measured and compared with the radio proper motions. Since HGTN's paper, Cas A has been used as a calibrator for ASCA, so more ASCA data have been obtained and ASCA's response functions have been refined. This will enable image reconstruction techniques to be applied to narrower bandpass images and better quality spatially resolved spectral fitting. Studying the correlations between the radio and X-ray morphologies as a function of X-ray energy will allow the different emission mechanisms and temperature and metallicity structures to be distinguished.

We have shown that Cas A is likely to be interacting with a dense cloud in the west. This has affected both the properties of the remnant and the cloud. Such interactions may play an important role both in SNR dynamics, and in the transfer of energy into the ISM.

We have also demonstrated a new technique for probing the ISM. By comparing X-ray and radio spectroscopic absorption measurements, the H I spin temperature and molecular abundances ratios were measured. Future studies of other radio and X-ray bright extended objects can significantly enhance our understanding of the ISM, by comparing spatially resolved column densities from either the ROSAT PSPC or ASCA with radio and far IR atomic and molecular line data.

This work was supported in part by the National Science Foundation, through grant number AST 93-18959 to the University of Minnesota. Funding was also provided by NASA/GSFC's Laboratory for High Energy Astrophysics through the Graduate Student Researchers Program. This research has made use of data obtained from the US ROSAT Public Data Archive which is jointly managed by the ROSAT Science Data Center and the HEASARC. The HEASARC is a collaboration of the Laboratory

for High Energy Astrophysics and the NSSDC at NASA/GSFC. The following data were kindly provided for our analysis — OH absorption data, John Bieging; ASCA column densities, Andrew P. Rasmussen; Westerbork H I absorption data, W. Miller Goss. We are also grateful for Goss's critical contributions as referee of this paper, and to John Dickey, B.I. Jun, Robert Petre and Ulrich Schwarz for helpful discussions and comments.

Chapter 5

Evidence for Proportionate Partition Between the Magnetic Field and Hot Gas in Turbulent Cassiopeia A

Accepted by The Astrophysical Journal Letters, May 1, 1998, as Keohane, Gotthelf & Petre

We present a deep X-ray observation of the young Galactic supernova remnant Cas A, acquired with the ROSAT High Resolution Imager. This high dynamic range (232 ks) image reveals low-surface-brightness X-ray structure, which appears qualitatively similar to corresponding radio features. We consider the correlation between the X-ray and radio morphologies and its physical implications. After correcting for the inhomogeneous absorption across the remnant, we performed a point by point (4″ resolution)

surface brightness comparison between the X-ray and radio images. We find a strong (r = 0.75) log-log correlation, implying an overall relationship of $\log(\Sigma_{\rm X-ray}) \propto (2.21 \pm 0.05) \times \log(\Sigma_{\rm radio})$. This is consistent with proportionate partition* (and possibly equipartition) between the local magnetic field and the hot gas — implying that Cas A's plasma is fully turbulent and continuously amplifying the magnetic field.

Subject headings: supernova remnants – supernovae: individual (Cas A) — X-rays: ISM — turbulence — MHD — techniques: image processing

5.1 Introduction

A comparison of the X-ray and radio emission of young supernova remnants (SNRs) provides a powerful tool for investigating the physical relationships among the thermal plasma, cosmic ray electrons and the magnetic field (e.g., Dickel et al. 1982; Matsui et al. 1984; Arendt et al. 1990; Dyer & Reynolds 1998). Radio emission is governed primarily by the density of relativistic electrons and the magnetic field strength, while the intensity in soft X-rays is dictated by the gas density. Shell SNRs provide excellent laboratories for investigating the interaction among these physical processes, with Cas A being the natural launching point for such investigations, because of its high surface brightness in both the radio and X-ray wavelength regimes.

Previous work has shown that the soft X-ray morphology of Cas A, on angular scales $\gtrsim 30''$ (or 0.5 pc at a distance of 3.4 kpc), is dominated by absorption effects (Keohane, Rudnick, & Anderson 1996, hereafter KRA). When this absorption is taken into account, a higher degree of intrinsic correlation between the X-ray and radio images is found. Similarly, Holt et al. (1994) found a correlation between the radio and the hard

*We use the term *proportionate partition* to mean that the magnetic and gas pressures are proportional to each other ($B^2 \propto U_{\rm gas} \propto n_{\rm gas}$) — see page 60.

X-ray (E>4.5 keV) surface brightness, which is not affected by absorption. These correlations demonstrate that a simple relationship may exist among the underlying physical parameters.

In this Letter we investigate the relationship between the radio and X-ray emission on smaller angular scales. We use a newly acquired ROSAT High Resolution Imager (HRI) image of Cas A, with a 40 times longer exposure than used in KRA. To account for the inhomogeneous column density towards Cas A, we "deabsorb" the image using H I and OH absorption data (§5.2.2). We perform a point by point (4″ resolution) surface brightness comparison between the X-ray and radio images and find a statistically significant correlation (§5.2.3). We discuss the physical implications of this correlation (§5.3) and its implications for future observational and theoretical studies of Cas A and other young SNRs (§5.4).

5.2 Analysis

5.2.1 The Deep ROSAT Image of Cas A

Deep ROSAT HRI exposures of the SNR Cas A were obtained on December 23, 1995 and June 20, 1996, with the telescope optical axis pointed toward the center of the remnant. The standard processing yields a total of 232 ks of acceptable observing time, which produces the highest dynamic range (500:1) X-ray image of Cas A to date. A final image, shown in Fig. 5.1, was made by cross-correlating and adding images from the two exposures, using the radio image as an absolute reference.

In order to reduce instrumental blurring (e.g. the HRI "halo") we applied 5 iterations of the Lucy-Richardson restoration technique (Richardson 1972; Lucy 1974). As a kernel for the deconvolution, we used an on-axis analytical radially symmetric point spread function (PSF), which is valid because the PSF is approximately constant across the 5′ extent of Cas A. The resolution of the final image was estimated to be about 4″ (0.07

pc).

To correct any systematic scaling errors that may have been produced by the restoration process, we used a 4″ FWHM Gaussian smoothed version of the raw image to rescale the reconstructed image. This required a linear transformation with a scale of 0.92 and an insignificant zero-offset (0.31 cts/beam).

This new image of Cas A is the first with enough sensitivity to reveal X-ray features, on small angular scales ($\theta \gtrsim 4''$) and low surface brightness ($\Sigma_{\rm HRI} \gtrsim 0.03\,{\rm cts\,s^{-1}\,(')^{-2}}$), which have been only previously detected in the radio. Many of the most striking of these features are outside the bright shell, such as the northern and southern knots and the eastern jet region. To enhance this outlying structure, we show a spatially filtered version of the image (Fig. 5.3), produced by dividing the 4″ X-ray image by a 60″ Gaussian smoothed version of itself. This effectively removes large scale structure and enhances regions away from the bright ring.

5.2.2 The Deabsorbed Image

The large scale differences between Cas A's soft X-ray and radio morphology are dominated by foreground absorption effects (KRA). In order to take these effects into account, we used H I and OH absorption data (Schwarz, Goss, & Kalberla 1997; Bieging & Crutcher 1986), which trace the foreground atomic and molecular gas respectively. We translated these data into an optical depth map using the empirical relation (specific to Cas A) for each resolution element:

$$\tau_X = 0.073\,{\rm km^{-1}s} \times EW_{\rm H\,I} + 1.6\,{\rm km^{-1}s} \times EW_{\rm OH} + 1.6 \qquad (5.1)$$

where τ_X is Cas A's optical depth over the ROSAT HRI bandpass, and $EW_{\rm H\,I}$ and $EW_{\rm OH}$ are the H I and OH equivalent widths respectively. A complete description of this method is given in KRA.

Using this HRI-specific 30″ resolution optical depth map, we produced the deabsorbed X-ray image of Cas A shown in Fig. 5.4. Absorption structure on scales between

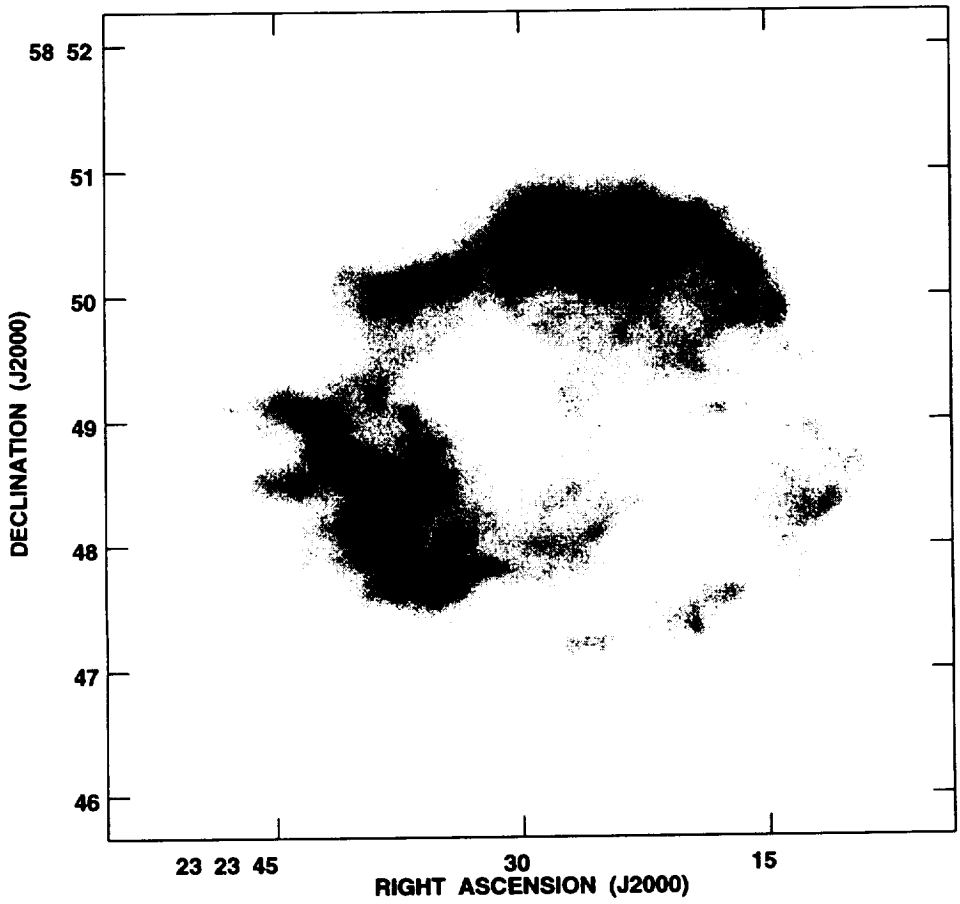

Figure 5.1: The 232 ks ROSAT HRI raw image scaled linearly. The maximum value is $102 \frac{\text{counts}}{0.5'' \text{pixel}}$. This images is oversampled with a pixel size of $0.5''$.

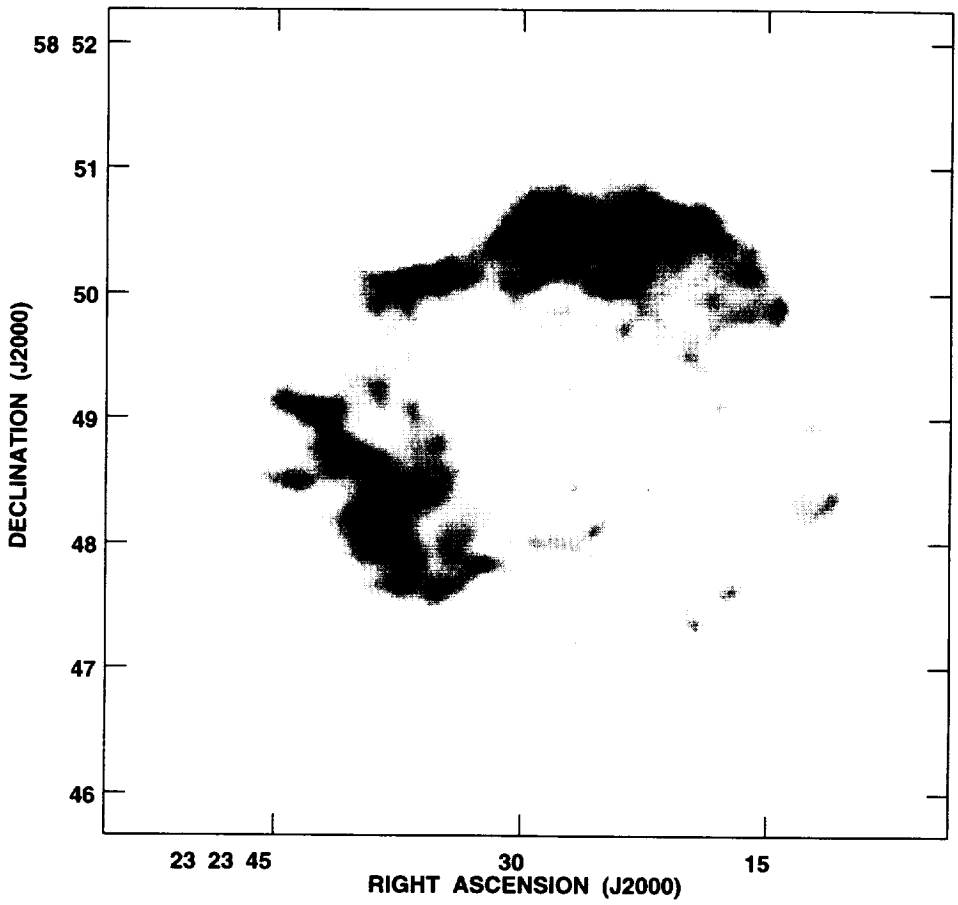

Figure 5.2: The Lucy-Richardson deconvolved image with 4″ resolution. This greyscale is scaled linearly with a maximum value of $5300 \frac{\text{counts}}{4'' \text{beam}}$. This image is oversampled with a 0.5″ pixel size, but has a resolution of 4″.

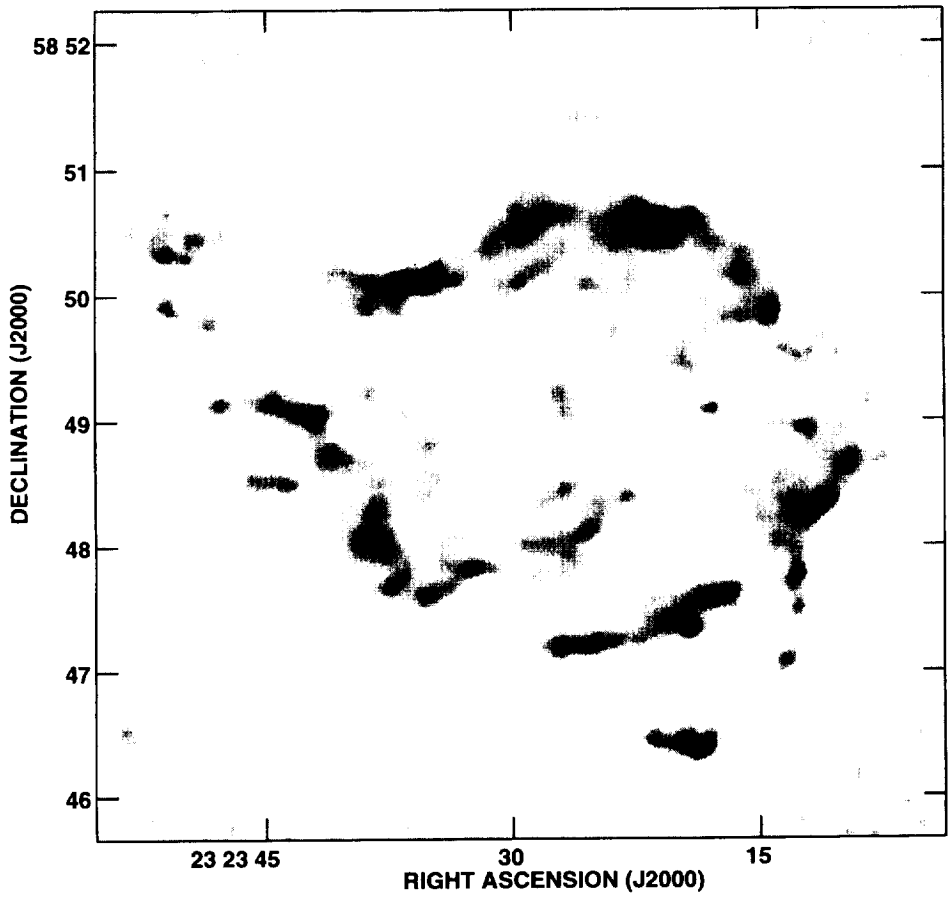

Figure 5.3: The deconvolved ROSAT HRI image divided by a 60″ smoothed version of itself. This figure is included in order to show the outlying and small-scale structure revealed by this deep exposure.

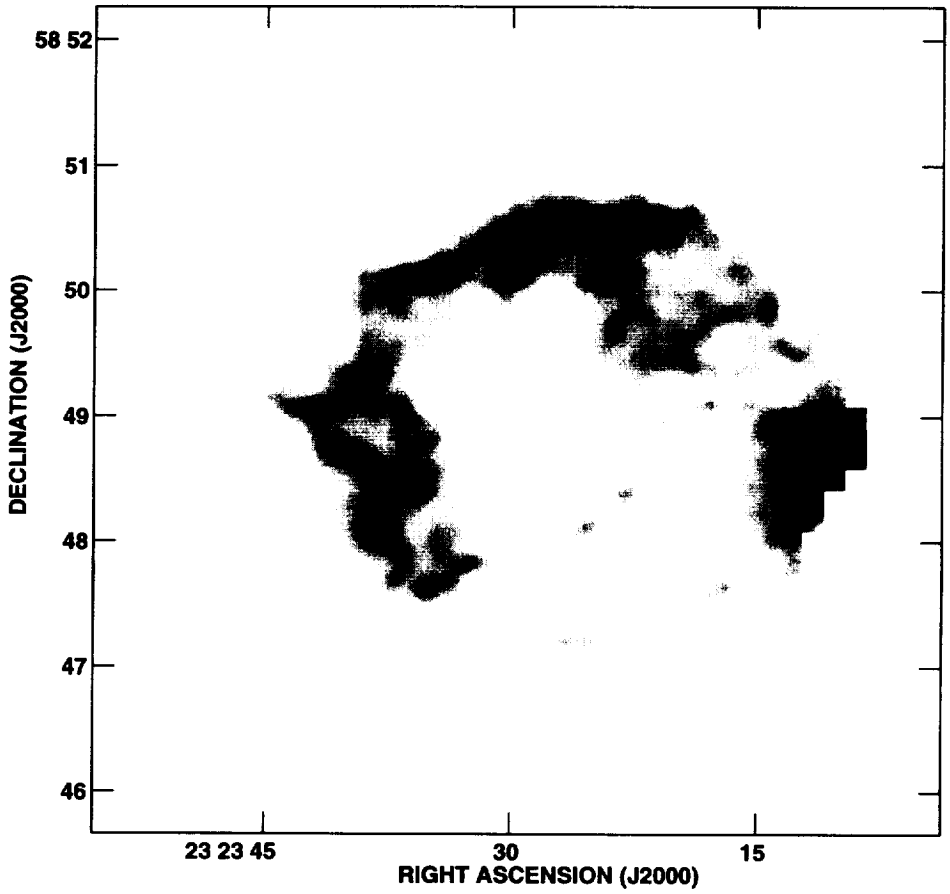

Figure 5.4: The deabsorbed ROSAT image scaled linearly. This image is oversampled with a 0.5″ pixel size, but its resolution is 4″. Note that the intervening column density was mapped in absorption, so this image is blanked outside of Cas A's radio-bright disk where the H I and OH optical depths are unreliable.

30″ and 4″ could affect our results, but the OH data of Bieging & Crutcher suggest that clouds of scales 30″–60″ dominate the absorption structure.

5.2.3 A Comparison with the Radio Image

The brightest features in the X-ray and radio maps are for the most part not correlated. However, when viewed on logarithmic scales, the deabsorbed X-ray map and the radio map appear quite similar (Fig. 5.5). In order to quantify this similarity, we performed a point-by-point comparison between the deabsorbed X-ray image and the most recent (epoch 1994) λ6 cm VLA map (Koralesky & Rudnick 1998). The time differences between the radio and X-ray observations ($\sim$1 year) will have no effect, given that typical proper motions in Cas A are of order $0.1''\,\mathrm{yr}^{-1}$ (Tuffs 1986). Figure 5.6 shows this correlation for 4″ pixels. This relationship has a correlation coefficient of r=0.75, and appears to be real but scatter-dominated.

We can parameterize the relationship between the deabsorbed X-ray surface brightness ($\Sigma_{\mathrm{X\,ray_D}}$) and the radio surface brightness (Σ_{radio}) as

$$\Sigma_{\mathrm{X\,ray_D}} \propto \Sigma_{\mathrm{radio}}^{\eta} \tag{5.2}$$

To find the value of η, we performed a least-squares analysis between the quantities $\log(\Sigma_{\mathrm{X\,ray_D}})$ and $\log(\Sigma_{\mathrm{radio}})$. We found the bisector between the two standard least-squares fits, as is appropriate for a scatter dominated linear correlation between two physical quantities (Isobe et al. 1990). At 4″ binning we find a best-fit $\eta = 2.21$ with a corresponding variance of $\sigma_\eta^2 = 6.8 \times 10^{-4} = (0.026)^2$. Monte Carlo simulations by Isobe et al. suggest that their formula for finding the variance in the slope underestimates the true uncertainty by about 10%, so we have set our "90% confidence" errors (Table 5.1) to the 1.8σ level.

We performed two simple tests to show that neither the correlation nor the scatter are artifacts of our analysis. First, to show that the correlation is intrinsic to the data,

we rotated one image by 180° about Cas A's geometrical center before re-correlating the data, whereby the correlation coefficient dropped from r=0.75 to r=0.41. This implies that the correlation is due to small scale structure, and is not simply a byproduct of Cas A's overall circular morphology. Second, to show the reality of the scatter, we created a simulated X-ray map, by assigning to each pixel an X-ray surface brightness that combined the radio surface brightness of that pixel scaled by a power law of 2.21, plus a random term representing the Poisson scatter in the X-ray map. The correlation between the radio and the simulated X-ray image showed no significant scatter, implying that the scatter in figure 5.6 due to statistical fluctuations is small compared with that observed. Possible physical explanations for this scatter are discussed in §5.3.2.

We performed the correlation analysis described above on maps with successively larger bin sizes in order to investigate the robustness of our analysis and investigate how increasing the pixel size affects the value of η (Table 5.1). As the data are binned, the best-fit η decreases, but its maximum value remains at about $\eta_{\rm max} \approx 2.3$.

To illustrate how smoothing could bias the measured values of η, assume that there exists a value $\eta_o > 1$, such that $\Sigma_{\rm X\,ray_D} = C \times \Sigma_{\rm radio}^{\eta_o}$. Thus the averaged quantities would be subject to the inequality:

$$\langle \Sigma_{\rm X\,ray_D} \rangle = \langle C \times \Sigma_{\rm radio}^{\eta_o} \rangle \geq C \times \langle \Sigma_{\rm radio} \rangle^{\eta_o} \ . \tag{5.3}$$

One possible explanation for the decreasing η with resolution is that this bias affects both the dim and bright parts of Cas A to about the same degree; however in proportion to their average brightness the dimmer regions are affected to a greater degree, so our logarithmic fitting returns a flatter slope η. Another possibility is that the binning of data lowers the dynamic range of the fit, thus skewing η towards its uncorrelated value of unity. A third possible explanation is that smoothing increases the importance of path-length variations as the governing physical parameter, thus also skewing η towards unity. Regardless of the particular explanation, the trend shown in Table 5.1 suggests that the intrinsic value of η is between 2.2 and 2.3.

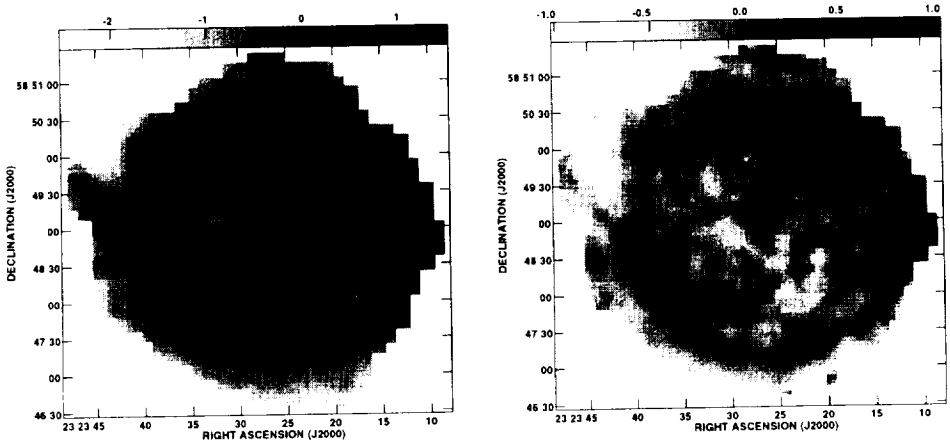

Figure 5.5: Logarithmically scaled images of Cas A. We present, from left to right, the deabsorbed X-ray image and the λ6 cm VLA map. The pixel size is 1″, the same as the beam size. The images are scales to correspond to the axes in Fig 5.6.

5.2.4 Deviations from the Trend

Figure 5.7 is a map of the quantity $\log(\Sigma_{\rm radio}^{2.21}/\Sigma_{\rm X\,ray_D})$, or a measure of deviations from the best-fit slope η. Consistent with an overall physical correlation, this map shows very little structure. There are no large scale features such as the shell or the western hot spot. A few key features are present, however. Some are relatively radio bright: the northern knot region; a knot near the center; and the outlying structure in

Resolution	N	r	η
4″	3948	0.75	2.21 ± 0.05
8″	876	0.75	2.19 ± 0.11
16″	210	0.76	2.14 ± 0.17
32″	47	0.75	1.96 ± 0.35
64″	10	0.49	1.43 ± 0.72

Table 5.1: The X-ray/radio Regression Parameters. Column definitions are: N = the number of independent points, r = the correlation coefficient, and η = the log-log surface brightness slope (see equation 5.2) with 90% confidence errors.

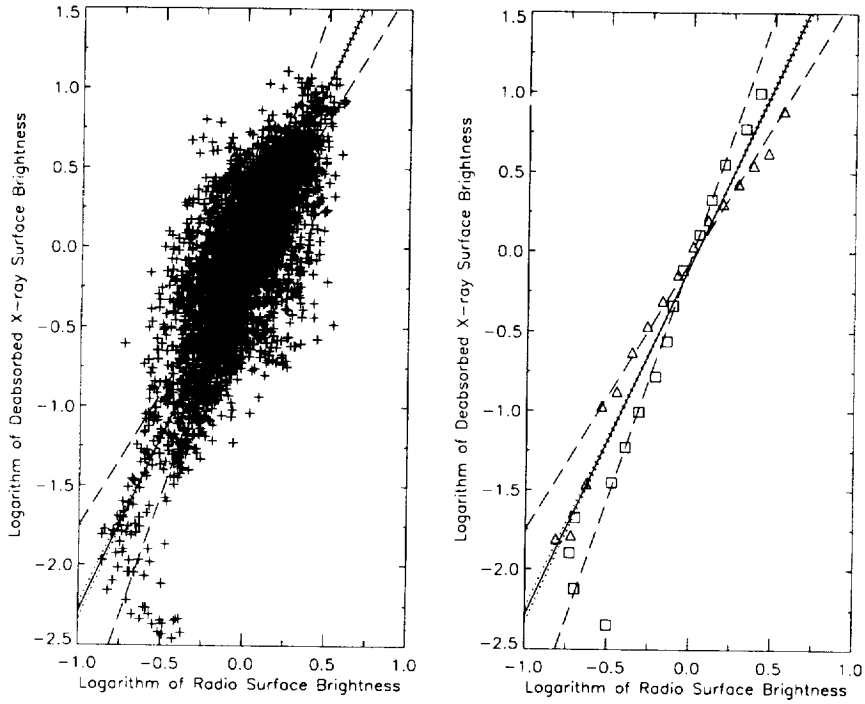

Figure 5.6: Log-log plots correlating the images in Fig 5.5. The left-hand plot is a standard scatter-plot with 3948 data points. For a majority of points, the random errors are smaller than the symbols plotted. On the right is a plot of the median $\log(\Sigma_{\mathrm{X\,ray_D}})$ in evenly spaced bins of $\log(\Sigma_{\mathrm{radio}})$ (triangles) and visa versa (squares). Both data sets are scaled to units of their respective overall median values. The same lines are plotted on each graph: the dashed lines represent the two standard least-squares fits (η_{xy}=1.7, η_{yx}=3.0); the dotted lines represent the 90% confidence range in the slope; and the solid line is the bisector of the two least-squares slopes.

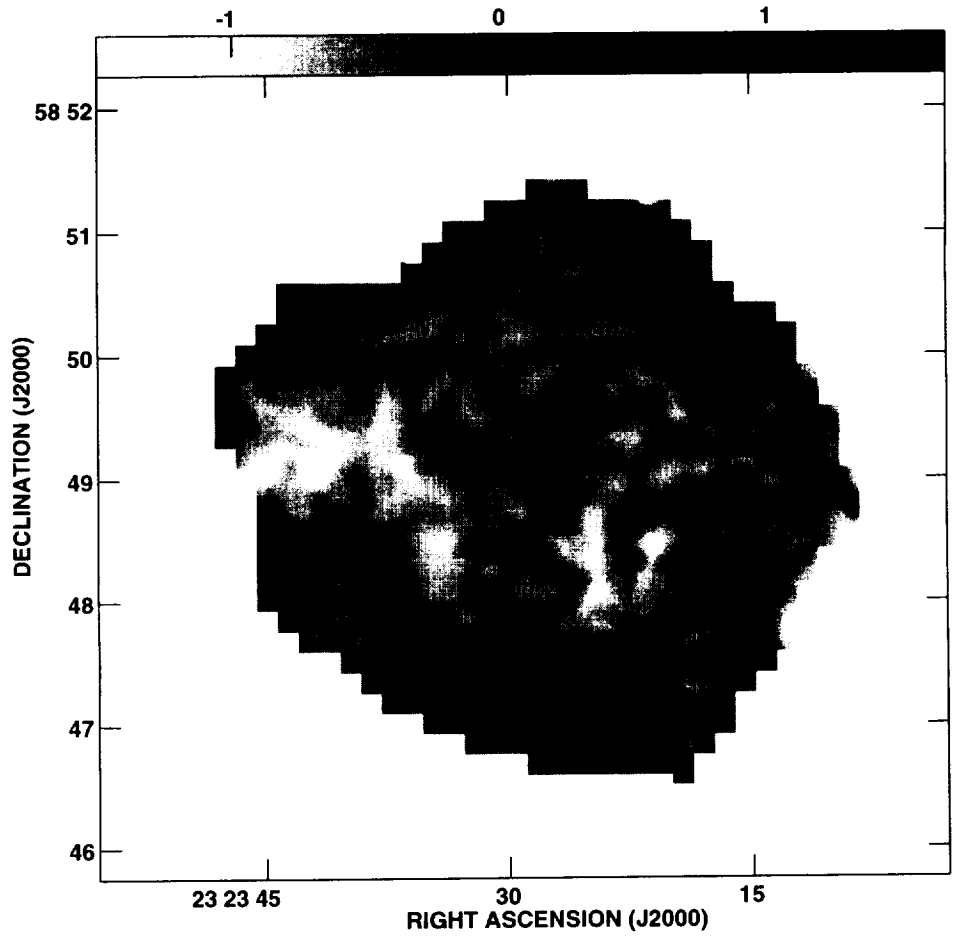

Figure 5.7: Plot of the quantity $\log(\Sigma^{2.21}_{\rm radio}/\Sigma_{\rm X\,ray_D})$. The greyscale ranges from log(min/mean) = −1.51 (white) to log(max/mean) = 1.67 (black). Like Fig.5.4, this image is oversampled with a 0.5″ pixel size, but a resolution of 4″.

the south. In addition, there is a relatively X-ray bright feature on the eastern shell.

5.3 Discussion

5.3.1 Proportionate Partition as a Possible Origin for the Correlation

The main objective of comparing the X-ray and radio emission in Cas A is to identify the physical relationships among the thermal plasma, cosmic ray electrons and magnetic field. In this section we show that our results are consistent with proportionate partition between the energy content of the gas and magnetic field. We also develop a physical justification for this by postulating a turbulent magnetohydrodynamic (MHD) plasma, which we argue is continuously amplifying the magnetic field. As both the trend and the exceptions are real, this scenario should be interpreted as valid "on average," but not necessarily for each feature in Cas A.

The ROSAT band spectrum of Cas A is dominated by line emission from H and He-like ions of Mg and Si and the L-shell ions of Fe (Holt et al. 1994). Thus by assuming a constant temperature plasma, we can relate the X-ray emissivity[†] ($\varepsilon_{\rm X\,ray}$) to the gas density ($n_{\rm gas}$) as:

$$\varepsilon_{\rm X\,ray} \propto n_{\rm gas}^2 \tag{5.4}$$

Cas A's radio emission mechanism is believed to be synchrotron radiation (Rosenberg 1970), arising from relativistic electrons (of density $n_{\rm rel}$) interacting with the magnetic field (B). We therefore characterize the radio emissivity ($\varepsilon_{\rm radio}$) as:

$$\varepsilon_{\rm radio} \propto n_{\rm rel} B^{1+\alpha} \tag{5.5}$$

where α is the radio spectral index ($\alpha = 0.77$, Baars et al. 1977).

[†]Here the emissivity, $\varepsilon_{\rm X\,ray}$, is defined in an analogous way to the radio emissivity, such that $\Sigma_{\rm X\,ray_D} \propto \int \varepsilon_{\rm X\,ray}\, dl$, where l is the path length.

Anderson et al. (1994) concluded that the radio brightness of the compact features in Cas A is governed primarily by magnetic field amplification. For this reason, we believe it reasonable to assume a constant (or uncorrelated) relativistic electron density. Therefore, equation 5.5 becomes:

$$\varepsilon_{\text{radio}} \propto B^{1+\alpha} \tag{5.6}$$

In their MHD simulations, Jun, Norman, & Stone (1995) show that Rayleigh-Taylor (R-T) instabilities in young SNRs are significantly enhanced by the presence of a magnetic field. Kelvin-Helmholtz instabilities, created by the shear flow along the R-T fingers, greatly enhance the magnetic field — especially on small scales. In addition, MHD studies of simple shear systems show that the magnetic field is amplified quickly as the energy cascades to smaller scales (Malagoli, Bodo, & Rosner 1996). On the scale where the magnetic field becomes dynamically important, reconnection and dissipation occur. It is therefore plausible that the magnetic field in Cas A is being amplified to the point of equipartition with the hot gas, locally on the smallest observable scales, so:

$$\frac{B^2}{8\pi} \approx U_{\text{gas}} \tag{5.7}$$

In aggregate this is approximately true. If one assumes equipartition between the magnetic field and the relativistic plasma, an energy density for each of these can be derived simply from the overall radio flux density. This overall magnetic energy density ($\frac{B^2}{8\pi}$) is comparable to the thermal energy density (U_{gas}) estimated from the integrated ASCA X-ray spectrum (Allen, G.E. *private communication*).

This suggestion of equipartition is apparently incompatible with the simulation of Jun & Norman (1996), whose 3-D simulations predicted magnetic fields significantly lower than equipartition. However, they also found that the higher the resolution of the simulation (i.e., the lower effective viscosity), the greater the resultant magnetic field. With regard to the analysis presented here, this distinction is moot. If the turbulent

cascade is halted on the smallest scales by the magnetic pressure, the equipartition relation (equation 5.7) should hold. On the other hand, if the turbulent cascade is the primary amplifier of the magnetic field, but is halted before the magnetic field reaches equipartition, then one would expect the system to still be in proportionate partition, i.e.:

$$B^2 \propto U_{\rm gas} \propto n_{\rm gas} \tag{5.8}$$

The analysis presented here cannot distinguish between equipartition (equation 5.7) and the looser constraint of proportionate partition (equation 5.8). Similarly, it does not matter here whether $U_{\rm gas}$ represents the turbulent energy density or the thermal energy density, so long as the energy density scales linearly, on average, with the gas density ($U_{\rm gas} \propto n_{\rm gas}$). We now combine equations 5.4, 5.6 and 5.8 to find a relationship between the X-ray and radio emissivities:

$$\varepsilon_{\rm X\,ray} \propto B^4 \propto \varepsilon_{\rm radio}^{\frac{4}{1+\alpha}} \propto \varepsilon_{\rm radio}^{2.26} \tag{5.9}$$

This simple relationship agrees remarkably with the value of η found in §5.2.3.

A similar and independent conclusion about turbulent magnetic field amplification was found by Koralesky & Rudnick (1998), who examined the changes in Cas A's radio emission as a function of azimuth over an 11 year baseline. They found that regions with the largest decrease in fractional polarization (corresponding to a decrease in order of the magnetic field) are decreasing the least in flux density. They suggest that the same process which is randomizing the magnetic field's orientation is also amplifying it, partially compensating for expansion losses.

This relationship between the radio and X-ray surface brightness is very different from the predictions of most other simple models. For example, in an isobaric model, the magnetic pressure and thermal pressure add to a constant, so the surface brightnesses would be anti-correlated. More realistically, a compression scenario where the magnetic field scales inversely with area so $B \propto n_{\rm gas}^{2/3}$, implies that $\eta = 1.7$, which is

also inconsistent with the data. If instead, we make the equally simple assumption that the relativistic electron density is proportional to the thermal gas density ($n_{\rm rel} \propto n_{\rm gas}$), then we find $\eta = 2.0$. While we cannot completely rule out this possibility, we do not favor it. The Larmor radii of the relativistic electrons are very small ($\sim 10^9$ cm for a 1 GeV particle in a 1 mG magnetic field), tightly coupling them to magnetic field lines, which in turn are coupled to the plasma. This suggests that $n_{\rm rel} \propto n_{\rm gas}$ may be a good assumption, but then one would also expect a relation between the magnetic field and density. When a magnetic field dependence is included, η is significantly reduced. For example, if $n_{\rm rel} \propto n_{\rm gas} \propto B$ then $\eta = 0.7$, which is clearly inconsistent with the correlation.

5.3.2 Possible Contributions to the Scatter

The simple model that fits the surface brightness ratio rests on three assumptions: constant relativistic electron density, constant X-ray emissivity per density squared ($\varepsilon_{\rm X\,ray}/n_{\rm gas}^2$), and proportionate partition. The relative flatness of the ratio map shows that deviations from these assumptions on large scales are absent. It is plausible, however, that the substantial scatter of the ratio for individual cells from the trend line represents local violation of one or more of these assumptions. The log of the rms deviation about the trend line is ± 0.38 (a factor of ~ 2.5); the log of the maximum excursion is ± 1.5.

If the scatter is due entirely to variations of $n_{\rm rel}$ or $B^2/n_{\rm gas}$ (proportionate partition), we find the corresponding rms variation of these is ± 0.17 in the log, or a factor of ~ 1.5. The X-ray emissivity is a function of both gas temperature and metal abundance. The emissivity scales linearly with the abundance of the metals producing the dominant lines in the ROSAT band, namely Mg and Si; thus local rms variations of a factor of ~ 2.5 in metallicity can account for the scatter. The emissivity scales with temperature in a less straightforward way, but deviations of $\log(\varepsilon_{\rm X\,ray}/n_{\rm gas}^2)$ of ± 0.4 can be accounted

for by log(kT) variations of ± 0.4.

Scatter of the degree indicated in any of these parameters is physically plausible. For instance, small scale gas pressure variations associated with a shock encountering a density enhancement can be as large as a factor of 6 (Dohm-Palmer & Jones 1996), which in turn could produce variations of $B^2/n_{\rm gas}$ or $\varepsilon_{\rm X\,ray}/n_{\rm gas}^2$ within the observed range. Measurements of any of these parameters on small angular scales, at best pose a challenge to current and future instruments, and at worst may be infeasible to measure (e.g., $n_{\rm rel}$).

5.4 Conclusion

We have performed a comparison of Cas A's radio and X-ray emission to a limiting resolution of 4″ (0.07 pc). The strong correlation between radio and X-ray surface brightness can be explained by the scenario that Cas A has "on average" a spatially constant relativistic electron density and proportionate partition on small scales between its thermal and magnetic energy densities, as would be expected from a fully turbulent MHD system.

These results may have important implications for theoretical work. The complex plasma physics of SNRs often must be simplified in order for computer simulations to run in a cost-effective manner. Unfortunately, most often one assumption is spherical or cylindrical symmetry, which is incompatible with turbulent flow. It may be possible, instead, to use the proportionate partition relation suggested by our result, along with some other characteristics of fully turbulent systems, to produce a more realistic first-order description of young, core-collapse, supernova remnants.

We thank Barron Koralesky for kindly providing the $\lambda 6$ cm radio data of Cas A in a digitized form. We also wish to thank Glenn Allen and John Dickel for insightful conversation. This work was supported by NASA.

Part II

X-ray Synchrotron Radiation

Chapter 6

Introduction to PART II: The Evidence for X-ray Synchrotron Radiation

6.1 The Origin of Cosmic Rays

6.1.1 What are Cosmic Rays?

Cosmic rays (CRs) are relativistic protons, electrons and nuclei which are bombarding the earth from all directions. They were first detected in 1912 by Victor Hess through electroscope measurements on manned balloon flights. Today, we detect protons and nuclei with energies ranging from about 10^8–10^{20} eV. Incredibly, the spectrum of these particles can almost be characterized by a single power-law ($N_e \propto E_e^{-\gamma}$) over 12 orders of magnitude in particle energy. When this power-law ($\gamma \approx 2.7$) is divided out, the resulting spectrum appears to have a feature at 10^{14}–10^{16} eV, commonly known as the "knee," above which the spectrum steepens slightly (Fig. 6.1). This knee has led

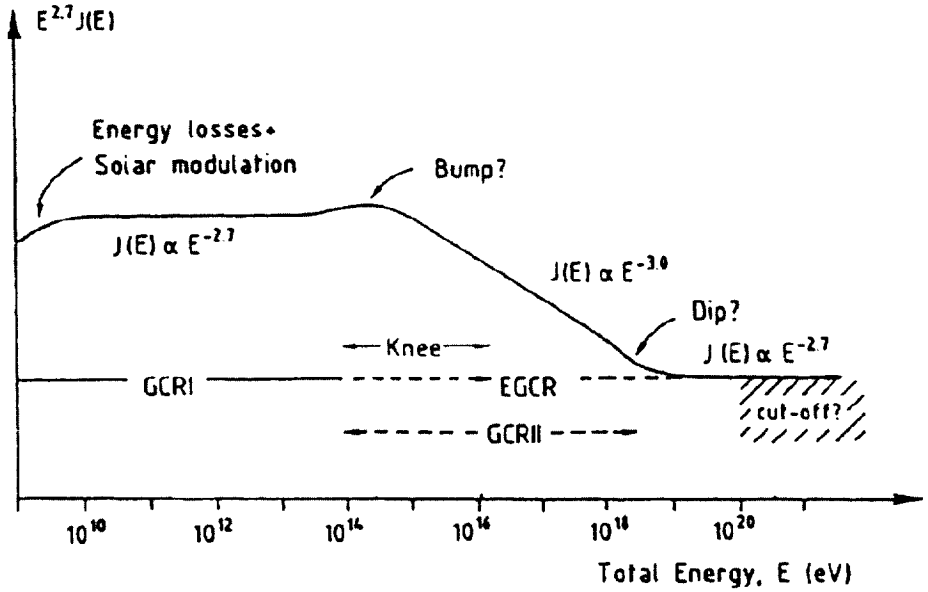

Figure 6.1: Schematic cosmic ray energy spectrum. The differential particle flux has been multiplied by $E_{cr}^{2.7}$ for presentation. (from: Axford 1992).

to the hypothesis that there is a transition from one dominant acceleration mechanism to another at about 10^{15} eV. This hypothesis is supported by the research presented here.*

6.1.2 Particle Acceleration by Supernova Remnants

In order to explain the origin of cosmic rays, Fermi (1949) introduced a mechanism of particle acceleration, whereby charged particles bounce off moving interstellar magnetic fields and either gain or lose energy, depending on whether the "magnetic mirror" is approaching or receding. In a typical environment (e.g. clouds in the ISM), he argued,

*It is important to note that the deflection of charged particles by the Galactic magnetic field makes it impossible to directly link particular cosmic rays with any particular source, so finding the origin of CRs is a non-trivial endeavor.

the probability of a head-on collision is greater than an overtaking collision, so particles would be accelerated on average. This random process is now called *2nd order Fermi acceleration*, because the mean energy gain per "bounce" is dependent on the "mirror" velocity squared.

On one hand Fermi's idea was plausible, because it naturally led to a power-law spectrum of particles. On the other hand, "energy budget" considerations demand that cosmic rays tap a greater source of energy than moving interstellar magnetic fields. Therefore, ter Haar (1950) proposed that supernovae produce high energy cosmic rays, while collisions in the ISM produced the power-law spectrum.

Following up on these ideas, Bell (1978) and Blandford & Ostriker (1978) independently applied Fermi's acceleration mechanism to SNR shocks. SNR shocks provided a particularly efficient means of accelerating particles, because the velocities are large and the motions are not random. A charged particle ahead of the shock front can pass through the shock and then be scattered by magnetic inhomogeneities behind the shock. The particle gains energy from this "bounce" and flies back across the shock, where it can be scattered by magnetic inhomogeneities ahead of the shock. This enables the particle to bounce back and forth again and again, gaining energy each time. This process is now called *1st order Fermi acceleration*, because the mean energy gain is dependent on the shock velocity only to the first power.[†]

Despite the acceptance of SNe as a major source of CRs, the details of the acceleration mechanisms, as well as the maximum energies of cosmic ray particles from SNRs, are still debated.[‡] Biermann (1995) argues that type I SNe account for cosmic ray protons with energies up to 10^{14} eV, with type II SNe accelerating CRs as far as 10^{17} eV. However, his predictions have not been verified. This work will investigate SNRs as sites

---

[†]An excellent detailed review of the physics of shock acceleration theory can be found in Blandford & Eichler (1987).

[‡]See Ellison *et al.* (1994) for a review of a conference on SNR shocks.

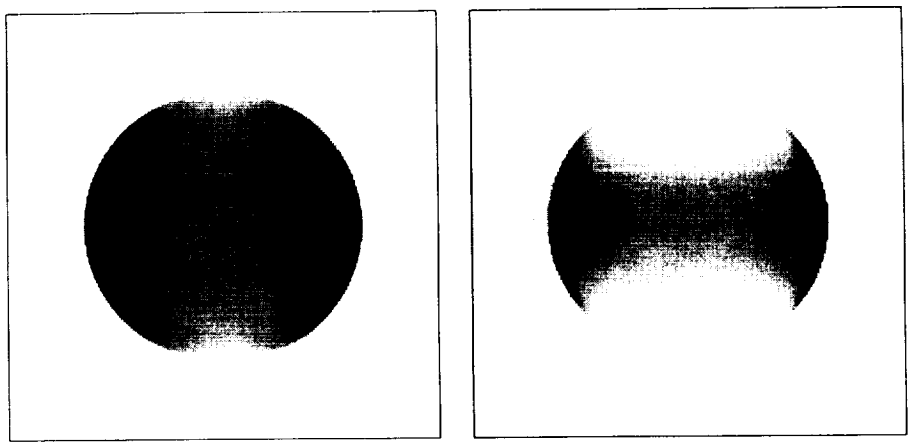

Figure 6.2: Theoretical synchrotron images assuming the quasi-perpendicular enhancement of Jokipii (1987). Notice the thinning of the bright shell between the radio map (left) and the corresponding X-ray map (right) (from: Reynolds, 1998).

of particle acceleration to 100 TeV (10^{14} eV) energies, within 1-2 decades of the knee of the cosmic ray spectrum, and put upper limits on the maximum electron energies in shell-type SNRs (chapter 7).

6.1.3 Synchrotron Radiation

The most successful indirect observational studies of cosmic rays have been by radio astronomers, who have studied *in situ* particle acceleration by observing synchrotron radiation from SNRs (e.g., Anderson & Rudnick 1993).

Synchrotron radiation is produced by relativistic electrons spiraling in a magnetic field.[§] The photon energy emitted from an individual electron is related to the magnetic field strength and its energy by:

$$E_{\rm photon} \approx 2\ keV \times \frac{B}{10\,\mu{\rm G}} \times \left(\frac{E_e}{100\ {\rm TeV}}\right)^2 \qquad (6.1)$$

Thus, radio studies probe electrons with energies in the MeV and GeV ranges, while

[§]The classic text on radiation mechanisms is Rybicki and Lightman (1979), but Shu (1991) is also excellent.

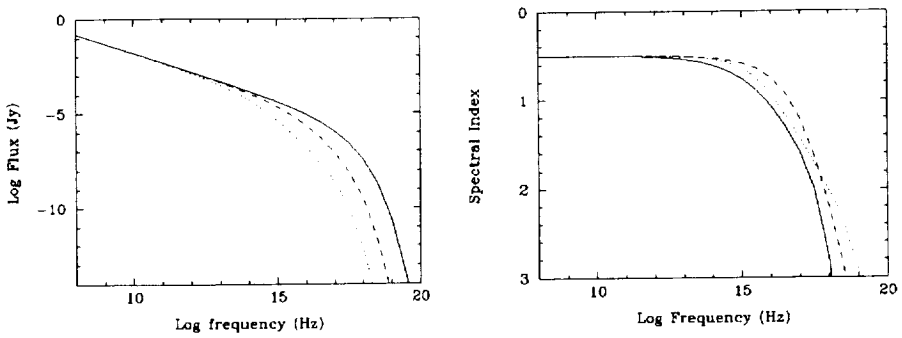

Figure 6.3: Model synchrotron spectra (left) and spectral indices (α, right), from Reynolds (1998). The different lines representing external magnetic fields ranging from 3–30 μG. The other parameters are typical for SNRs. Note, the photon indices we expect to measure in the X-ray range from $\Gamma = 2$–4.

100 TeV electrons emit X-rays in typical magnetic fields.[¶]

Between the radio and X-ray, synchrotron radiation from shell-type SNRs has been virtually impossible to detect due to absorption and domination by thermal emission. Reynolds & Chevalier (1981) modeled synchrotron radiation from type I SNRs in the adiabatic stage of evolution (*e.g.* Tycho's SNR and SN1006). Ammosov et al. (1994) also modeled the X-ray synchrotron spectrum for the SNRs Tycho and SN1006. More recently Reynolds (1996, 1998) has investigated SNR X-ray synchrotron radiation by producing a set of images (see Fig. 6.2) and spectra (see Fig. 6.3) given reasonable SNR parameters. Each of these calculations concludes that the synchrotron component may be, but is not necessarily, significant in the X-ray regime.

[¶]The canonical magnetic field of 10 μG is most-likely an underestimate for young SNRs (chapter 5).

6.2 Observing X-ray Synchrotron Radiation

6.2.1 Introduction

The ASCA satellite has made significant advances in the capabilities of X-ray astronomy. It combines moderate resolution spectroscopic capabilities, a large bandpass, and moderate imaging (appendix A). ASCA has a broader bandpass than the ROSAT PSPC detector, and it can distinguish between spectral line and continuum emission. This makes ASCA the natural instrument to compare the spectra of SNRs with modern non-equilibrium ionization (NEI) models. However, the observed X-rays come from both thermal and non-thermal components. Therefore, in order to model either emission mechanism appropriately, both components need to be accounted for.

ASCA Spectra

For the supernova remnants discussed in this PART, we attempt to find evidence to support either a thermal or non-thermal interpretation of the continuum emission. In general, a thermal X-ray spectrum should show a softer continuum spectrum than a non-thermal spectrum, as was observed in the XTE spectrum (10–50 keV) of Cas A (Allen et al. 1997). Unfortunately, in the ASCA bandpass (0.5–12 keV) analyses based only on spectral fitting cannot definitively distinguish between thermal and non-thermal emission. This uncertainty is largely because of our general lack of understanding of the thermal continuum emission. Specifically, sophisticated thermal models, with their multi-temperature structures, can reproduce power-law continua below 10 keV (e.g., Hamilton, Chevalier, & Sarazin 1983). To complicate things further, synchrotron models demonstrate concave-down curvature (Fig. 6.3), though to a lesser degree than the thermal models.

In light of the difficulty in distinguishing thermal from non-thermal emission, we investigate the possibility of synchrotron radiation through two opposite approaches:

- We make the assumption that the continuum is primarily thermal — then look for excess hard emission. (this chapter)

- We make the assumption that the continuum is primarily synchrotron radiation — then find the upper limit to each SNR's roll-off frequency and maximum electron energy. (chapter 7)

These two approaches differ in methodology as well as assumptions.

The method employed in this chapter requires the application of the best thermal model to a particular SNR. In general, young SNRs are so complex that pre-existing thermal models generally do not fit high quality ASCA data. Therefore, complex thermal modeling, customized to individual SNRs, is often carried out (e.g., Hamilton, Sarazin, & Szymkowiak 1986b; Decourchelle & Ballet 1994; Borkowski, Sarazin, & Blondin 1994; Borkowski et al. 1996). Unlike the existing models, these custom models usually fit the data quite well (at least within the targeted energy range), but they contain many free parameters. So while excess hard components are suggestive of synchrotron radiation, the ASCA spectra can usually be explained via a more complex thermal model.

ASCA Imaging

In addition to spectroscopy, ASCA has moderate imaging capability (appendix A). This allows the separate imaging of line and continuum emission. This has been performed for a number of SNRs, allowing the spatial separation of different components of the spectrum (e.g., Holt et al. 1994; Hwang & Gotthelf 1997). In chapter 8, we apply this method to the larger SNR, IC443, where we can clearly separate the hard continuum from the soft line-dominated emission.

In general, applying this technique to young SNRs is a dubious endeavor, because the thermal and non-thermal emissions are often well-correlated (PART I). However,

this is not the case for the SNRs W49 B and 3C 397, so we apply this technique to them below (§6.2.4, §6.2.6).

6.2.2 Synchrotron Dominated SNRs: SN 1006 & SN 393

Reynolds & Chevalier (1981) argued that the X-ray emission from the type I SNR, SN 1006, is dominated by synchrotron radiation extending naturally from the radio. Despite this argument, featureless thermal models were set forth to explain the same observations (Hamilton, Sarazin, & Szymkowiak 1986a).

The issue was finally resolved with ASCA. Koyama et al. (1995) found that SN 1006's rims are well-characterized by the featureless model, but the interior reveals the typical SNR emission lines (Fig. 6.4). This result is consistent with the synchrotron dominated spectrum, but not the thermal interpretation (Reynolds 1996; Laming 1998). The "final nail in the coffin," was the discovery of TeV energy gamma rays from SN 1006 (Tanimori et al. 1998). The origin of these gamma rays is consistent with inverse Compton up-scattering of cosmic microwave background photons off of TeV electrons.

In addition to SN 1006, a second continuum-dominated SNR has been discovered (Koyama et al. 1997), which is likely the guest star of 393 AD (Wang, Qu, & Chen 1997). A more in-depth study of SN 393 is underway (Slane et al. 1997), and promises interesting results.

6.2.3 The Importance of Hard Spectra: e.g. Cas A

Holt et al. (1994) completed an analysis of the ASCA PV phase data on Cas A, where they separated out a hard continuum component ($\approx 5\ keV$) and deconvolved the image to a resolution of 30″. One argument in favor of this continuum component being synchrotron is that it is more spatially similar to the the radio continuum than the X-ray line emission. However, this argument is weak because when absorption is taken into account the spatial correlation between the soft X-ray and radio is also quite

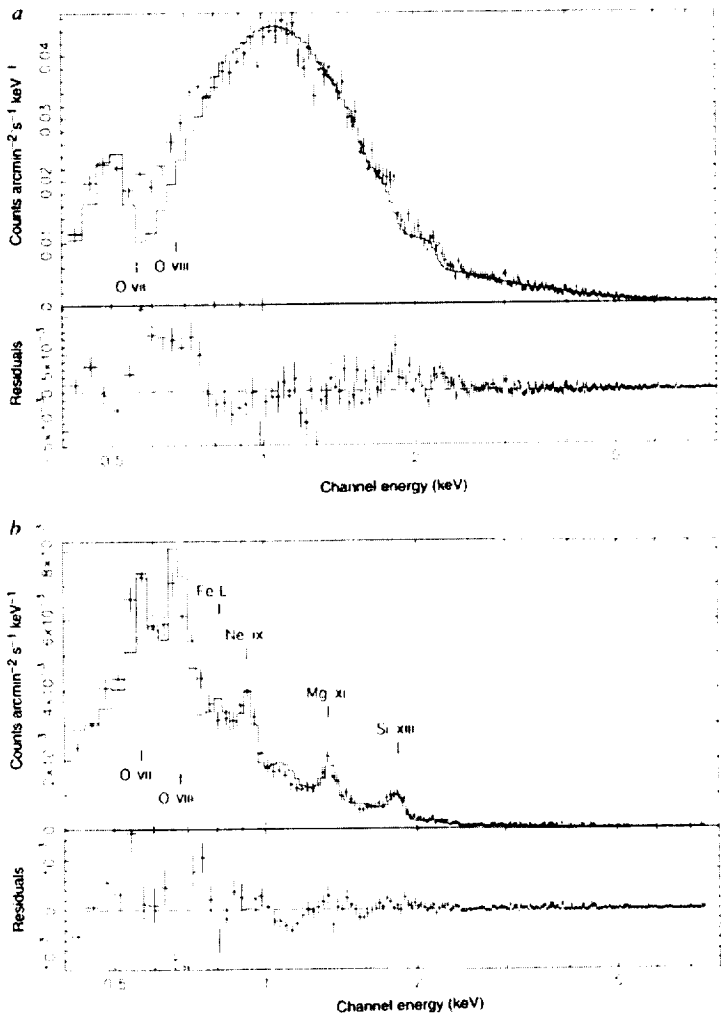

Figure 6.4: Two ASCA X-ray spectra of the SNR SN1006. Panel (a) is from the bright NE rim, while panel (b) is from the center of the SNR. (from: Koyama *et al.*, 1995).

good (PART I).

The solution is to observe Cas A with an instrument with a broader (harder) bandpass, because thermal emission falls off faster with increasing photon energy than does synchrotron. This was done using the Rossi X-ray Timing Explorer (RXTE) satellite.

Allen et al. (1997) present this RXTE observation and conclude from both the PCA and HEXTE data that the hard X-ray emission is dominated by synchrotron radiation. By combining OSSE (The et al. 1995, 1996) and SAX Favata et al. (1997) to the RXTE data, the spectral continuum of Cas A can be characterized by a single power-law with a photon index of about 3 in the 2–100 keV energy range.[‖] This combination of a relatively steep spectrum of more-or-less constant spectral index over almost two decades of frequency can only be interpreted as synchrotron emission.

6.2.4 W49 B

Fujimoto et al. (1995) analyzed the ASCA SIS data of W49 B and found that the spectrum could not be fit by a single plasma component — even when a non-equilibrium ionization model was used. They conclude that ASCA must be seeing a multi-temperature plasma mixture.

We have analyzed the ASCA GIS data and come to a slightly different conclusion. When we try to fit W49 B's GIS spectrum with a single plasma (Hamilton, Chevalier, & Sarazin 1983), we obtain a poor fit at the harder energies, however we can fit the spectrum better ($\Delta\chi^2 \approx 300$) with a single NEI plasma component plus a hard power-law (Fig. 6.5 & Tab. 6.1 on pp. 76 & 75).

While our thermal model is clearly overly simplistic, the data suggest an excess of hard emission. This suggests a possible non-thermal component. Currently there is no

[‖]Allen *et al.* assume a two temperature Raymond-Smith model to account for the ASCA emission, so they conclude that the additional synchrotron component must steepen with higher energy. This is not necessary if one assumes that the lines and continuum are produced by completely separate processes. For example the spectral lines could be produced by highly enriched clumpy ejecta, while the continuum is synchrotron dominated.

conclusive evidence to suggest that all the emission is thermal (as is often assumed), nor is there definitive evidence for a significant synchrotron component.

W49 B				
Model Component	Parameter	Value		Unit
Absorption	N_H	6.2	5.9	$\times 10^{22}$ cm^{-2}
Hamilton, Chevalier & Sarazin (1983)	Model #	103		
	He Abundance	-	-	solar
	C Abundance	-	-	solar
	N Abundance	-	1	solar
	O Abundance	-	1.5	solar
	Ne Abundance	-	1.2	solar
	Mg Abundance	33	28	solar
	Si Abundance	4.3	4.2	solar
	S Abundance	3.8	4.2	solar
	Ca Abundance	2.5	3.8	solar
	Fe Abundance	5.1	4.9	solar
	Ni Abundance	28	8.5	solar
	Normalization	8.7	8.0	$\times 10^{-3}$
Power-law	Photon Index	N/A	1.4	
	1 keV Flux Density	N/A	2	$\times 10^{-3}$ ph. cm^{-2} s^{-1} keV^{-1}

Table 6.1: The hard ASCA spectrum of W49 B fit primarily with the model of Hamilton, Chevalier & Sarazin (1983). An additional power-law component significantly ($\Delta\chi^2$=300) improved the fit. The fit without the hard component (left column) had χ^2=3012 with 859 degrees of freedom (χ^2_ν=3.6), while the fit with the hard component (right column) had χ^2=2715 with 859 degrees of freedom (χ^2_ν=3.2). The spectrum is shown in Fig. 6.5 (p. 76), and the parameters from a primarily non-thermal fit, to the same data, are shown on p. 101.

6.2.5 Kepler's SNR

Kepler's SNR (Kepler 1606) has been a case study for a number of theoretical models of non-equilibrium X-ray emission (Hughes & Helfand 1985; Decourchelle & Ballet 1994; Rothenflug et al. 1994; Borkowski, Sarazin, & Blondin 1994, hereafter BSB). Each of the 1994 models attempted to explain the EXOSAT observations of Smith et al. (1989), and each has its strengths and weaknesses.

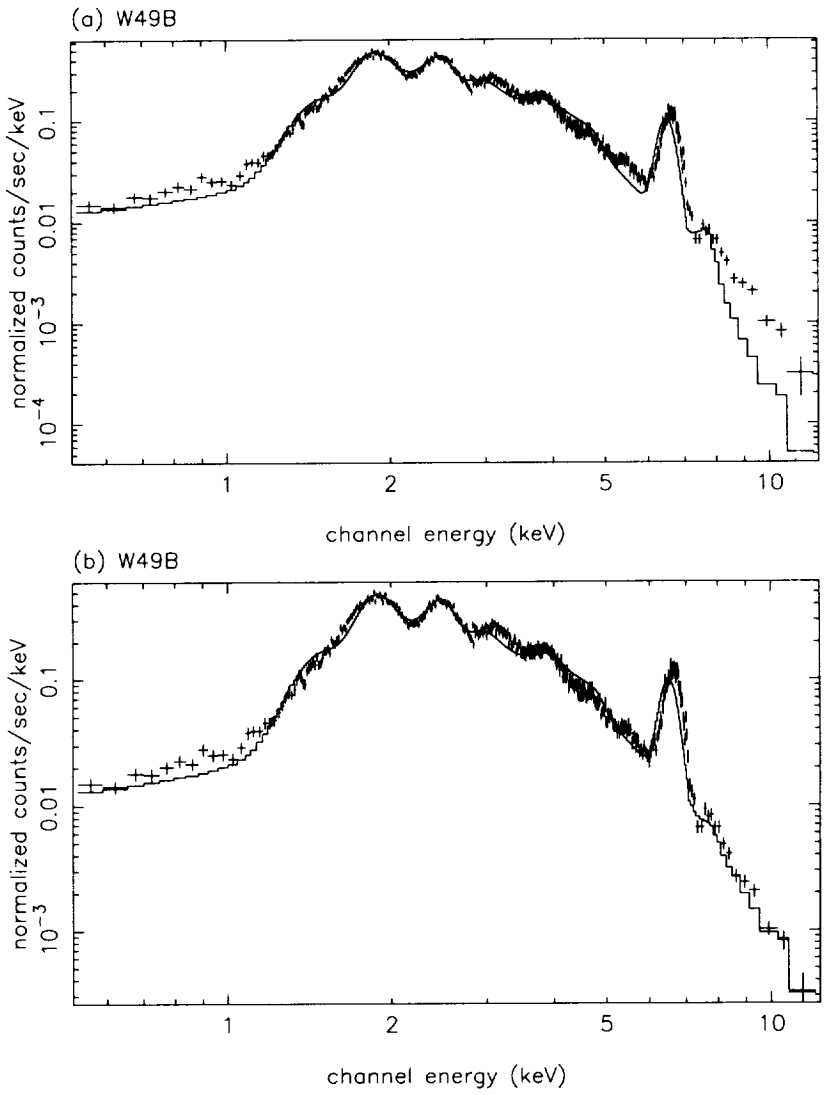

Figure 6.5: The folded ASCA GIS spectrum of W49 B with a thermal model fit. (a) The ASCA GIS data with the best-fit thermal NEI model (Hamilton, Chevalier & Sarazin 1983). (b) The same data with the best-fit thermal NEI model + a power-law. The fit parameters are shown in Tab. 6.1. These same data, fit with a primarily non-thermal model, are shown on p. 103.)

The goal of this analysis is to look for the possibility of an X-ray synchrotron continuum in addition to the thermally produced X-rays. As with the other SNRs featured in this chapter, we take the approach of first fitting the spectrum with a "best fit" thermal model and then determining if an additional component is necessary.

The model of BSB has had the best success in modeling the hard X-ray spectra, though their model does not (nor was it intended to) fit the data below 3.5 KeV. Therefore, we take BSB's model as our best-guess of the thermal spectrum, and then assess the need for an additional power-law component.

In the HEASARC ASCA archive there are two observations of Kepler's SNR with similar, but slightly different, pointing positions (see table 6.2). The data presented here are the *revision 2* spectra for both observations, and the background was selected by hand from off-source data in each observation. These are also the same data as shown on pp. 104–105.

The spectral analysis program XSPEC was used to simultaneously fit the four spectra restricting $E > 3.5$keV (Fig. 6.6). The best-fit model is shown in table 6.3.

	ad50032000		ad50032010	
	GIS 2	GIS 3	GIS 2	GIS 3
Total good Time (s)	18,503	18,437	16,417	16,417
Total good counts	61,360	68,615	53,303	60,415
Average cts/s	3.29	3.72	3.25	3.68

Table 6.2: ASCA observations of Kepler's SNR.

The Fe abundance and the power law spectral index are interdependent; as the modeled Fe abundance increases (i.e. the thermal continuum decreases), the power law component must also increase in order to fit the data. It is this coupling between the thermal continuum and the additional power law that is responsible for the bulk of the uncertainty (if BSB's model is correct).

The ASCA data of Kepler's SNR hint at the possibility of high energy synchrotron

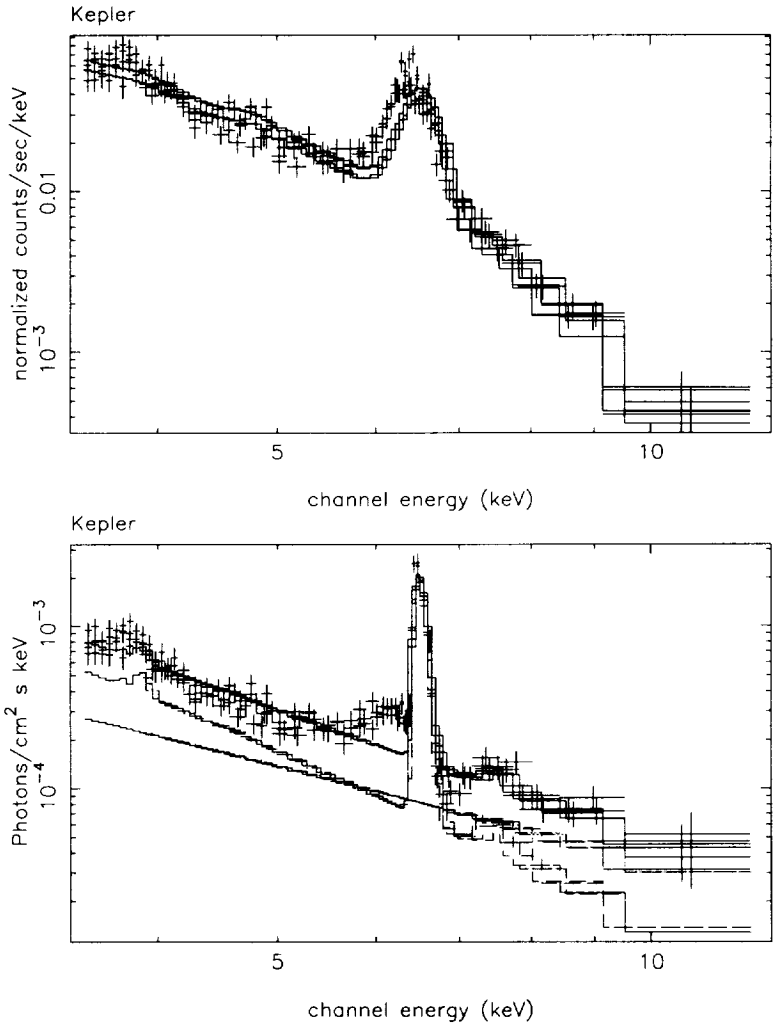

Figure 6.6: Kepler's ASCA GIS spectrum, fit using the model and parameters shown in Tab. 6.3.

Kepler's SNR		
Model Component	Parameter	Value
Absorption	N_H	5 $\times 10^{21}$ cm^{-2}
Borkowski, et al. (1994)	Fe Abundance	2.0 solar
	Normalization	0.94
Power-law	Photon Index	2
	1 keV Flux Density	3.5 $\times 10^{-3}$ ph. cm^{-2} s^{-1} keV^{-1}

Table 6.3: The hard ASCA spectrum of Kepler's SNR fit primarily with the model of Borkowski, Sarazin & Blondin (1994). An additional power-law component significantly ($\Delta\chi^2$=110) improved the fit. The fit had χ^2=538 with 356 degrees of freedom. The column density was frozen, while the other four parameters were allowed to float.

radiation from Kepler's SNR. However, our results do not rule out another thermal model with a slightly harder spectrum.

6.2.6 3C 397

The radio synchrotron emission from 3C 397 was well-studied by Anderson & Rudnick (1993) who analyzed the total intensity and spectral index variations across the SNR. Like W49B, 3C 397 is a young SNR that has a shell-type radio morphology and was apparently center-filled in soft X-rays. However, the most recent ROSAT HRI image reveals a small central X-ray component, while the rest of the SNR is morphologically similar to the radio (Dyer & Reynolds 1998).

Using public ASCA GIS data, we have performed an analysis of 3C 397 in a similar manner to W49B in §6.2.4. As Fig. 6.7 shows, a single component NEI model (Hamilton, Chevalier, & Sarazin 1983) does not fit the data as well as the synchrotron upper limit (plus ad hoc line emission) model in chapter 7 (pp. 106–107).

Spatially, we find that the hard X-ray continuum appears to follow the radio morphology (see Fig. 6.9). This would be either the case if a significant amount of hard continuum were synchrotron, or if the shell were preferentially absorbed.

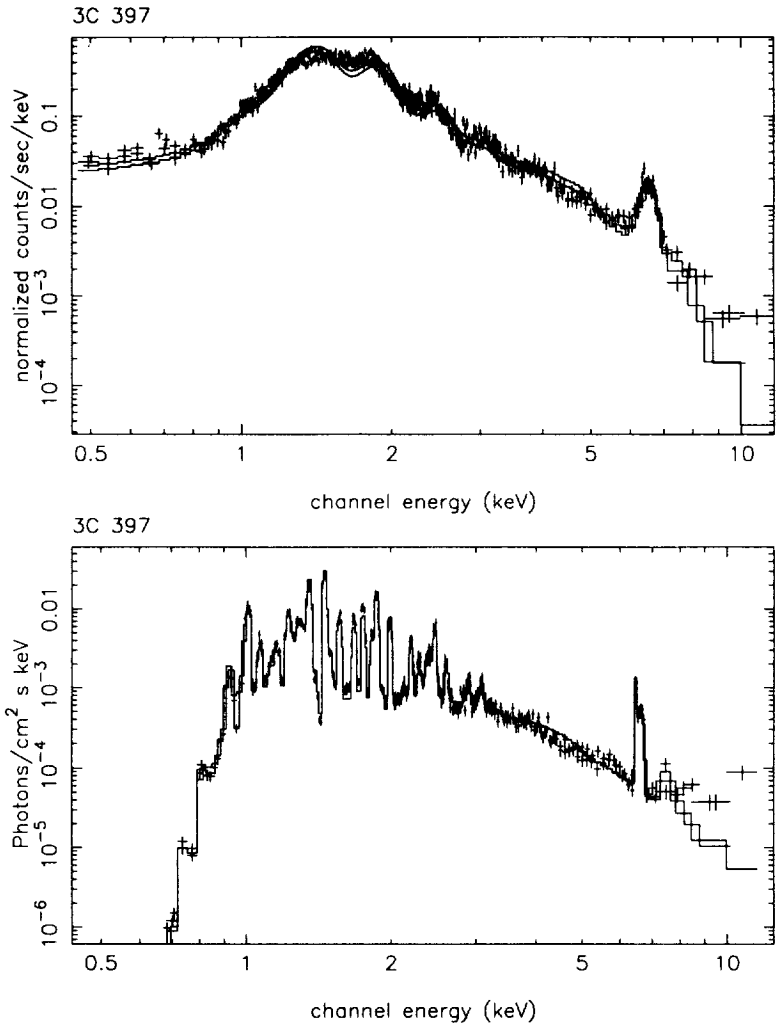

Figure 6.7: 3C 397's ASCA GIS spectrum, fit using the NEI model of Hamilton, Chevalier & Sarazin (1983). All the parameters were allowed to float independently for the best possible fit (Tab. 6.4, left column). The χ^2 of the fit was 1368 with 431 degrees of freedom (χ^2_ν=3.2)

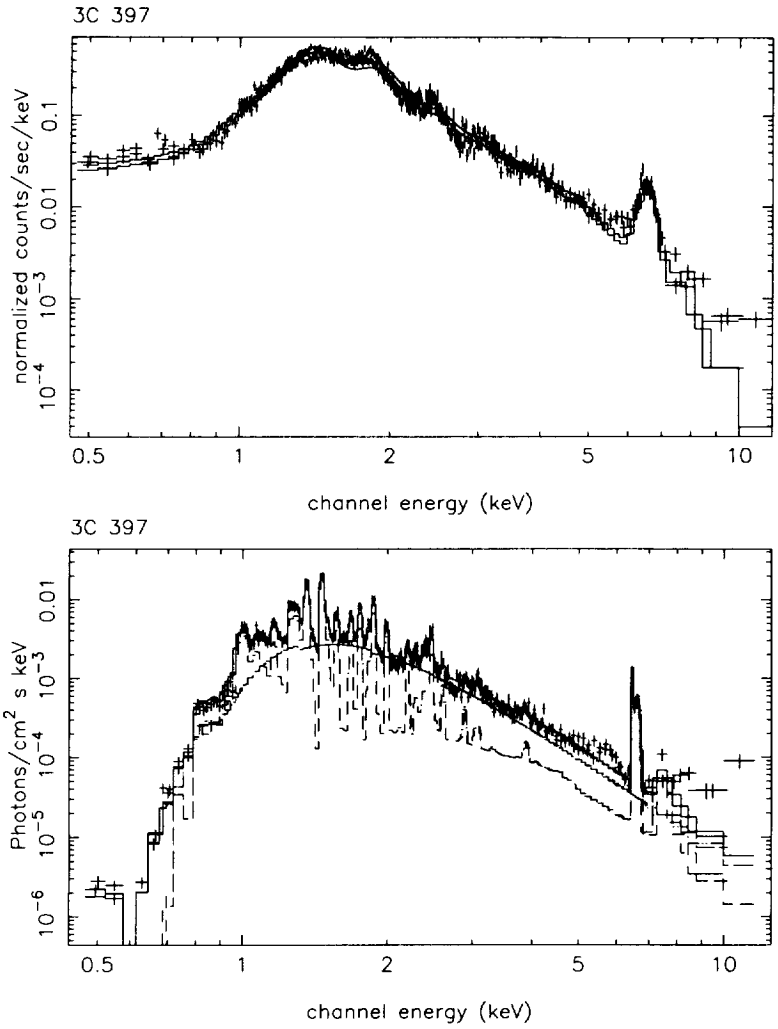

Figure 6.8: 3C397's ASCA GIS spectrum, fit using the NEI model of Hamilton, Chevalier & Sarazin (1983) plus a power-law. All the parameters were allowed to float independently for the best possible fit (Tab. 6.4, right column). The χ^2 of the fit was 1059 with 429 degrees of freedom (χ^2_ν=2.4)

3C 397				
Model Component	Parameter	Value		Unit
Absorption	$N_{\rm H}$	2.1	2.1	$\times 10^{22}$ cm^{-2}
Hamilton, Chevalier & Sarazin (1983)	Model #	95		
	He Abundance	-	-	solar
	C Abundance	-	-	solar
	N Abundance	-	-	solar
	O Abundance	-	-	solar
	Ne Abundance	-	-	solar
	Mg Abundance	70	99	solar
	Si Abundance	12	14	solar
	S Abundance	8	9	solar
	Ca Abundance	-	8	solar
	Fe Abundance	10	32	solar
	Ni Abundance	46	100	solar
	Normalization	12	4	$\times 10^{-4}$
Power-law	Photon Index	N/A	4.1	
	1 keV Flux Density	N/A	7	$\times 10^{-2}$ ph. cm^{-2} s^{-1} keV^{-1}

Table 6.4: The ASCA spectrum of 3C 397 fit primarily with the model of Hamilton, Chevalier & Sarazin (1983). An additional power-law component significantly ($\Delta\chi^2 \approx 300$) improved the fit. The fit without the hard component (left column) had $\chi^2=1369$ with 431 degrees of freedom ($\chi^2_\nu=3.2$), while the fit with the hard component (right column) had $\chi^2=1059$ with 429 degrees of freedom ($\chi^2_\nu=2.5$). The spectrum is shown in Figs. 6.7 & 6.8 (p. 80 & 81), and the parameters from a primarily non-thermal fit, to the same data, are shown on p. 106.

In conclusion, the spectra and images of 3C 397 are suggestive of synchrotron emission, but the ASCA data are still inconclusive.

6.3 Conclusion

The existence of X-ray synchrotron in a few cases has been well-established, but in the majority of SNRs the origin of the 1–10 keV continuum emission remains unclear. Synchrotron models can fit the 1–10 keV continuum acceptably (see chapter 7), but so can thermal models.

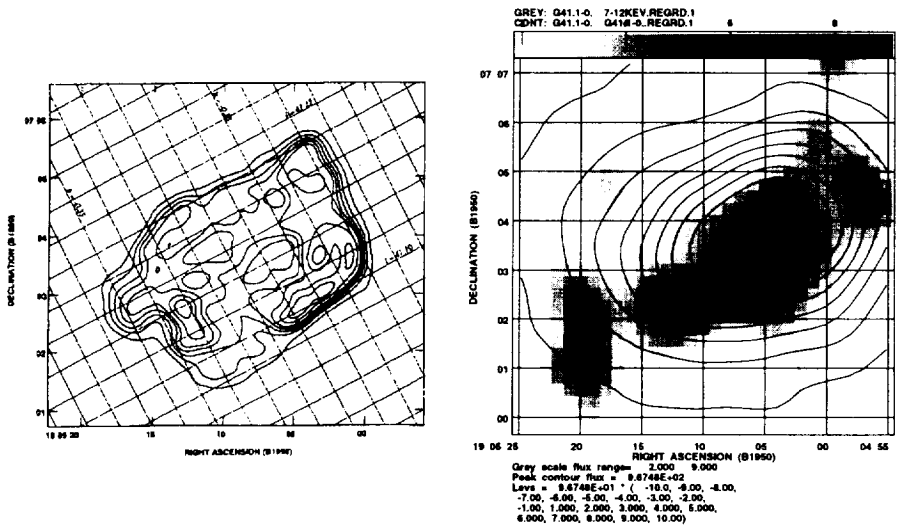

Figure 6.9: Images of 3C 397: (left) The $\lambda 20$ cm total intensity map of Anderson & Rudnick (1993); (right) ASCA GIS map of the 7–12 keV hard continuum; overlaid are contours of the total GIS intensity image. Note the hard continuum in the ASCA image overlays the $\lambda 20$ shell.

Currently, thermal X-ray emission models can be constructed to resemble the observed spectra of virtually any SNR, but future X-ray observations can help. Hard X-ray observations of more SNRs by RXTE and SAX can observe hard emission where thermal models do not predict it (e.g. Cas A). In addition, the spectral-imaging capabilities of AXAF will be able to observe morphological differences between continuum and line emission in small SNRs — as ASCA has done so successfully with the larger SNRs. In addition, the high spectral resolution promised by the next Japanese X-ray mission (Astro-E) should finally be able to resolve the structure of currently blended emission lines, thus providing measures of the thermal parameters (e.g. temperature, metallicity) independent of the shape of the thermal continuum.

Chapter 7

Maximum Energies of Shock-Accelerated Electrons in Young Shell Supernova Remnants

The key results from this chapter are in preparation as Reynolds & Keohane

7.1 Introduction

It is generally believed that Galactic cosmic rays are produced by SNRs (see chapter 6), via the Fermi acceleration process (see §6.1.2 on p. 66). The primary evidence for this has long been the pervasive radio synchrotron emission from SNRs, which imply the existence of electrons with energies up to about 10 GeV or so (also see §6.1.3 on p. 68). There appears to be no unambiguous evidence for the presence of cosmic-ray protons and nuclei (Allen et al. 1995), though recent EGRET γ-ray observations of a few supernova remnants (Esposito et al. 1996) have been interpreted as at least partly due to the decay of neutral pions produced by interactions of cosmic-ray protons with thermal gas (Drury, Aharonian, & Voelk 1994; Sturner et al. 1997; Baring et al. 1998). However, it is quite possible that the γ-rays originate from other sources within

its large field of view (e.g. pulsars). If the EGRET observations do represent diffuse shock-related emission, we finally will have evidence for the presence of ions at energies of 100 GeV or so.

However, recent X-ray observations of young supernova remnants have revealed non-thermal components, which have been generally interpreted as synchrotron radiation from the high-energy tail of the electron distribution as it rolls off at energies of 10 TeV and above. The presence of electrons at such extreme energies was confirmed for the remnant of SN 1006 by the discovery of TeV gamma rays (Tanimori et al. 1998, see p. 72), so we now have strong evidence for electrons with energies close to the "knee."

In this chapter, we select a sample of thirteen Galactic shell-type SNRs. This sample includes the brightest remnants both smaller than 10′ in diameter and with public ASCA data. In addition, similar calculations for SN1006 are referred to — making the sample 14 in total. Table 7.1 shows our sample in order of decreasing radio surface brightness, with their radio flux density and mean surface brightness, X-ray count rate and the radio flux density extrapolated to 1 keV (2.4×10^{17} Hz). The extrapolated flux density is derived from the radio flux density and spectral index; it represents what the synchrotron emission in the X-ray would be in the absence of any electron spectral steepening.

Our strategy is to find the upper limit to E_{max} for each SNR, by assuming that it contains a maximally curved nonthermal component. We emphasize that we do not assert that this component is physically required for these objects, simply that its value of the cut-off frequency is the highest allowable by the ASCA data. We do not propose to produce physical models for these objects. Our results show that while young SNRs are still likely to be the primary source of cosmic rays below the "knee," they cannot be used to explain the CR spectrum above the knee — or perhaps even that far. This is the first direct observational evidence that another source must be the primary accelerator of CRs above the knee.

Rank in Σ	Name(s)	1-GHz Flux Jy	Σ at 1 GHz Jy/□′	MPC[a] Rate cts/s	Extrapolated 1 keV Flux Den. mJy	$\frac{\text{photons}}{\text{s cm}^2\,\text{keV}}$	Page Numbers
1	Cas A	2720	140	109	0.9	1.5	90, 97–98
2	G349.7+0.2	20	5.1	N/A	1.3	2.0	90, 99–100
3	W49B	38	4.0	4.7	3.5	5.6	91, 101–103
4	Kepler	19	2.7	4.5	0.08	0.13	91, 104–105
5	3C397	22	2.5	2.5	2.0	3.2	91, 106–107
6	SN 386[b]	22	1.8	1.8	1.7	2.7	92, 108–109
7	Tycho	56	1.1	27.5	0.4	0.7	92, 110–112
8	3C 391	24	0.9	1.4	0.6	0.9	93, 113–114
10	3C 396	18	0.5	0.6	0.2	0.3	93, 115–116
11	Kes 73[b]	6	0.5	4.7	0.01	0.02	93, 117–118
12	RCW 103[b]	28	0.4	4.4	1.8	2.8	93, 119–120
21	G346.6-0.2	10	0.2	N/A	0.6	1.0	94, 121–122
22	G352.7-0.1	4	0.2	N/A	0.04	0.06	94, 123–124
56	SN 1006[c]	19	0.03	3.4	0.2	0.3	72

[a]We are showing the EINSTEIN Monitor Proportional Counter (MPC) count rate from Seward (1990), because it has the harder bandpass (1.5–20 keV).

[b]While classified as shell-type by Green, these SNRs have known central sources.

[c]While ASCA fits to SN 1006 is not presented in this chapter, it is the canonical synchrotron dominated SNR, so we are including it here for comparison.

Table 7.1: The top radio surface brightness shell-type SNRs in the Milky Way, which are smaller than 10′ in diameter and have public ASCA data. Sources of information are Green's catalogue (Green 1988) and Seward (1990).

7.2 The Common Analysis Technique

7.2.1 The Maximally Curved Model

The work here employs the maximally curved special case model of Reynolds (1998), who assumes that the electron spectrum is a power-law with an exponential cut-off — i.e.,

$$N_e(E) = K E_e^{-\gamma} e^{-E_e/E_{\max}} . \tag{7.1}$$

Reynolds found the most rapid possible synchrotron cutoff, by folding this distribution through the single-particle synchrotron emissivity, assuming a constant magnetic field. It is important to note that the actual emissivity expected rolls off slower than this model predicts. For example, any inhomogeneity in the remnant, such as a varying magnetic-field strength or a varying normalization K in Equation 7.1, will broaden the total spectrum, so these assumptions will give the highest possible value for $E_{\max}$ (given the radio constraints) for any observed X-ray spectrum.

This maximally curved model X-ray spectrum can then be characterized by three parameters:

- $S_{1\mathrm{GHz}}$, the 1 GHz radio flux density,
- α, the radio spectral index ($\gamma = 2\alpha + 1$), and
- $\nu_{\mathrm{roll-off}}$, the roll-off frequency.

Two of these parameters ($S_{1\mathrm{GHz}}$ and α) are radio-derived quantities, and have been well-measured over the years. In fact, both of these quantities are compiled in Green's catalogue (Green 1988). Therefore, this simplistic model yields a photon spectrum parameterized only by the radio spectrum and a maximum "roll-off frequency." The roll-off frequency is related to the cutoff electron energy via the standard synchrotron relation (see equation 6.1 on p. 68):

$$\nu_{\mathrm{roll-off}} \approx 0.5 \times 10^{16}\,\mathrm{Hz} \left(\frac{B}{10\,\mu\mathrm{G}}\right) \left(\frac{E_{\max}}{10\,\mathrm{TeV}}\right)^2 . \tag{7.2}$$

An X-ray spectrum of this model, with typical parameters, is shown in Fig. B.5 on page 157.

7.2.2 The Data

The analysis of all the SNRs presented in this chapter (except for Cas A) uses archival Gas Imaging Spectrometer (GIS) data from the ASCA observatory, and takes advantage of the recent *revision 2* batch data analysis (Pier 1997). For each ASCA pointing, the data are screened and spectra are extracted from circular regions around the source and the spectral channels are grouped so each bin has at least 40 counts. These spectra, along with their accompanying response functions, are provided with the *revision 2* data. Background spectra, however, are not provided in the standard processing.

For each SNR presented here, the extraction region of the standard processing was verified as encompassing the SNR. In each case the *revision 2* regions encompassed the SNR but excluded unnecessary excess background — just as one would draw them by hand.

Background spectra were produced by excluding the sources by hand from the *revision 2* screened event files, and extracting the leftover events. This was possible because only SNRs smaller than 10′ were included in this sample. It should be noted that imperfect background subtraction may cause an apparent excess in the very hard X-ray continuum ($E \gtrsim 7$ keV). This may affect the qualitative appearance of the very hard spectra, but it will not significantly alter the upper limits measured here.

7.2.3 The Spectral Fitting Methods

The spectra were fit with Reynolds' maximally curved model, plus an *ad hoc* thermal model consisting of only narrow gaussian emission lines, whose energies and line

strengths were both free parameters.* When necessary, an additional soft thermal bremsstrahlung component was added,† and in two cases (SN 393 & 3C 396) a very hard power-law component was needed to account for concave-up curvature. The standard Wisconsin absorption (Morrison & McCammon 1983) was applied to all ASCA fits.

7.2.4 Interpreting the Spectra

The results of this analysis are presented primarily in the tables and figures on pages 86–125. Tab. 7.1 shows the SNRs presented in this section and their basic information, while Tab. 7.28 summarizes the results of this analysis. The tables and figures in between show the individual results for each SNR.

For each SNR two tables and one figure are presented:

- A table of the best-fit model components and parameters.
- A table of the variation in the roll-off frequency with the radio flux and spectral index. This is the dominant source of uncertainty in the roll-off frequency.
- 0.5–11 keV (except Cas A) spectra. Both *folded* (i.e. detector) and *unfolded* (i.e. source) spectra are presented.

The sensitivity of X-ray spectrometers, such as the ASCA GIS, vary over their wavelength range. This *response function* is carefully measured and is now well-known for ASCA. Therefore, emission models must be *folded* through the response function before they can be compared to the data. The top spectrum in each figure is this

*As with the maximally curved model, this technique was chosen to preserve the derived upper limits, because blended spectral lines can mimic continuum emission. It is important that any ambiguous "continuum" emission be assumed to be synchrotron emission for these upper limits to be robust.

†This soft bremsstrahlung component is completely *ad hoc*, and in most cases takes into account the soft line emission (mostly Fe) below 1 keV. This is fine for the purposes here, because whatever is causing the excess soft emission seen in some SNRs, it is not synchrotron radiation.

folded spectrum, notice the two model lines representing the difference in the GIS2 and GIS3 response matrix (or in the case of Cas A, the PCA and HEXTE spectrometers on RXTE). In general, folded spectra show best how well the model fits the data.

Alternatively, the data can be *unfolded* back through the response function to be compared with the model. This *unfolded* spectrum shows the model in real flux density units (i.e. photons $cm^{-2}\,s^{-1}\,keV^{-1}$), and each term in the overall model is plotted separately on the unfolded spectra, so one can easily see the relative importance of each component. Note that these terms represent absorbed model components, so each term falls off toward the low energy end of the spectrum. However the *unfolding* process is less robust than the *folding* process, so close comparisons between the model and data are not advised with unfolded spectra.

7.3 Results

7.3.1 Cassiopeia A

Unlike all the other SNRs presented in this chapter, Cas A has been observed by RXTE and the data have been analyzed (Allen et al. 1997). Here I fit this RXTE spectrum of Cas A with Reynolds' simple synchrotron model, resulting in a good fit to both the PCA and HEXTE data (Tab. 7.2 & Fig. 7.1 on pp. 97-98). These result in a maximum electron value close to the knee of the CR spectrum.

7.3.2 G349.7+0.2

G349.7+0.2 is the second brightest (σ) shell-type SNR in the galaxy, and at a distance of 18 pc it has about 20% the radio luminosity of Cas A. G349.7+0.2's morphology is clearly shell-type (Shaver et al. 1985), and it is currently interacting with a molecular cloud (Frail et al. 1996).

Perhaps because of its small angular size and high column density (Tab. 7.4, p. 99)

G349.7+0.2 has not been well studied in the X-ray. In fact, the data presented here are from the Galactic ridge survey, as opposed to a pointed observation.

7.3.3 W49 B

In order to obtain an upper limit to the synchrotron emission from W49 B, the 95 ks spectrum was fit assuming that the 0.5–12.0 keV continuum is entirely synchrotron. Reynolds' synchrotron model was used to fit the continuum, and no other continuum component was required. A plot of the ASCA GIS spectrum with this model fit is shown in Fig. 7.3, and the model parameters are presented in Tab. 7.6 (p.101).

7.3.4 Kepler's SNR

Fig. 7.4 and Tab. 7.8 (pp. 104–105) show the ASCA GIS spectrum, and spectral fit parameters, assuming that the hard X-ray continuum is dominated by synchrotron radiation. In general this fit was rather poor, and required an excess soft component which though being line emission, was approximated with a very soft bremsstrahlung component. In general the maximum roll-off frequency was fairly high, but given the poor fit this is most-likely due to excess hard thermal X-ray emission.

Kepler's SNR was also discussed earlier in chapter 6 (p. 75).

7.3.5 3C 397

3C 397 (G41.1-0.3) is a young shell-type SNR which has, as of yet, no pulsar detection. On page 79 the possibility of an excess hard component in 3C 397 is discussed. In this chapter, the GIS spectrum is fit using the synchrotron model and gaussian lines (Tab 7.10 & Fig. 7.5 on pp. 106–107).

7.3.6 SN 386

The SNR G11.2-0.3 (SN 386, Clark & Stephenson 1977; Green et al. 1988; Reynolds et al. 1994) is a shell-type SNR in the radio and soft X-ray (Becker, Markert, & Donahue 1985; Green et al. 1988; Reynolds et al. 1994). However, Vasisht et al. (1996) found a centrally peaked hard source within SN 386 with ASCA, and argued that it contains an embedded plerion. The measured photon index of the hard source was dependent on the thermal X-ray model used, but was about 1.5. Later, Torii et al. (1997) found a sinusoidal modulation in the ASCA data with a period of 65 milliseconds, thus confirming the pulsar interpretation. Torii et al. (1997) also measure the best-fit photon index as a function of pulsar phase (assuming the soft emission is thermal), and they find variations from Γ=1.6 to 2.1. When they subtract the off-phase from the on-phase spectra, they measure a photon index for the pulsar of 0.6.

The spectral fitting method used here also implies a hard central source, assuming that the bulk of the shell emission is synchrotron dominated. The continuum emission was well fit using a simple two component, completely non-thermal model, where the softer emission was fit using Reynolds' synchrotron model and the hard emission by a simple power-law (Fig. 7.6, p. 109). The best-fit hard component, assuming a synchrotron-dominated soft continuum, resulted in a photon index of 0.5 (Tab. 7.12, p. 108) — in remarkable agreement with the pulsar spectral index of 0.6.

7.3.7 Tycho's SNR

The supernova of 1572 is thought to be a Type Ia SNR based on Brahe's light curve (Brahe 1573). It has been extremely well studied, especially in the X-ray (e.g., Hamilton, Sarazin, & Szymkowiak 1986b; Brinkmann et al. 1989; Vancura, Gorenstein, & Hughes 1995; Hwang & Gotthelf 1997; Hwang, Hughes, & Petre 1998). Given that much of this work utilized ASCA observations, it was not surprising that the quality of the public GIS data is very good (see Fig. 7.7, p. 112). It is remarkable how good a fit

is obtained by these maximally-curved models to the hard continuum.

7.3.8 3C 391

The SNR 3C 391 is remarkably well fit using this non-thermal model — with $\chi^2_\nu \approx 1.2$ (Tab. 7.16 on p. 113). As with the other SNRs, this hints that its continuum may be synchrotron dominated. The soft thermal bremsstrahlung, naturally, accounts for the soft excess which is most likely line emission.

7.3.9 3C 396

The SNR 3C 396 is similar to 3C 391, except there is a significant hard excess, which cannot be explained as a background subtraction problem (pp. 115–116). We have added an extra, very-hard component to characterize this, however the nature of this component is unknown. It may be an embedded pulsar, it may be an inverse-Compton component, or there could be another explanation.

7.3.10 Kes 73 & RCW 103

Kes 73 and RCW 103 are two radio shell-type SNRs where central X-ray sources have recently been confirmed (Gotthelf & Vasisht 1997; Vasisht & Gotthelf 1997; Gotthelf, Petre, & Hwang 1997).

The ASCA spectrum of Kes 73 was well fit using the same methods as the other SNRs in the chapter, but the resultant maximum roll-off frequency is over an order of magnitude greater than the other SNRs (see Tab. 7.20 & Fig. 7.10 on pages 117 & 118). Our method of finding upper limits for the roll-off frequency remains valid, because these central sources are radio-quiet; however if a central source is dominating the hard X-ray emission the upper limit may be anomalously high.

Similarly RCW 103's central source (Gotthelf, Petre, & Hwang 1997) also most likely

dominates the hard emission. The roll-off frequency upper limit is not very high, however (see Tab. 7.28, p. 125). RCW 103 did prove particularly hard to fit. For similar reasons as Kes 73, it was impossible to fit the soft emission with the synchrotron model. As with the other SNRs, excess non-synchrotron X-ray emission, whatever its origin, only lowers the roll-off frequency — allowing the upper limit to stand.

7.3.11 G346.6-0.2 & G352.7-0.1

G346.6-0.2 and G352.7-0.1 are less famous SNRs which exhibit lower radio surface brightness than the other SNRs presented in this chapter (and lower X-ray flux), but still are fairly bright compared with the other SNRs in Green's catalogue. Both objects were observed during the survey of the Galactic ridge (as opposed to a dedicated pointing), and the data are not of the same quality as their counterparts. The synchrotron model fits these SNRs well, but that could easily be due to the quality of the data. For the purposes of measuring an upper limit on the roll-off frequency, these spectra are adequate. As with all of these SNRs, the errors are dominated by the error in the radio spectral index.

7.3.12 SN 1006

One historical shell remnant, SN 1006, has too low a radio surface brightness, and is too large, to qualify for our sample. However, SN 1006 is the one SNR whose X-ray spectrum is known to be actually produced by synchrotron radiation. While its spectrum rolls off more slowly than our maximally curved spectrum due to inhomogeneities, we can treat the calculated ν_m of the model (Reynolds 1996) as equivalent to the upper limits we quote for the rest of the remnants. This value is included in Table 7.28.

7.4 Conclusion

None of these supernova remnants has X-ray emission bright enough to lie on the extrapolation of its radio spectrum (except perhaps Kes 73). Thus the spectrum of electrons responsible for the radio emission must steepen or cut off before reaching X-ray emitting energies. We derive upper limits to the cutoff energies using the most sharply cut-off physically reasonable model, the synchrotron emissivity of a power-law electron spectrum with an exponential cutoff. Those upper limits are listed for 13 remnants with some of the highest radio surface brightnesses in the Galaxy (Tab. 7.28). In all cases, the electron spectrum must steepen well below the "knee" in the cosmic-ray spectrum. Possible explanations include:

1. These remnants are not currently producing cosmic rays, but may in the future as they age.

2. Their electron spectra cut off sooner than their proton spectra (e.g. synchrotron losses dominate).

3. Supernova remnants do not produce Galactic cosmic rays even to within an order of magnitude of the "knee".

We stress that the fundamental source of the limits, the fact that all supernova remnants in our sample are fainter in X-rays than the extrapolated radio spectrum, is completely model-independent. We have taken the sharpest possible physically reasonable cutoff in the electron spectrum to find the highest frequency at which the electron spectrum could begin to cut off and still not exceed the observed X-rays. We emphasize that our limits are limits; the true turnover frequencies could be still lower.

We plan to extend this work as new X-ray observations become available. Cruder limits can be obtained from integrated X-ray flux observations of older, larger remnants, and we intend to attempt this. However, these results should cause some discomfort in

the particle-acceleration community. If our thirteen objects are typical of the supernova remnants that produce cosmic rays, the canonical picture of Galactic cosmic-ray origin may need substantial revision.

Cassiopeia A			
Model	Parameter	Value	Source
Absorption	$N_{\rm H}$	1×10^{22} cm^{-2}	Chap. 4
Reynolds' Synchrotron Model	$S_{\rm 1GHz}$	2720 Jy	Green's catalogue
	α	0.77	Green's catalogue
	max $\nu_{\rm roll\,off}$	3.15×10^{17} Hz	this RXTE fit

Table 7.2: The best-fit upper-limit on the roll-off frequency ($\nu_{\rm roll\,off}$) assuming that the X-ray spectrum above 10 keV is produced exclusively by synchrotron radiation. This is probably a good assumption for Cas A (Allen, et al. 1997). This fit had $\chi^2 = 290$ for 105 degrees of freedom. In addition the normalization was allowed to float on only the HEXTE component (higher energy spectrum) to account for well-known problems with early HEXTE calibration. The spectrum is shown in Fig. 7.1.

$\alpha \downarrow S_{\rm 1GHz} \rightarrow$	2700	2710	2720	2730	2740
0.62	4.6	4.6	4.6	4.6	4.6
0.67	7.7	7.7	7.7	7.6	7.6
0.72	14	14	14	14	14
0.77	32	32	**31.5**	31	31
0.82	95	95	95	94	94
0.87	610	600	600	590	590

Table 7.3: The best-fit roll-off frequency of Cas A ($\times 10^{16}$ Hz) as a function of radio flux density (Jy) and spectral index.

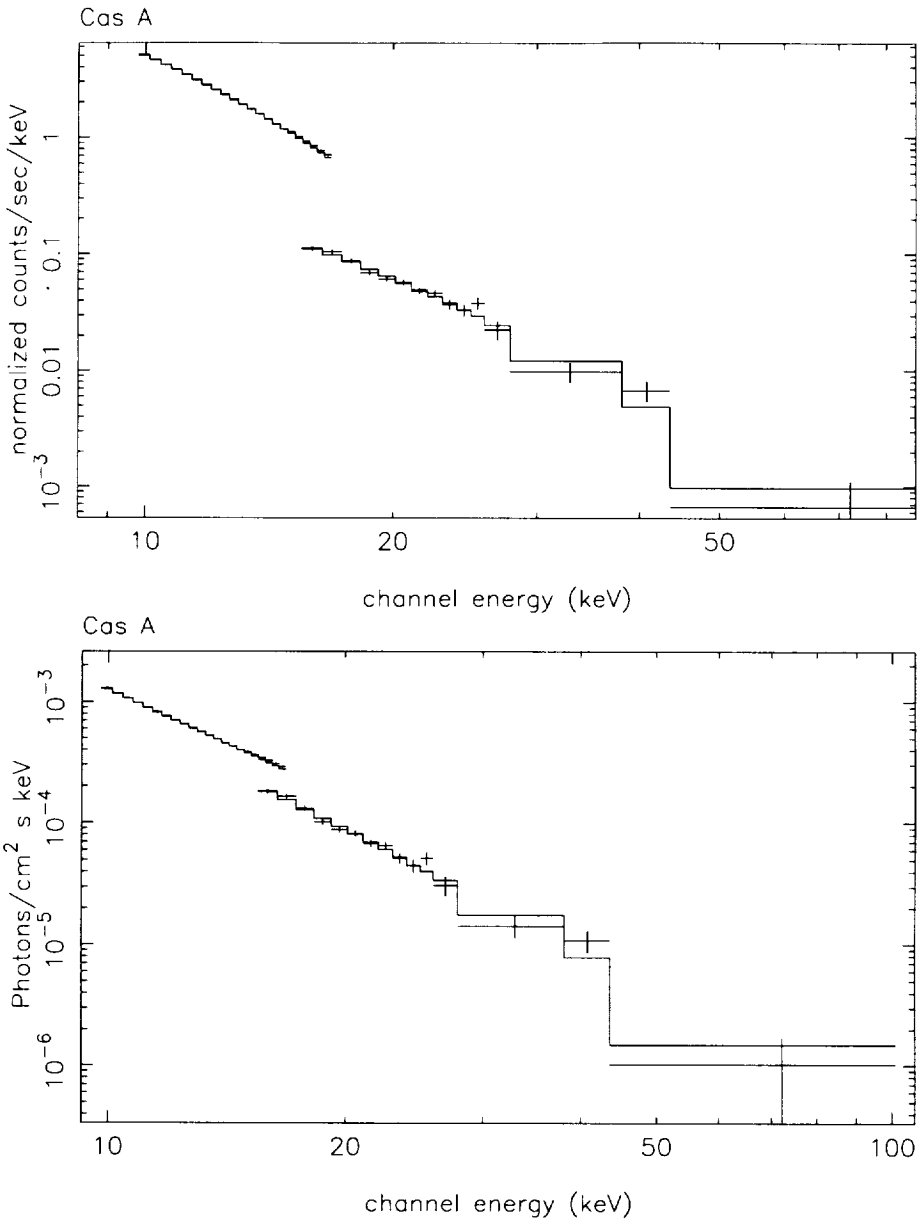

Figure 7.1: Folded (top) and unfolded (bottom) RXTE spectra of Cas A with the parameters in Tab. 7.2 used in the fit. This is to fit the best-fit upper-limit synchrotron component. The ASCA GIS spectrum is continuous with the RXTE PCA spectrum, implying good overall PCA calibration. On the other hand, the HEXTE spectrum required an overall normalization adjustment to match the PCA spectrum in their overlapping region; this is the source of the gap in the above spectrum.

G349.7+0.2		
Model Component	Parameter	Value
Absorption	$N_{\rm H}$	4.0×10^{22} $\rm cm^{-2}$
Reynolds' Synchrotron Model	$S_{\rm 1GHz}$	20 Jy
	α	0.5
	max $\nu_{\rm roll\,off}$	1.8×10^{16} Hz
Narrow Gaussian	$F_{\rm line}$	1.0×10^{-3} $\rm ph.cm^{-2}s^{-1}$
	Line Energy	1.9 keV
Narrow Gaussian	$F_{\rm line}$	8×10^{-4} $\rm ph.cm^{-2}s^{-1}$
	Line Energy	2.4 keV
Narrow Gaussian	$F_{\rm line}$	1.5×10^{-4} $\rm ph.cm^{-2}s^{-1}$
	Line Energy	3.1 keV
Narrow Gaussian	$F_{\rm line}$	5×10^{-5} $\rm ph.cm^{-2}s^{-1}$
	Line Energy	6.8 keV

Table 7.4: The best-fit spectrum of G349.7+0.2, assuming that synchrotron radiation is the primary source of X-ray continuum emission. This fit had $\chi^2 = 125$ for 110 degrees of freedom ($\chi^2_\nu = 1.1$). The radio flux and spectral index were taken from Green's catalogue, and frozen during the X-ray fitting. The spectrum is shown on page 100.

$\alpha \downarrow S_{\rm 1GHz} \rightarrow$	18	19	20	21	22
0.40	0.9	0.8	0.8	0.8	0.8
0.45	1.2	1.2	1.2	1.2	1.2
0.50	1.9	1.8	**1.8**	1.8	1.7
0.55	3.1	3.0	2.9	2.8	2.8
0.60	5.5	5.3	5.1	5.0	4.9

Table 7.5: The best-fit roll-off frequency of G349.7+0.2 ($\times 10^{16}$ Hz) as a function of radio flux density (Jy) and spectral index.

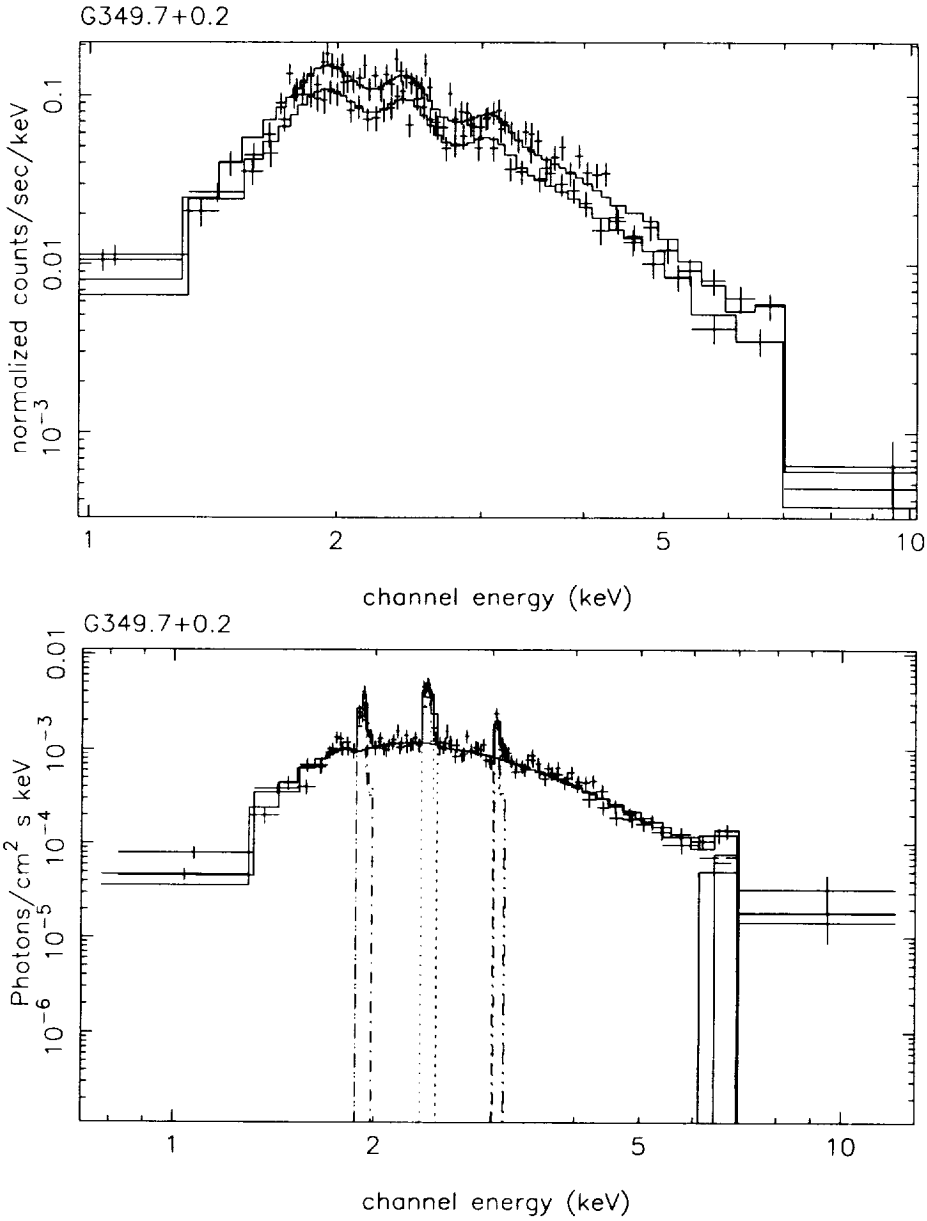

Figure 7.2: Folded (top) and unfolded (bottom) spectra of G349.7+0.2 with the parameters in Tab. 7.4 used in the fit.

W49B		
Model Component	Parameter	Value
Absorption	$N_{\rm H}$	4.1×10^{22} cm^{-2}
Reynolds' Synchrotron Model	$S_{\rm 1GHz}$	38 Jy
	α	0.5
	max $\nu_{\rm roll\,off}$	2.5×10^{16} Hz
Narrow Gaussian	$F_{\rm line}$	3.7 ph.cm^{-2}s^{-1}
	Line Energy	0.97 keV
Narrow Gaussian	$F_{\rm line}$	1.3×10^{-2} ph.cm^{-2}s^{-1}
	Line Energy	1.4 keV
Narrow Gaussian	$F_{\rm line}$	3.9×10^{-3} ph.cm^{-2}s^{-1}
	Line Energy	1.7 keV
Narrow Gaussian	$F_{\rm line}$	5.0×10^{-3} ph.cm^{-2}s^{-1}
	Line Energy	1.9 keV
Narrow Gaussian	$F_{\rm line}$	3.0×10^{-3} ph.cm^{-2}s^{-1}
	Line Energy	2.5 keV
Narrow Gaussian	$F_{\rm line}$	6.7×10^{-4} ph.cm^{-2}s^{-1}
	Line Energy	3.1 keV
Narrow Gaussian	$F_{\rm line}$	1.6×10^{-4} ph.cm^{-2}s^{-1}
	Line Energy	3.5 keV
Narrow Gaussian	$F_{\rm line}$	4.3×10^{-4} ph.cm^{-2}s^{-1}
	Line Energy	3.9 keV
Narrow Gaussian	$F_{\rm line}$	1.2×10^{-3} ph.cm^{-2}s^{-1}
	Line Energy	6.6 keV
Narrow Gaussian	$F_{\rm line}$	8×10^{-5} ph.cm^{-2}s^{-1}
	Line Energy	7.8 keV
Narrow Gaussian	$F_{\rm line}$	5×10^{-5} ph.cm^{-2}s^{-1}
	Line Energy	9.0 keV

Table 7.6: The best-fit spectrum of W49B, assuming that the synchrotron radiation is the primary source of X-ray continuum emission. This fit had χ^2=996 for 835 degrees of freedom (χ^2_ν=1.2). The radio flux and spectral index were taken from Green's catalogue, and frozen in the X-ray fit. The spectrum is shown on page 103. The roll-off frequency as a function of the radio parameters is tabulated on page 102. The results from an NEI fit to the same data are shown on page 75.

$\alpha \downarrow S_{1\mathrm{GHz}} \rightarrow$	36	37	38	39	40
0.40	1.1	1.1	1.0	1.0	1.0
0.45	1.6	1.6	1.5	1.5	1.5
0.50	2.5	2.5	**2.5**	2.4	2.4
0.55	4.4	4.3	4.2	4.2	4.1
0.60	8.9	8.7	8.5	8.4	8.2

Table 7.7: The best-fit roll-off frequency of W49 B ($\times 10^{16}$ Hz) as a function of radio flux density (Jy) and spectral index.

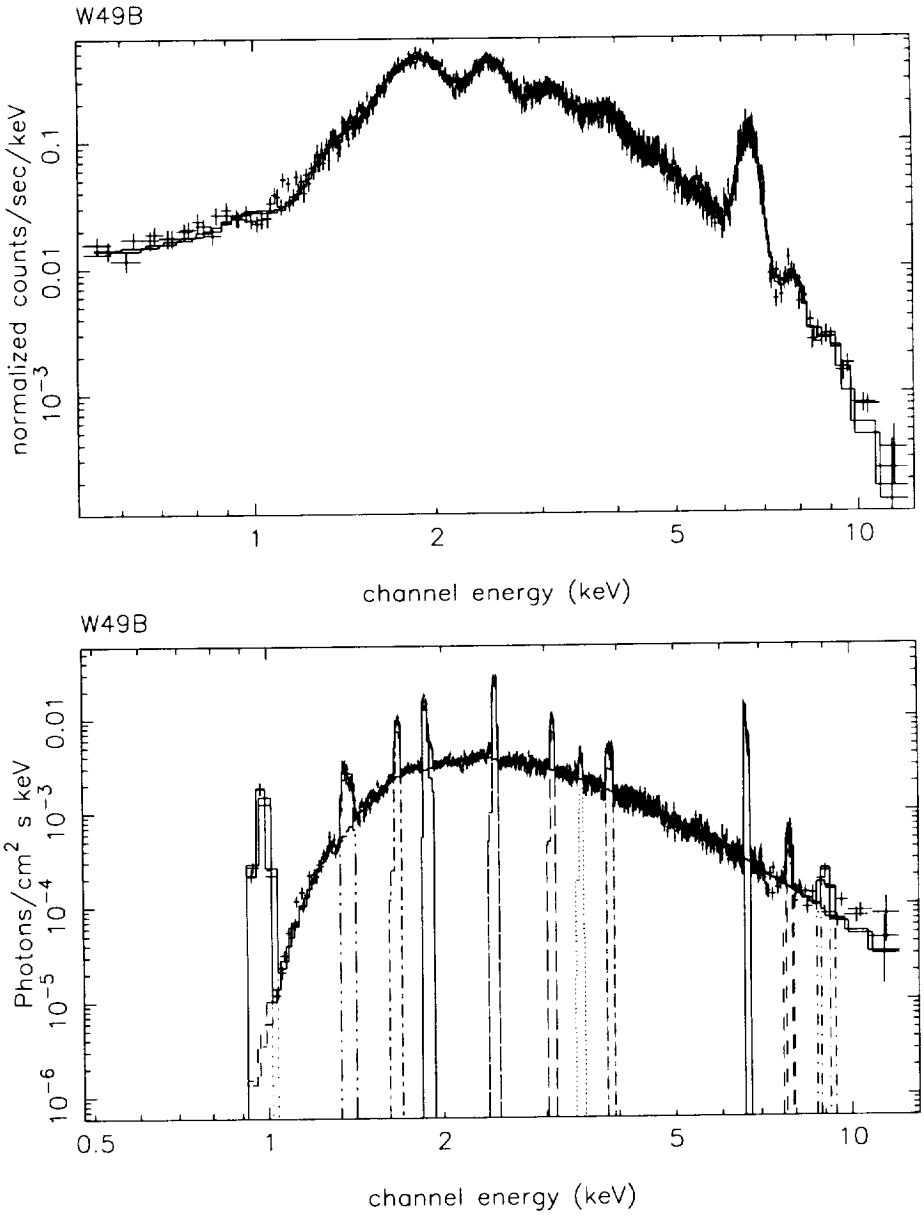

Figure 7.3: Folded (top) and unfolded (bottom) spectra of W49 B with the parameters in Tab. 7.6 used in the fit. This is to fit the best-fit upper-limit synchrotron component. The same data, fit with a primarily thermal model, are shown on page 76.

Kepler's SNR			
Model Component	Parameter	Value	
Absorption	$N_{\rm H}$	6.7×10^{21}	$\rm cm^{-2}$
Reynolds' Synchrotron Model	$S_{\rm 1GHz}$	19	Jy
	α	0.64	
	max $\nu_{\rm roll\,off}$	1.1×10^{17}	Hz
Thermal Bremsstrahlung	kT	0.14	keV
	Normalization	233	
Narrow Gaussian	$F_{\rm line}$	1.0×10^{-2}	$\rm ph.cm^{-2}s^{-1}$
	Line Energy	1.8	keV
Narrow Gaussian	$F_{\rm line}$	1.7×10^{-3}	$\rm ph.cm^{-2}s^{-1}$
	Line Energy	2.2	keV
Narrow Gaussian	$F_{\rm line}$	2.2×10^{-3}	$\rm ph.cm^{-2}s^{-1}$
	Line Energy	2.4	keV
Narrow Gaussian	$F_{\rm line}$	3.8×10^{-4}	$\rm ph.cm^{-2}s^{-1}$
	Line Energy	3.0	keV
Narrow Gaussian	$F_{\rm line}$	5.6×10^{-5}	$\rm ph.cm^{-2}s^{-1}$
	Line Energy	3.7	keV
Narrow Gaussian	$F_{\rm line}$	4.0×10^{-4}	$\rm ph.cm^{-2}s^{-1}$
	Line Energy	6.4	keV

Table 7.8: The best-fit spectrum of Kepler's SNR, assuming that synchrotron radiation is the primary source of X-ray continuum emission. This fit had $\chi^2 = 1260$ for 405 degrees of freedom (χ^2_ν=3.1). The radio flux and spectral index were taken from Green's catalogue, and frozen during the X-ray fitting. The spectrum is shown on page 105.

$\alpha \downarrow S_{\rm 1GHz} \rightarrow$	17	18	19	20	21
0.54	3.1	3.0	2.9	2.8	2.7
0.59	5.7	5.5	5.3	5.1	5.0
0.64	12.4	11.8	**11.3**	10.8	10.4
0.69	35.2	32.9	30.9	29.2	27.6
0.74	183	163	146	132	121

Table 7.9: The best-fit roll-off frequency of Kepler's SNR ($\times 10^{16}$ Hz) as a function of radio flux density (Jy) and spectral index.

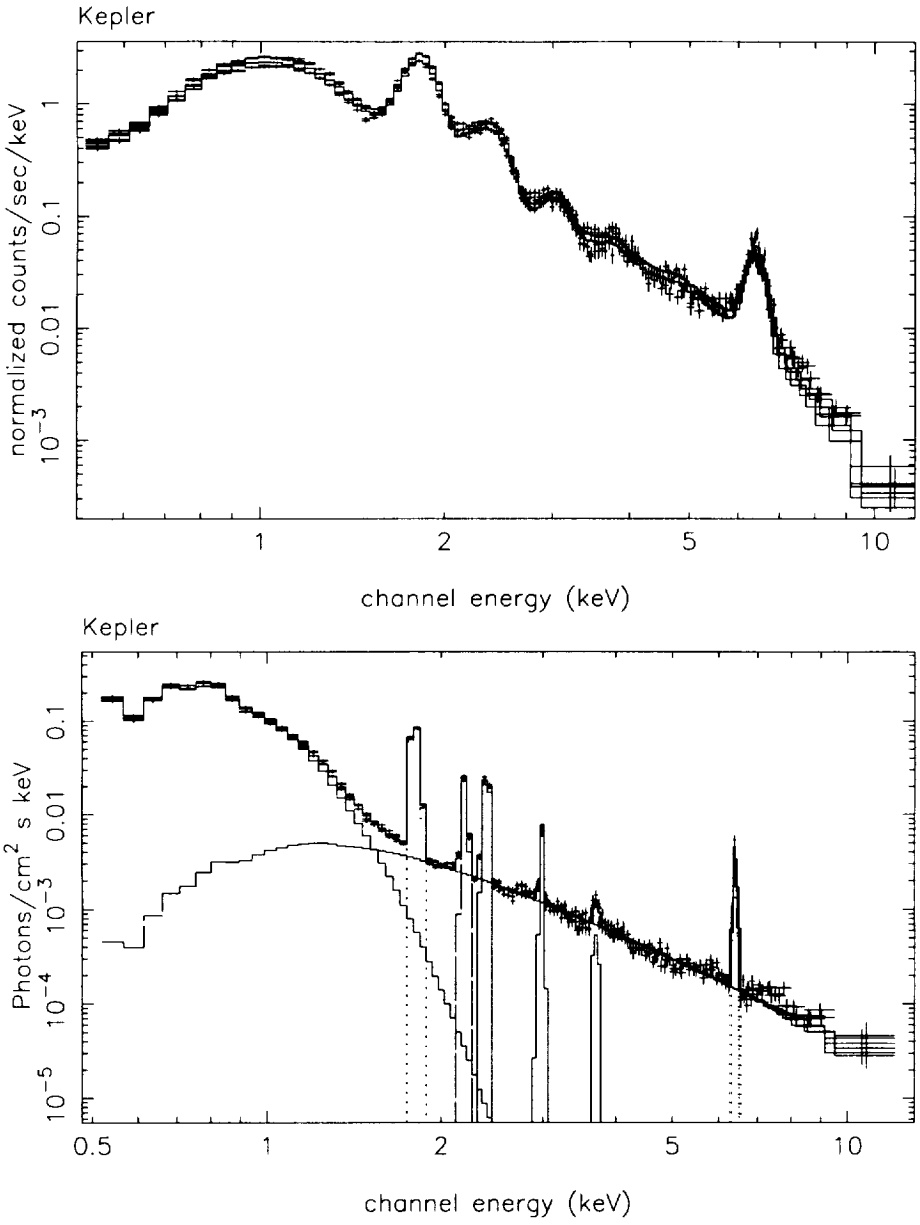

Figure 7.4: Folded (top) and unfolded (bottom) ASCA spectra of Kepler with the parameters in Tab. 7.8 used in the fit. This is to fit the best-fit upper-limit synchrotron component. Notice the harder continuum component is the maximally curved synchrotron model, while the soft continuum is an additional thermal bremsstrahlung component.

3C 397		
Model Component	Parameter	Value
Absorption	$N_{\rm H}$	8×10^{21} cm^{-2}
Reynolds' Synchrotron Model	$S_{\rm 1GHz}$	22 Jy
	α	0.59
	max $\nu_{\rm roll\,off}$	3.4×10^{16} Hz
Narrow Gaussian	$F_{\rm line}$	1.2×10^{-3} ph.cm^{-2}s^{-1}
	Line Energy	1.3 keV
Narrow Gaussian	$F_{\rm line}$	2.0×10^{-3} ph.cm^{-2}s^{-1}
	Line Energy	1.4 keV
Narrow Gaussian	$F_{\rm line}$	1.2×10^{-3} ph.cm^{-2}s^{-1}
	Line Energy	1.8 keV
Narrow Gaussian	$F_{\rm line}$	3.4×10^{-4} ph.cm^{-2}s^{-1}
	Line Energy	2.3 keV
Narrow Gaussian	$F_{\rm line}$	1.9×10^{-4} ph.cm^{-2}s^{-1}
	Line Energy	6.5 keV

Table 7.10: The best-fit spectrum of 3C 397, assuming that synchrotron radiation is the primary source of X-ray continuum emission. This fit had $\chi^2 = 793$ for 432 degrees of freedom (χ^2_ν=1.8). The radio flux was taken from Green's catalogue, and the radio spectral index from Anderson & Rudnick (1993); both radio parameters were frozen during the X-ray fitting. The spectrum is shown on page 107.

$\alpha \downarrow S_{\rm 1GHz} \rightarrow$	20	21	22	23	24
0.49	1.3	1.2	1.2	1.2	1.2
0.54	2.0	2.0	2.0	1.9	1.9
0.59	3.6	3.5	**3.4**	3.3	3.2
0.64	7.2	6.9	6.7	6.5	6.3
0.69	18	17	16	15	15

Table 7.11: The best-fit roll-off frequency of 3C 397 ($\times 10^{16}$ Hz) as a function of radio flux density (Jy) and spectral index.

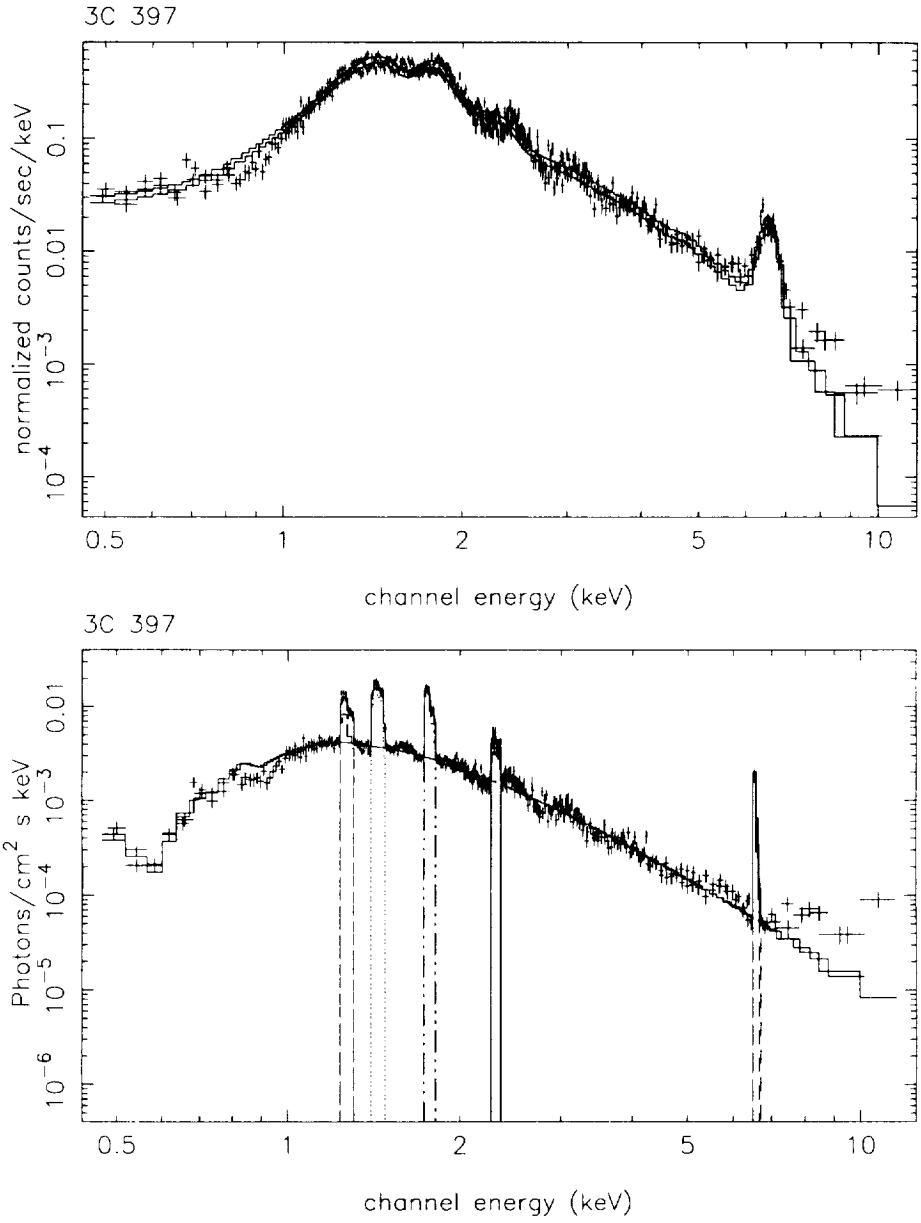

Figure 7.5: Folded (top) and unfolded (bottom) spectra of 3C397 with the parameters in Tab. 7.10 used in the fit.

SN 386		
Model Component	Parameter	Value
Absorption	$N_{\rm H}$	1.0×10^{22} $\rm cm^{-2}$
Reynolds' Synchrotron Model	$S_{\rm 1GHz}$	22 Jy
	α	0.49
	max $\nu_{\rm roll\,off}$	1.3×10^{16} Hz
Narrow Gaussian	$F_{\rm line}$	2×10^{-3} $\rm ph.cm^{-2}s^{-1}$
	Line Energy	1.3 keV
Narrow Gaussian	$F_{\rm line}$	3×10^{-3} $\rm ph.cm^{-2}s^{-1}$
	Line Energy	1.8 keV
Narrow Gaussian	$F_{\rm line}$	9×10^{-4} $\rm ph.cm^{-2}s^{-1}$
	Line Energy	2.4 keV
Narrow Gaussian	$F_{\rm line}$	3×10^{-5} $\rm ph.cm^{-2}s^{-1}$
	Line Energy	6.7 keV
Very Hard Power-Law	1 keV flux density	2.0×10^{-4} $\rm ph.cm^{-2}s^{-1}keV^{-1}$
	Photon Index	0.50

Table 7.12: The best-fit spectrum of SN 386 (G11.2-0.3), assuming that synchrotron radiation is the primary source of X-ray continuum emission except for the pulsar component at the hardest energies. This fit had $\chi^2 = 277$ for 216 degrees of freedom (χ^2_ν=1.3). The radio flux and spectral index were taken from Green's catalogue, and frozen during the X-ray fitting. The spectrum is shown on page 109. The very hard power-law component is most likely the pulsar, as is discussed on p. 92

$\alpha \downarrow$ $S_{\rm 1GHz} \rightarrow$	20	21	22	23	24
0.39	0.585	0.574	0.564	0.546	0.546
0.44	0.886	0.863	0.844	0.827	0.812
0.49	1.39	1.35	**1.32**	1.29	1.27
0.54	2.34	2.28	2.22	2.17	2.12
0.59	4.34	4.21	4.08	3.96	3.87

Table 7.13: The best-fit roll-off frequency of SN 386 ($\times 10^{16}$ Hz) as a function of radio flux density (Jy) and spectral index.

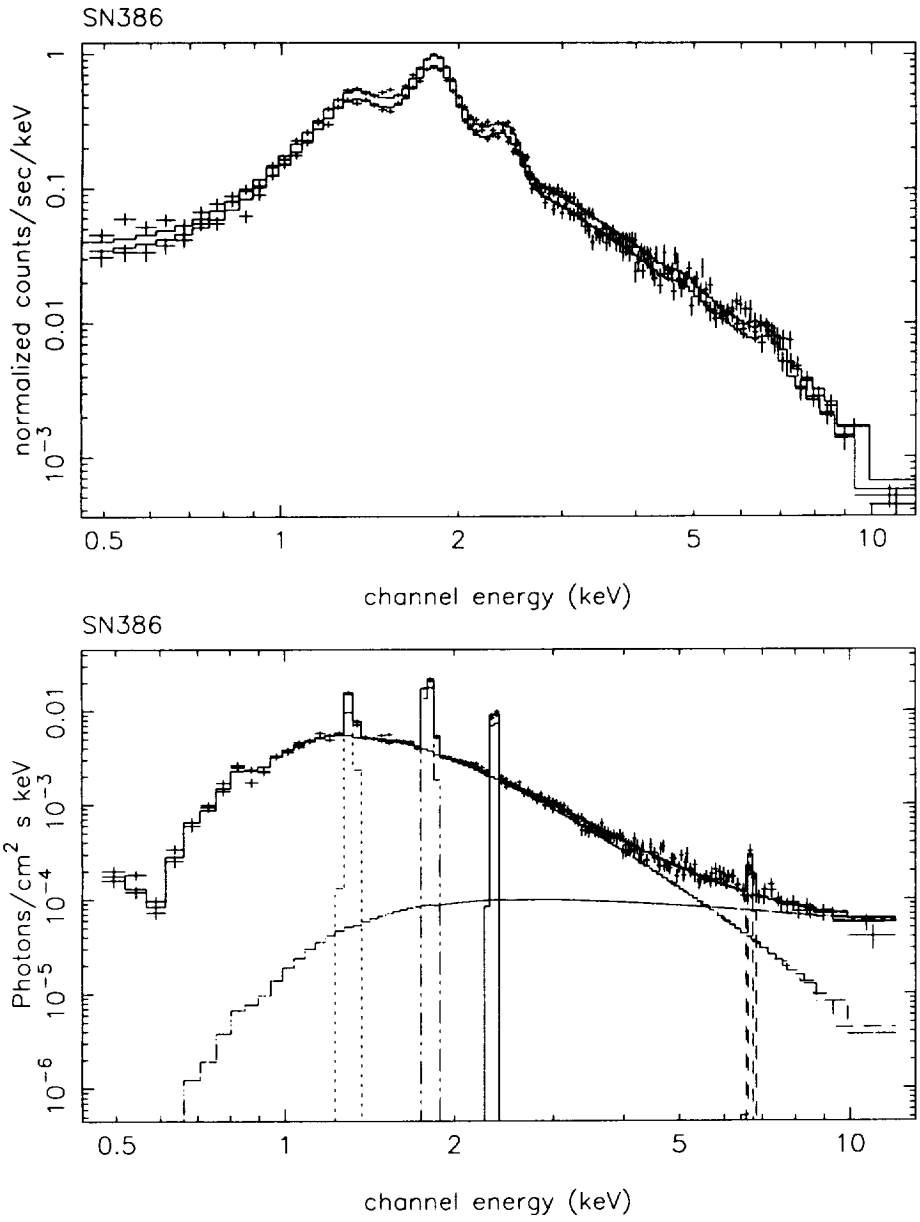

Figure 7.6: Folded (top) and unfolded (bottom) spectra of SN 386 with the parameters in Tab. 7.12 used in the fit.

Tycho's SNR		
Model Component	Parameter	Value
Absorption	$N_{\rm H}$	5.2×10^{21} cm^{-2}
Reynolds' Synchrotron Model	$S_{\rm 1GHz}$	56 Jy
	α	0.61
	max $\nu_{\rm roll\,off}$	8.8×10^{16} Hz
Thermal Bremsstrahlung	kT	0.17 keV
	Normalization	53
Narrow Gaussian	$F_{\rm line}$	5.6×10^{-3} ph.cm^{-2}s^{-1}
	Line Energy	1.3 keV
Narrow Gaussian	$F_{\rm line}$	7.5×10^{-2} ph.cm^{-2}s^{-1}
	Line Energy	1.8 keV
Narrow Gaussian	$F_{\rm line}$	8.2×10^{-3} ph.cm^{-2}s^{-1}
	Line Energy	2.1 keV
Narrow Gaussian	$F_{\rm line}$	2.1×10^{-2} ph.cm^{-2}s^{-1}
	Line Energy	2.4 keV
Narrow Gaussian	$F_{\rm line}$	1.3×10^{-3} ph.cm^{-2}s^{-1}
	Line Energy	2.8 keV
Narrow Gaussian	$F_{\rm line}$	2.1×10^{-3} ph.cm^{-2}s^{-1}
	Line Energy	3.0 keV
Narrow Gaussian	$F_{\rm line}$	5.2×10^{-4} ph.cm^{-2}s^{-1}
	Line Energy	3.8 keV
Narrow Gaussian	$F_{\rm line}$	6.5×10^{-4} ph.cm^{-2}s^{-1}
	Line Energy	6.4 keV

Table 7.14: The best-fit spectrum of Tycho, assuming that synchrotron radiation is the primary source of X-ray continuum emission. This fit had $\chi^2 = 5130$ for 1984 degrees of freedom (χ^2_ν=2.6). The radio flux and spectral index were taken from Green's catalogue, and frozen during the X-ray fitting. The spectrum is shown on page 112. The roll-off frequency as a function of the radio parameters is tabulated on page 111.

$\alpha \downarrow S_{1\mathrm{GHz}} \rightarrow$	54	55	56	57	58
0.51	2.3	2.3	2.3	2.3	2.3
0.56	4.3	4.3	4.2	4.2	4.1
0.61	9.1	8.9	**8.8**	8.7	8.6
0.66	24	23	23	22	22
0.71	95	92	90	87	85

Table 7.15: The best-fit roll-off frequency of Tycho's SNR ($\times 10^{16}$ Hz) as a function of radio flux density (Jy) and spectral index.

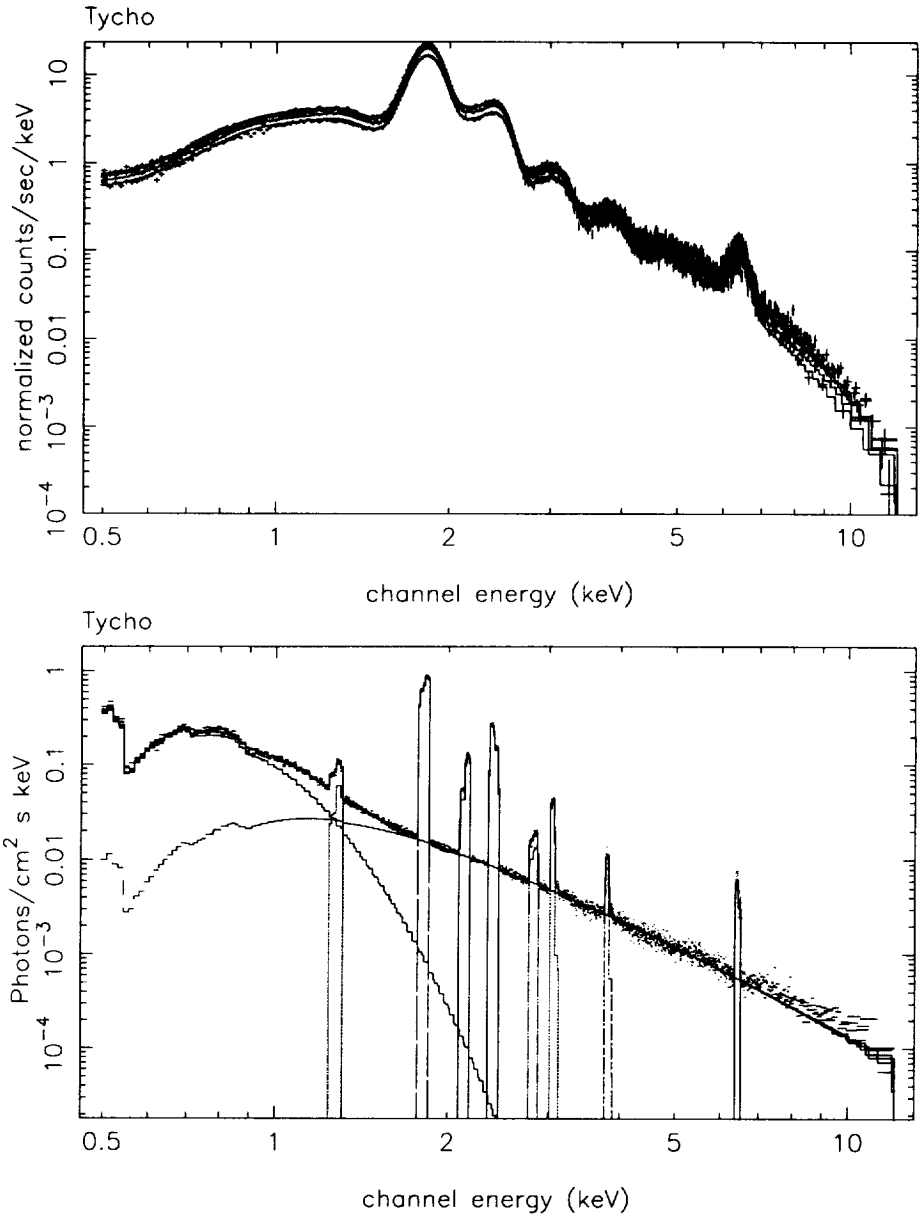

Figure 7.7: Folded (top) and unfolded (bottom) spectra of Tycho's SNR with the parameters in Tab. 7.14 used in the fit.

3C391		
Model Component	Parameter	Value
Absorption	$N_{\rm H}$	1.3×10^{22} $\rm cm^{-2}$
Reynolds' Synchrotron Model	$S_{\rm 1GHz}$	24 Jy
	α	0.55
	max $\nu_{\rm roll\,off}$	1.4×10^{16} Hz
Thermal Bremsstrahlung	kT	0.4 keV
	Normalization	0.17
Narrow Gaussian	$F_{\rm line}$	4×10^{-4} $\rm ph.cm^{-2}s^{-1}$
	Line Energy	1.4 keV
Narrow Gaussian	$F_{\rm line}$	9×10^{-4} $\rm ph.cm^{-2}s^{-1}$
	Line Energy	1.8 keV
Narrow Gaussian	$F_{\rm line}$	2×10^{-4} $\rm ph.cm^{-2}s^{-1}$
	Line Energy	2.4 keV
Narrow Gaussian	$F_{\rm line}$	1×10^{-6} $\rm ph.cm^{-2}s^{-1}$
	Line Energy	4.2 keV
Narrow Gaussian	$F_{\rm line}$	3×10^{-5} $\rm ph.cm^{-2}s^{-1}$
	Line Energy	6.8 keV

Table 7.16: The best-fit spectrum of 3C 391, assuming that synchrotron radiation is the primary source of X-ray continuum emission. This fit had $\chi^2 = 352$ for 273 degrees of freedom (χ^2_ν=1.3). The radio flux and spectral index were taken from Green's catalogue, and frozen during the X-ray fitting. The spectrum is shown on page 114.

$\alpha \downarrow S_{\rm 1GHz} \rightarrow$	22	23	24	25	26
0.45	0.68	0.67	0.66	0.65	0.64
0.50	0.96	0.95	0.93	0.92	0.91
0.55	1.5	1.4	1.4	1.4	1.4
0.60	2.4	2.3	2.3	2.2	2.2
0.65	4.2	4.1	4.0	3.9	3.8

Table 7.17: The best-fit roll-off frequency of 3C 391 ($\times 10^{16}$ Hz) as a function of radio flux density (Jy) and spectral index.

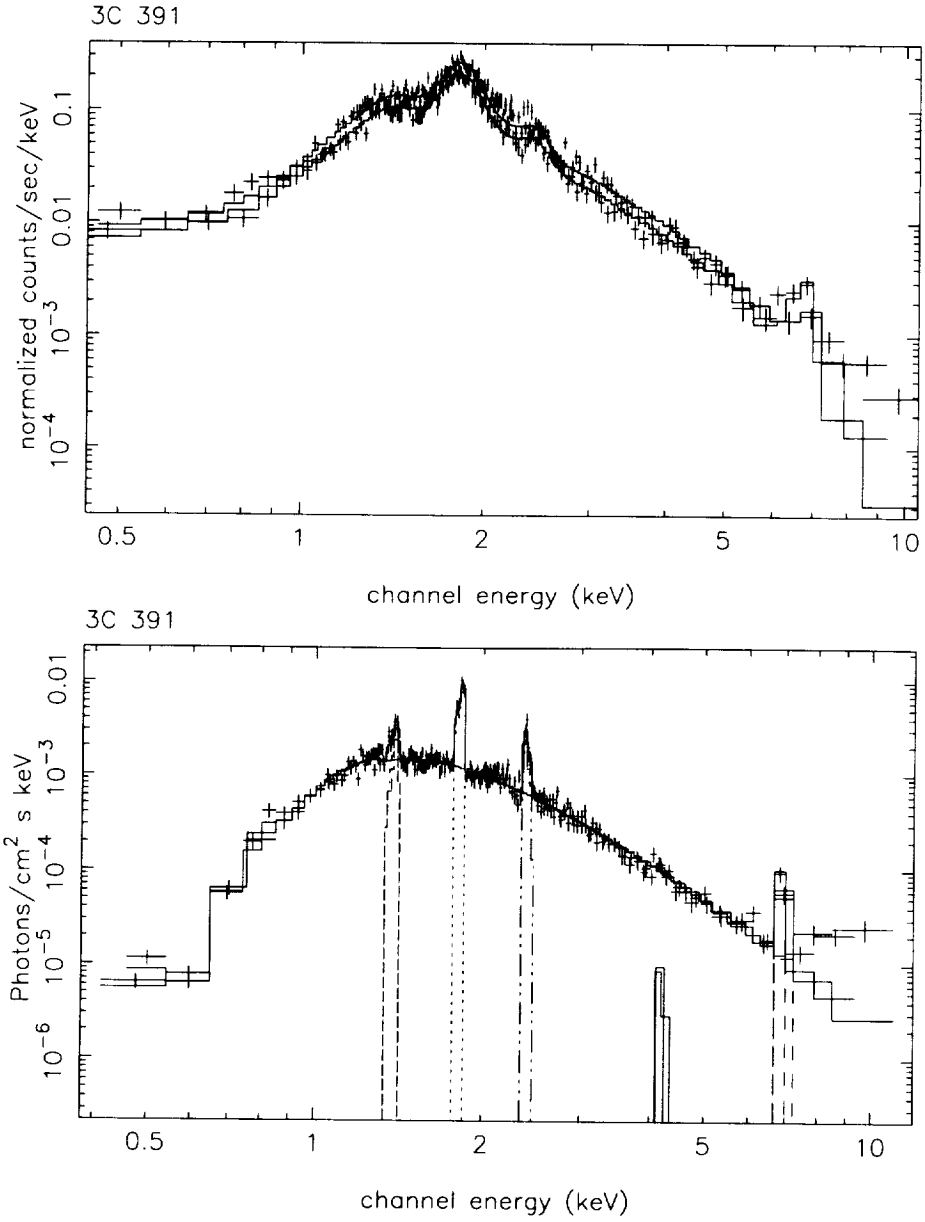

Figure 7.8: Folded (top) and unfolded (bottom) spectra of 3C 391 with the parameters in Tab. 7.16 used in the fit.

3C 396		
Model Component	Parameter	Value
Absorption	$N_{\rm H}$	3.6×10^{22} $\rm cm^{-2}$
Reynolds' Synchrotron Model	$S_{\rm 1GHz}$	18 Jy
	α	0.53
	max $\nu_{\rm roll\,off}$	1.4×10^{16} Hz
Thermal Bremsstrahlung	kT	0.13 keV
	Normalization	63
Narrow Gaussian	$F_{\rm line}$	7×10^{-4} $\rm ph.cm^{-2}s^{-1}$
	Line Energy	1.8 keV
Narrow Gaussian	$F_{\rm line}$	2×10^{-4} $\rm ph.cm^{-2}s^{-1}$
	Line Energy	2.4 keV
Narrow Gaussian	$F_{\rm line}$	2×10^{-5} $\rm ph.cm^{-2}s^{-1}$
	Line Energy	6.6 keV
Very Hard Power-Law	1 keV flux density	8×10^{-5} $\rm ph.cm^{-2}s^{-1}keV^{-1}$
	Photon Index	0.53

Table 7.18: The best-fit spectrum of 3C 396, assuming that synchrotron radiation is the primary source of X-ray continuum emission. This fit had $\chi^2 = 168$ for 144 degrees of freedom (χ^2_ν=1.2). The radio flux was taken from Green's catalogue, and the radio spectral index from Anderson & Rudnick (1993); both radio parameters were frozen during the X-ray fitting. The spectrum is shown on page 116.

$\alpha \downarrow$ $S_{\rm 1GHz} \rightarrow$	16	17	18	19	20
0.43	0.75	0.74	0.73	0.72	0.71
0.48	1.1	1.1	1.0	1.0	1.1
0.53	1.8	1.7	**1.6**	1.6	1.6
0.58	2.7	2.6	2.5	2.5	2.6
0.63	4.8	4.6	4.4	4.3	4.1

Table 7.19: The best-fit roll-off frequency of 3C 396 ($\times 10^{16}$ Hz) as a function of radio flux density (Jy) and spectral index.

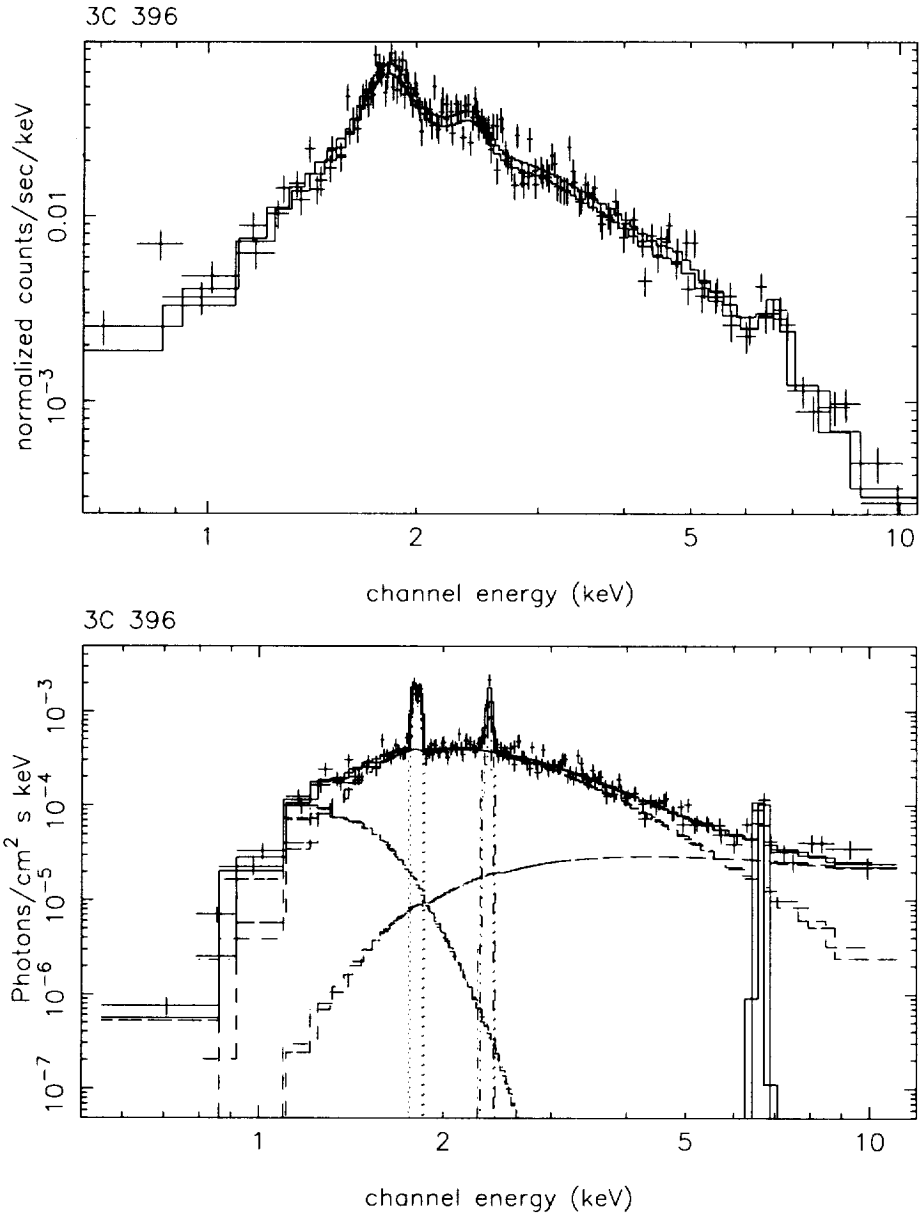

Figure 7.9: Folded (top) and unfolded (bottom) spectra of 3C 396 with the parameters in Tab. 7.18 used in the fit.

Kes 73		
Model Component	Parameter	Value
Absorption	$N_{\rm H}$	1.6×10^{22} cm^{-2}
Reynolds' Synchrotron Model	$S_{\rm 1GHz}$	6 Jy
	α	0.68
	max $\nu_{\rm roll\,off}$	1.5×10^{18} Hz
Thermal Bremsstrahlung	kT	0.9 keV
	Normalization	0.1
Narrow Gaussian	$F_{\rm line}$	3.3×10^{-3} ph.cm^{-2}s^{-1}
	Line Energy	1.3 keV
Narrow Gaussian	$F_{\rm line}$	3.0×10^{-3} ph.cm^{-2}s^{-1}
	Line Energy	1.8 keV
Narrow Gaussian	$F_{\rm line}$	1.2×10^{-3} ph.cm^{-2}s^{-1}
	Line Energy	2.4 keV
Narrow Gaussian	$F_{\rm line}$	1.1×10^{-4} ph.cm^{-2}s^{-1}
	Line Energy	3.0 keV
Narrow Gaussian	$F_{\rm line}$	1×10^{-5} ph.cm^{-2}s^{-1}
	Line Energy	7 keV

Table 7.20: The best-fit spectrum of Kes 73, assuming that synchrotron radiation is the primary source of X-ray continuum emission. This fit had $\chi^2 = 353$ for 246 degrees of freedom (χ^2_ν=1.4). The radio flux and spectral index were taken from Green's catalogue, and frozen during the X-ray fitting. The spectrum is shown on page 118. It should be noted that the very high roll-off frequency is most-likely not physical, but instead represents the central compact source (see page 7.3.10.

$\alpha \downarrow$ $S_{\rm 1GHz} \rightarrow$	4	5	6	7	8
0.58	19	16	14	12	11
0.63	58	44	36	31	27
0.68	360	220	**150**	120	97
0.73	big	big	1000	1000	990
0.78	big	big	big	big	big

Table 7.21: The best-fit roll-off frequency of Kes 73 ($\times 10^{16}$ Hz) as a function of radio flux density (Jy) and spectral index. Where a roll-off frequency of "big" is indicated, the X-ray emission exceeds the extrapolated radio emission.

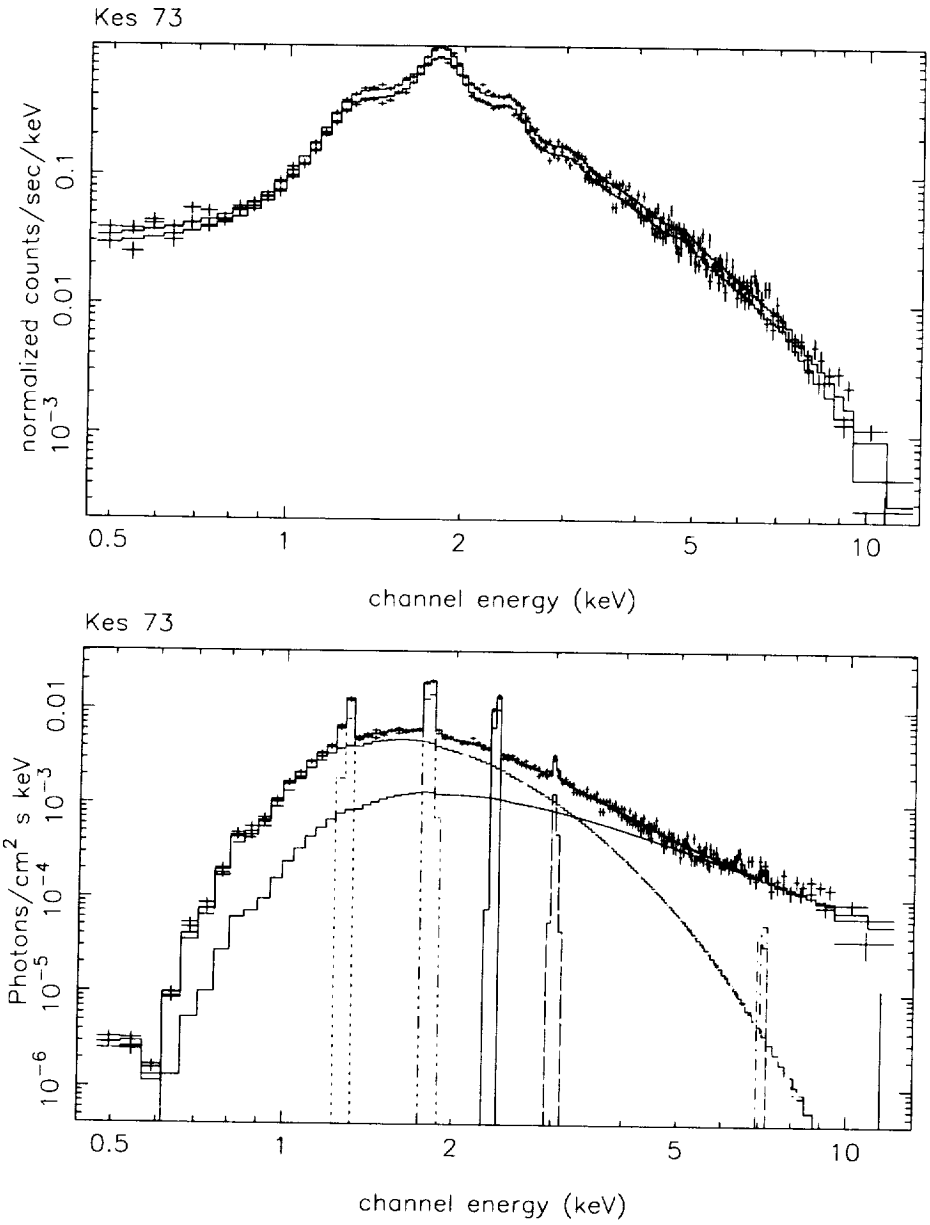

Figure 7.10: Folded (top) and unfolded (bottom) spectra of Kes 73 with the parameters in Tab. 7.20 used in the fit.

RCW 103		
Model Component	Parameter	Value
Absorption	$N_{\rm H}$	5.6×10^{21} $\rm cm^{-2}$
Reynolds' Synchrotron Model	$S_{\rm 1GHz}$	28 Jy
	α	0.6
	max $\nu_{\rm roll\,off}$	1.2×10^{16} Hz
Thermal Bremsstrahlung	kT	0.2 keV
	Normalization	24
Narrow Gaussian	$F_{\rm line}$	9.4×10^{-2} $\rm ph.cm^{-2}s^{-1}$
	Line Energy	0.8 keV
Narrow Gaussian	$F_{\rm line}$	3.9×10^{-3} $\rm ph.cm^{-2}s^{-1}$
	Line Energy	1.8 keV
Narrow Gaussian	$F_{\rm line}$	1.0×10^{-3} $\rm ph.cm^{-2}s^{-1}$
	Line Energy	2.3 keV
Narrow Gaussian	$F_{\rm line}$	9.2×10^{-5} $\rm ph.cm^{-2}s^{-1}$
	Line Energy	2.9 keV
Narrow Gaussian	$F_{\rm line}$	2.1×10^{-5} $\rm ph.cm^{-2}s^{-1}$
	Line Energy	6.6 keV

Table 7.22: The best-fit spectrum of RCW 103, assuming that synchrotron radiation is the primary source of X-ray continuum emission. This fit had $\chi^2 = 1942$ for 179 degrees of freedom (χ^2_ν=11).. The radio flux and spectral index were taken from Green's catalogue, and frozen during the X-ray fitting. The spectrum is shown on page 118. It should be noted that the poor fit is a result of the central compact source (see page 7.3.10.

$\alpha \downarrow$ $S_{\rm 1GHz} \rightarrow$	26	27	28	29	30
0.40	0.60	0.59	0.59	0.58	0.58
0.45	0.84	0.83	0.82	0.81	0.79
0.50	1.23	1.21	**1.20**	1.18	1.17
0.55	1.88	1.85	1.82	1.77	1.74
0.60	2.94	3.02	2.98	2.91	2.86

Table 7.23: The best-fit roll-off frequency of RCW 103 ($\times 10^{16}$ Hz) as a function of radio flux density (Jy) and spectral index. Where a roll-off frequency of "big" is indicated, the X-ray emission exceeds the extrapolated radio emission.

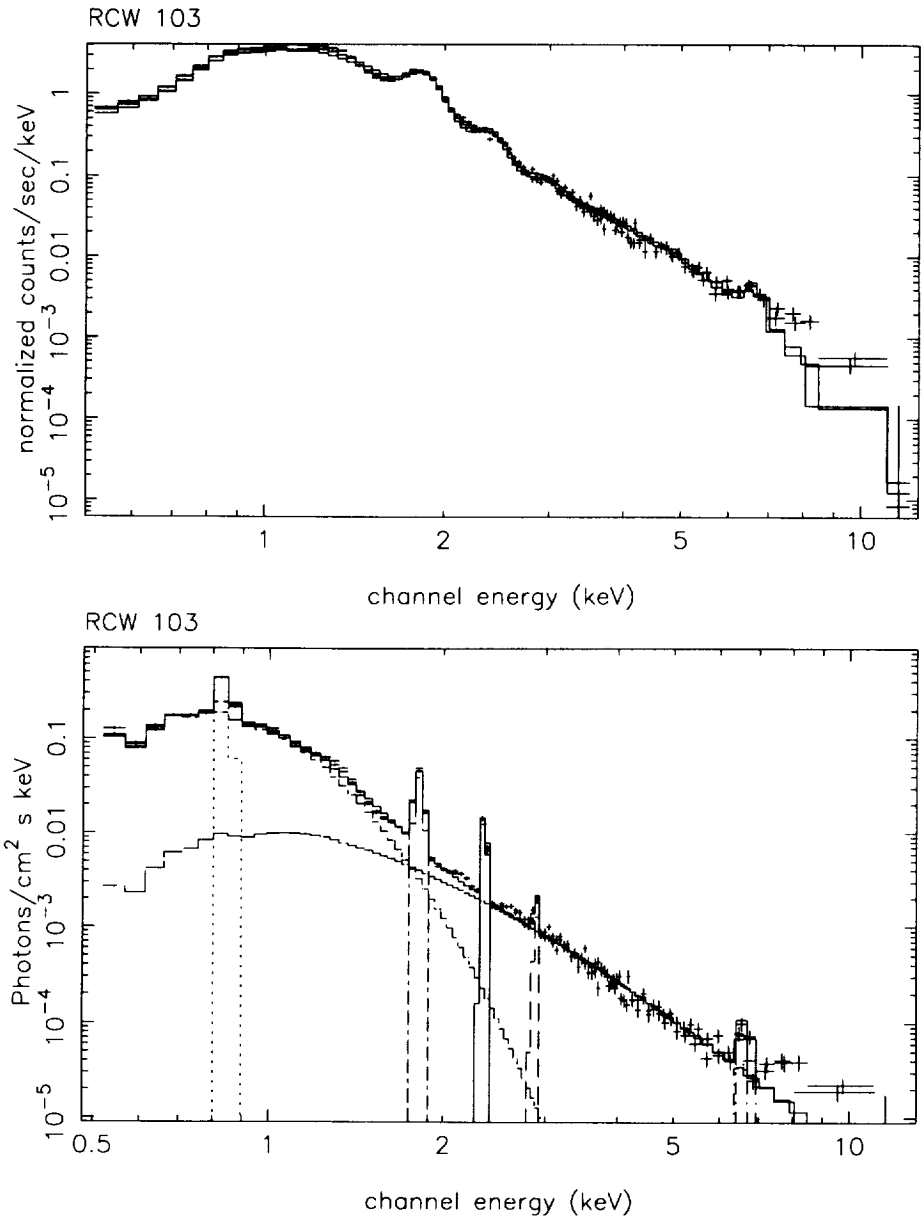

Figure 7.11: Folded (top) and unfolded (bottom) spectra of RCW 103 with the parameters in Tab. 7.22 used in the fit.

G346.6-0.2		
Model Component	Parameter	Value
Absorption	$N_{\rm H}$	4.9×10^{22} cm^{-2}
Reynolds' Synchrotron Model	$S_{\rm 1GHz}$	10 Jy
	α	0.50
	max $\nu_{\rm roll\,off}$	1.5×10^{16} Hz

Table 7.24: The best-fit spectrum of G346.6-0.2, assuming that synchrotron radiation is the primary source of X-ray continuum emission. This fit had $\chi^2 = 43$ for 43 degrees of freedom (χ^2_ν=1.0). The radio flux and spectral index were taken from Green's catalogue, and frozen during the X-ray fitting. The spectrum is shown on page 122.

$\alpha \downarrow$ $S_{\rm 1GHz} \rightarrow$	8	9	10	11	12
0.40	0.8	0.7	0.7	0.7	0.7
0.45	1.1	1.0	1.0	1.0	0.9
0.50	1.6	1.5	**1.5**	1.4	1.4
0.55	2.5	2.4	2.3	2.2	2.1
0.60	4.4	4.1	3.9	3.7	3.5

Table 7.25: The best-fit roll-off frequency of G346.6-0.2 ($\times 10^{16}$ Hz) as a function of radio flux density (Jy) and spectral index.

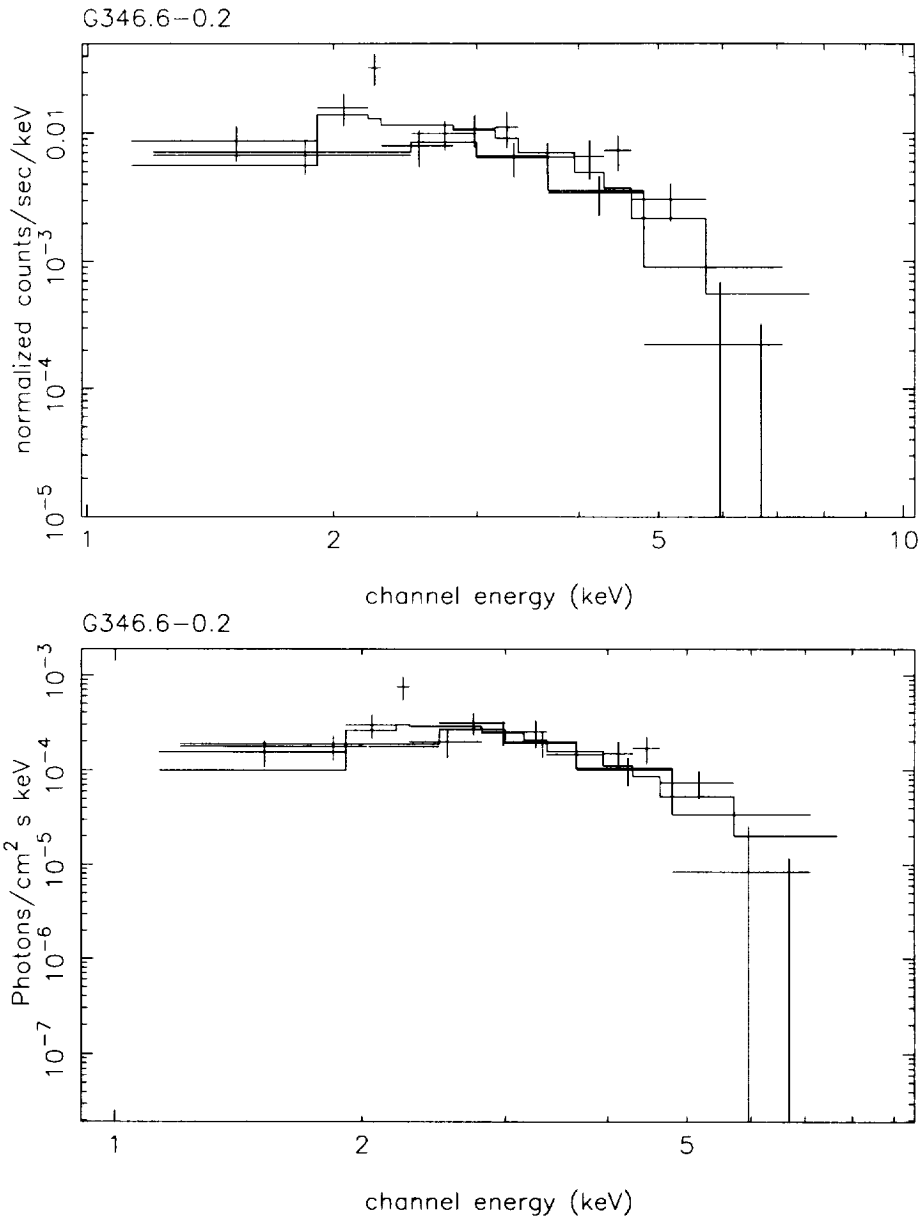

Figure 7.12: Folded (top) and unfolded (bottom) spectra of G346.6-0.2 with the parameters in Tab. 7.24 used in the fit.

G352.7-0.1		
Model Component	Parameter	Value
Absorption	$N_{\rm H}$	2.2×10^{22} cm^{-2}
Reynolds' Synchrotron Model	$S_{\rm 1GHz}$	4 Jy
	α	0.60
	max $\nu_{\rm roll\,off}$	6.6×10^{16} Hz
Narrow Gaussian	$F_{\rm line}$	2.8×10^{-4} ph.cm^{-2}s^{-1}
	Line Energy	1.8 keV
Narrow Gaussian	$F_{\rm line}$	3.4×10^{-5} ph.cm^{-2}s^{-1}
	Line Energy	2.5 keV

Table 7.26: The best-fit spectrum of G352.7-0.1, assuming that synchrotron radiation is the primary source of X-ray continuum emission. This fit had $\chi^2 = 98$ for 37 degrees of freedom (χ^2_ν=2.6). The radio flux and spectral index were taken from Green's catalogue, and frozen during the X-ray fitting. The spectrum is shown on page 124.

$\alpha \downarrow S_{\rm 1GHz} \rightarrow$	2	3	4	5	6
0.50	2.9	2.3	2.0	1.9	1.7
0.55	5.3	4.1	3.5	3.1	2.7
0.60	11	8.2	**6.6**	5.7	5.1
0.65	33	21	15	12	10
0.70	177	81	51	35	28

Table 7.27: The best-fit roll-off frequency of G352.7-0.1 ($\times 10^{16}$ Hz) as a function of radio flux density (Jy) and spectral index.

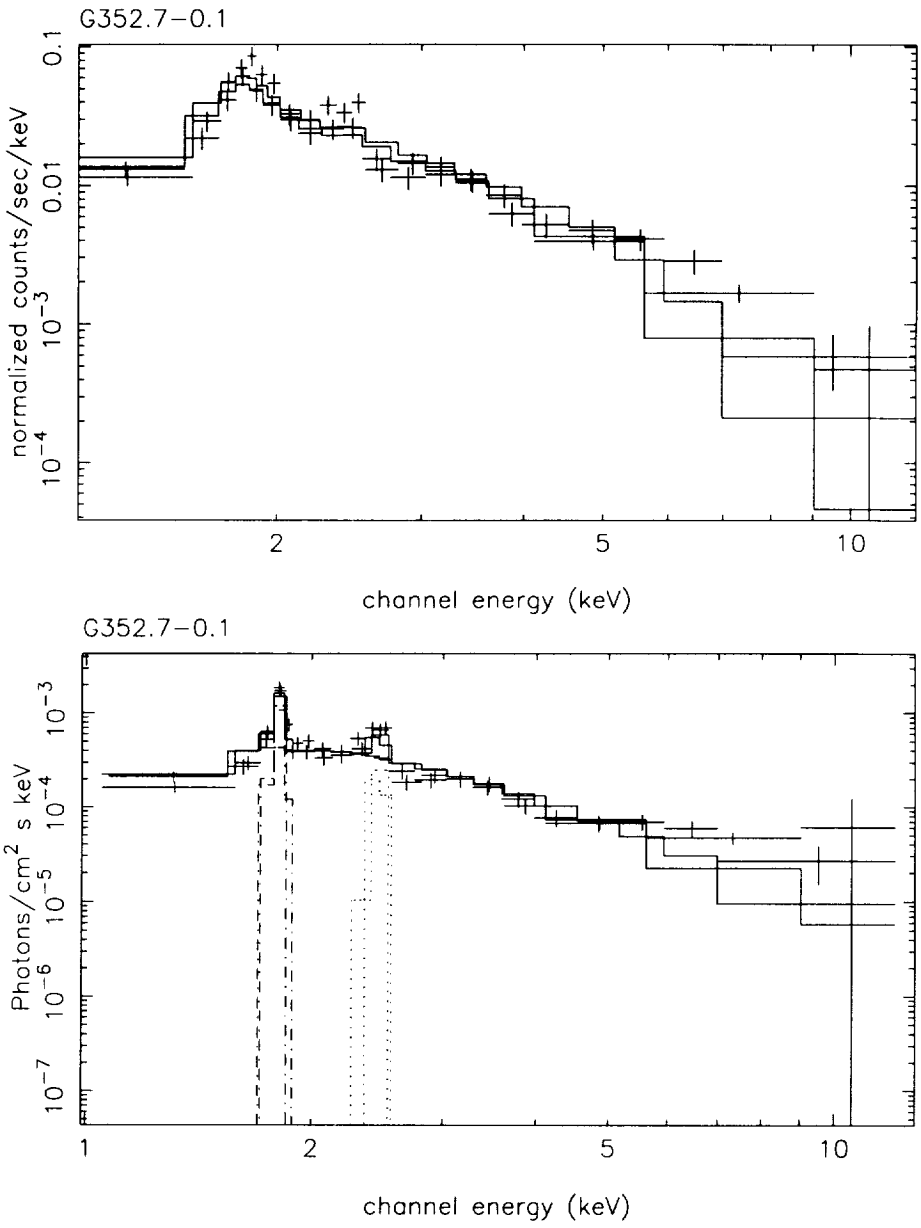

Figure 7.13: Folded (top) and unfolded (bottom) spectra of G352.7-0.1 with the parameters in Tab. 7.26 used in the fit.

Object	$\nu_{roll\,off}$ (10^{16} Hz)	(keV)	$E_{max}\sqrt{(B/10\mu G)}$ (erg)	(TeV)	χ^2_ν	Page Numbers
Kes 73[a]	150	6	290	200	1.4	93, 117–118
Cas A[b]	32	1	130	80	[c]	90, 97–98
Kepler	11	0.5	79	50	3.1	91, 104–105
Tycho	8.8	0.4	70	40	2.6	92, 110–112
G352.7-0.1	6.6	0.3	60	40	2.6	94, 123–124
SN 1006[bd]	6	0.2	57	40	–	72
3C 397	3.4	0.1	43	30	1.8	91, 106–107
W49 B	2.4	0.1	36	20	1.2	91, 101–103
G349.7+0.2	1.8	0.07	31	20	1.1	90, 99–100
3C 396	1.6	0.07	30	20	1.2	93, 115–116
G346.6-0.2	1.5	0.06	29	20	1.0	94, 121–122
3C 391	1.4	0.06	28	20	1.3	93, 113–114
SN 386[a]	1.2	0.05	26	20	1.3	92, 108–109
RCW 103[a]	1.2	0.05	26	20	11	93, 119–120

[a]Contains a known hard X-ray central source.

[b]Synchrotron radiation is currently the leading explanation for the fitted X-ray continuum.

[c]The RXTE reduced χ^2 value for Cas A is misleading, because systematic errors dominate.

[d]Reynolds (1996) completed an analysis of SN 1006, which includes this measurement. We include SN 1006 here for completeness. It should also be noted that Reynolds (1996) derived a magnetic field of 0.6μG, implying that $E_{max} \sim$ 100–200 TeV.

Table 7.28: Roll-off frequency and maximum electron energy upper limits. These are upper limits, because in each case the bulk of the continuum is assumed to be synchrotron. Values shown in cgs units were rounded to two digits, while their common unit equivalent were rounded to the more reasonable one significant figure. Note that while 10 μG is the canonical SNR magnetic field, Cas A's magnetic field is about 1 mG (i.e. $E_{max} \sim 8$ TeV) and others are quite uncertain.

Chapter 8

A Possible Site of Cosmic Ray Acceleration in the Supernova Remnant IC 443

Published in The Astrophysical Journal as

Keohane, J.W., Gotthelf, E.V., Petre, R, Ozaki, M. & Koyama, K.

Vol. 466, pp. 309-316, July 20, 1997

We present evidence for shock acceleration of cosmic rays to high energies ($\sim$10 TeV) in the supernova remnant IC 443. X-ray imaging spectroscopy with ASCA reveals two regions of particularly hard emission: an unresolved source embedded in an extended emission region, and a ridge of emission coincident with the southeastern rim. Both features are located on part of the radio shell where the shock wave is interacting with molecular gas, and together they account for a majority of the emission at 7 keV. Though we would not have noticed it *a priori*, the unresolved feature is coincident with one resolved by the ROSAT HRI. Because this feature overlaps a unique

region of flat radio spectral index ($\alpha < 0.24$), has about equal light-crossing and synchrotron loss times, and a power law spectrum with a spectral index of α=1.3±0.2, we conclude that the hard X-ray feature is synchrotron radiation from a site of enhanced particle acceleration. Evidence against a plerion includes a lack of observed periodicity (the pulsed fraction upper limit is 33%), the spectral similarity with the more extended hard region, the location of the source outside the 95% error circle of the nearby EGRET source, the fact that it is nestled in a bend in the molecular cloud ring with which IC 443 is interacting, and the requirement of an extremely high transverse velocity (≥5,000 km/s). We conclude that the anomalous feature is most likely tracing enhanced particle acceleration by shocks that are formed as the supernova blast wave impacts the ring of molecular clouds.

Subject headings: acceleration of particles — radiation mechanisms: non-thermal — shock waves — cosmic rays — supernova remnants — supernovae: individual (IC 443)

8.1 Introduction

It is generally accepted from energy budget considerations that supernova remnants (SNRs) are the primary source of galactic cosmic rays (CRs), which are inferred to span the energy range from about 10^8 to 10^{14} eV (Blandford & Ostriker 1978; Axford 1994; Biermann 1995, and references therein). Though radio observations of synchrotron radiation from supernova remnants supply bountiful evidence that they are the source of CRs at GeV energies, evidence regarding higher energy cosmic rays is largely circumstantial. A search for ultra-high energy γ-rays ($\sim 10^{14}$ eV) coincident with SNRs detected nothing significant (Allen et al. 1995). The best evidence thus far for shock acceleration of ~100 TeV CRs, comes from X-ray observations of SN 1006 (Koyama et al. 1995). SN 1006 appears to be unique in that the non-thermal X-ray flux from its shell dominates the thermal, but current limits on the non-thermal flux from the

shells of other young SNR do not exclude the presence of a synchrotron component, and hence ongoing CR acceleration to TeV energies.

In this paper we report the discovery of a site in another SNR in which high energy cosmic rays are possibly being accelerated, but by a different mechanism from that in SN 1006. Using ASCA GIS data, we have found a concentration of hard X-ray emission along the southern rim of the middle-aged remnant IC 443, whose spectrum is consistent with a power law, and whose morphology suggests enhanced shock acceleration resulting from the SNR shock encountering dense clouds in the ISM. The observations are consistent with the prediction of such an effect by (Jones & Kang 1993, hereafter JK93).

IC 443 (G189.1+3.0) is a nearby ($\approx$ 1.5 kpc) supernova remnant (SNR) of intermediate age. Many infrared and radio line observations have demonstrated that IC 443 is interacting with a ring of molecular clouds (e.g., DeNoyer 1979; Burton *et al.* 1988, hereafter BGBW; Burton *et al.* 1990; Dickman *et al.* 1992, hereafter DSZH; van Dishoeck *et al.* 1993). The region in which the most complex interactions between the molecular cloud and the SNR shock is occurring also has an unusually flat radio spectral index for a shell-like SNR (α <0.24 — Green 1986, hereafter G86).

In the X-ray band, IC 443 has been the subject of a number of comprehensive studies, most notably those of (Petre et al. 1988, hereafter PSSW) and (Asaoka & Aschenbach 1994, hereafter AA94)). It has an irregular soft X-ray morphology, influenced strongly by its interactions with an H I cloud to the northeast and the foreground molecular cloud and shadowing by the foreground SNR G189.6+3.3. Using Ginga, (Wang et al. 1992, hereafter WAHK) resolved spectrally a hard component which they were able to characterize by either a thermal model with kT$\sim$14 keV or a power law with photon index $\Gamma \sim 2.2$. Scanning observations by HEAO1 A-2 showed that the hard emission is more centrally located than the bright soft emission. Neither the A-2 nor the Ginga observations provided information regarding the extent of the hard emission.

Table 8.1: ASCA observations of the SNR IC 443

Sequence #	10011010	51023000
Mission Phase	PV phase	AO-1
RA (J2000)	$06^h17^m25^s$	$06^h16^m19^s$
Declination	$+22°40'37''$	$+22°26'53''$
GIS Exposure	20.2 ks	34.7 ks
Date	April 14, 1993	March 9, 1994

IC 443 is also coincident with a high energy γ-ray source, which has led to speculation that the γ-rays are produced by the interaction of cosmic rays, accelerated by IC 443's shocks, with nearby molecular cloud material (Sturner & Dermer 1995; Esposito et al. 1996, hereafter EHKS). Models of broad-band non-thermal spectra have recently been produced by Sturner et al. (1997); in these synchrotron radiation dominates from the radio to the soft X-ray, while electron bremsstrahlung and π^0 decay dominate the γ-ray emission for a supernova remnant like IC 443.

Our paper is organized as follows. We first present the ASCA GIS images showing the location of the hard X-ray emission region (§8.2.1). We compare the ASCA image with that from the ROSAT HRI. We then discuss our analysis of the GIS spectrum and the GIS and HRI light curves from that region (§8.2.4). Finally, we discuss possible emission mechanisms and the implications for the acceleration of cosmic rays by supernova remnants (§8.3.2).

8.2 Observations and Analysis

8.2.1 The ASCA GIS X-ray Maps

ASCA performed observations of two adjacent regions of IC 443, one during the Performance Verification (PV) phase of of the mission, the other during the first cycle of guest observations (AO-1). The relevant information about these observations is

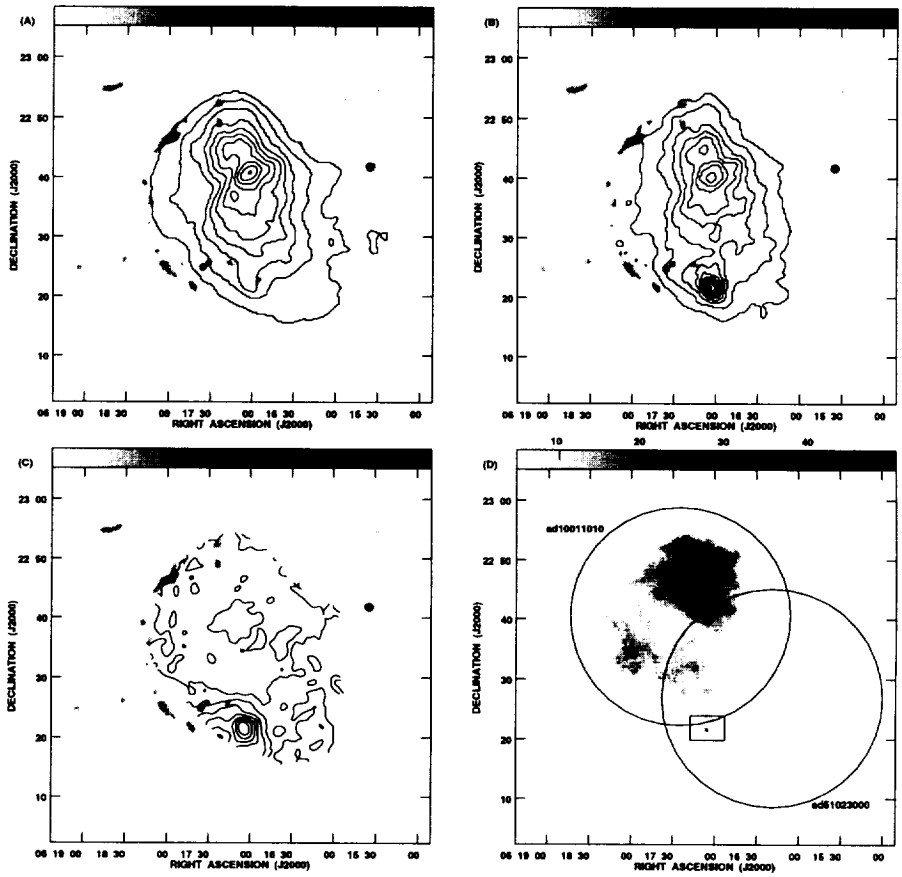

Figure 8.1: Soft (A) and hard (B) GIS contour images of IC 443. The energy bands are 1.1–2.1 and 2.1–12.0 keV respectively. The ratio of the two bands (C) is also shown (blanked in regions of low soft X-ray surface brightness). The contour levels in each figure are multiples of 10% of the peak. For reference, we have shown in grey-scale (A, B, C), a 1.4 GHz radio map from the VLA sky survey (10–100 mJy/beam). Image D shows our ROSAT HRI mosaic of IC 443; the GIS field of view for each observation and the region shown in Figure 8.2.1 are overlaid.

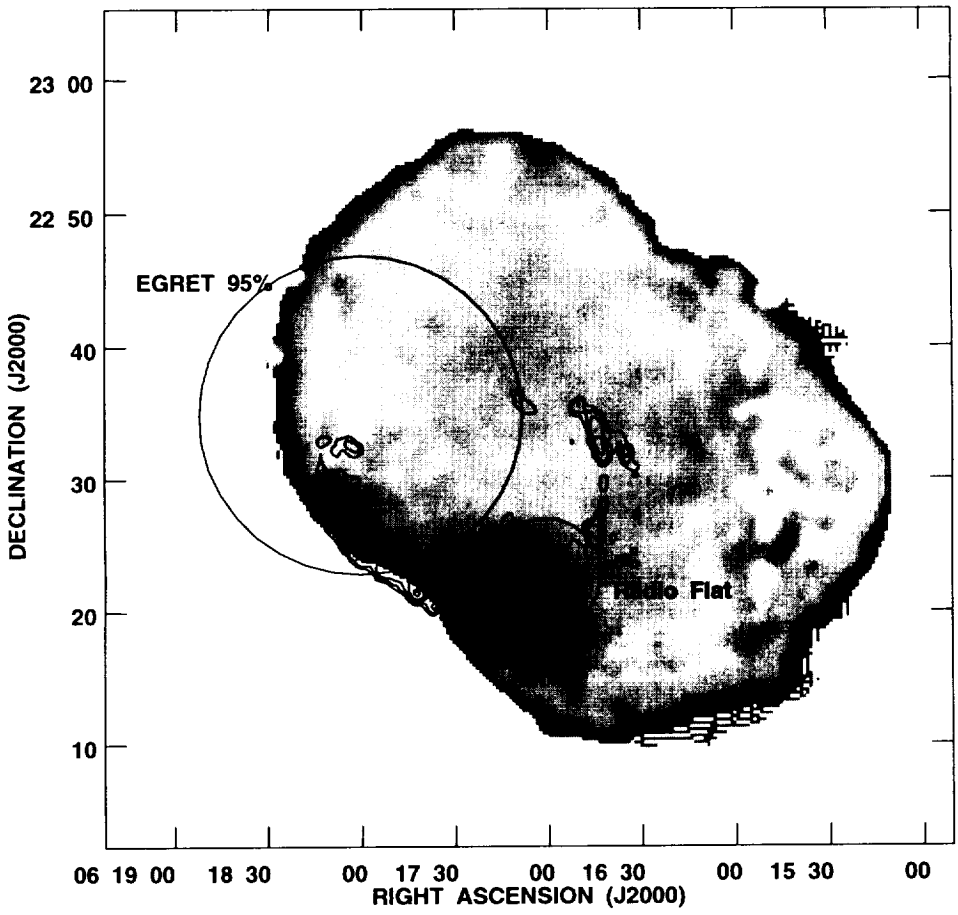

Figure 8.2: The ASCA GIS hardness ratio map ($F_{2.1\text{-}12\ \mathrm{keV}}/F_{1.1\text{-}2.1\ \mathrm{keV}}$) is shown in grey-scale. The overlaid drawings are: the EGRET γ-ray detection circle (EHKS), the region of flat radio spectral index (G86) and a contour plot of the v=1-0S(1) H_2 emission line intensity (BGBW).

contained in Table 8.1. We extracted these data sets from the ASCA public archive. In figures 8.2 A and B, we show exposure-corrected GIS mosaic images for the hard (2.1–12 keV) and soft bands (1.1–2.1 keV). These appear highly correlated, except for a bright feature in the hard band map, centered at RA = $06^h17^m05^s$, Dec = $+22°21'30''$ (J2000). The anomalous nature of this feature is shown in dramatic fashion in figure 8.2C, a spectral hardness ratio map, constructed by dividing the hard band map by the soft. There it can be seen that the other features, associated with the diffuse thermal emission in IC 443, all have similar spectral hardness, but the hard X-ray feature (HXF) stands out. The ASCA GIS brightness distribution within the hard feature is consistent with that expected from a source smaller than $\sim 1'$. The hard feature is $\sim 12'$ off axis so it was not in the SIS field of view.

In addition, there is a ridge of spectral hardness located northeast of the HXF along the radio-bright rim of the remnant. This second feature is not shown in Fig. 8.2C because it was blanked due to its small soft X-ray count rate. It is shown, however, in Figs. 8.2 and 8.2.1. As will be discussed in more detail in §8.2.4, the hard flux from the observed portion of the ridge is about half the hard flux from the HXF and the two regions can account for a majority of the total hard ASCA flux.

8.2.2 ROSAT HRI Image

The region containing the HXF was observed for 30 ks using the ROSAT HRI as part of a program to create a complete high resolution X-ray image of IC 443. In Fig. 8.2D, we show the complete HRI mosaic, with the GIS fields of view overlaid. A surface brightness enhancement appears approximately at the location of the HXF. The HRI map of the region containing the HXF is shown in Fig. 8.2.1, with the GIS hardness ratio contours overlaid. The feature's central core has an angular extent of about $10''\times 5''$, with extended lower level structure of about $1'$ in extent. The elongation of the central core is perpendicular to the orientation of the low level emission and does not resemble

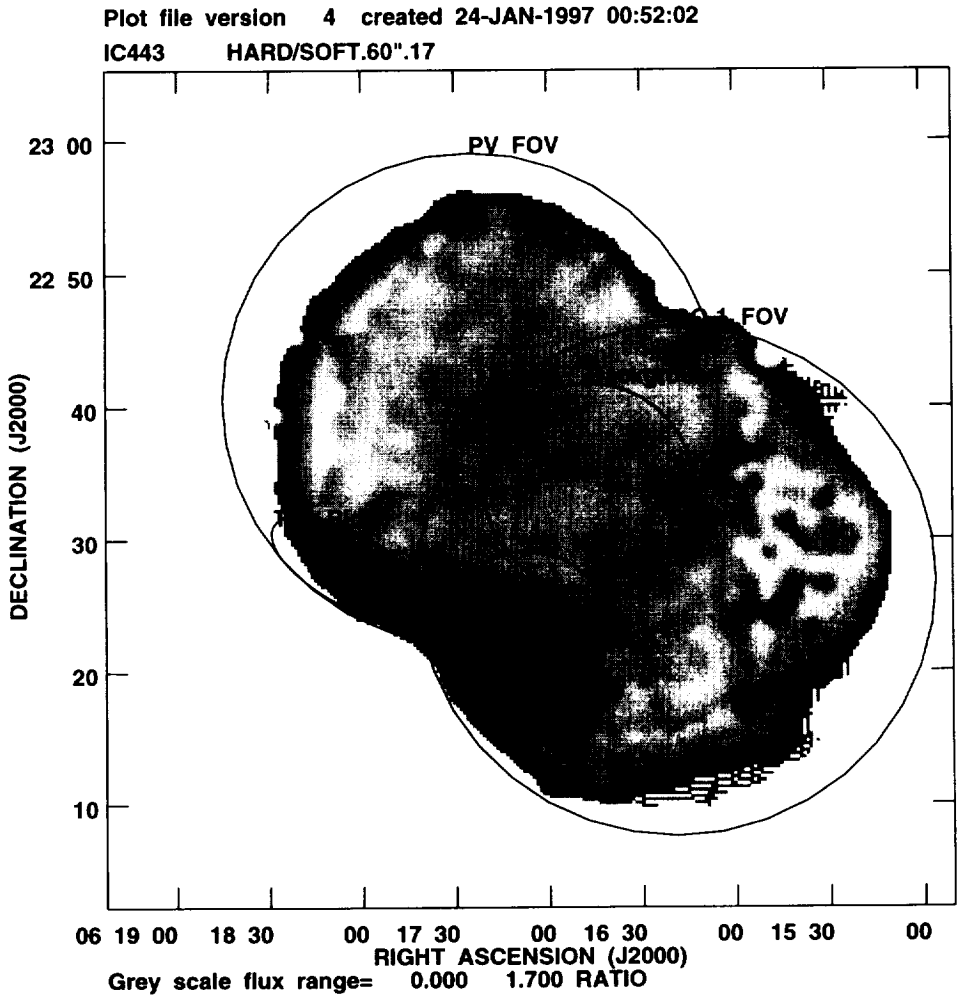

Figure 8.3: The regions where ASCA GIS data were selected for our spectral analysis and the approximate ASCA GIS fields of view, overlaid on the same hardness ratio map as shown in Fig. 8.2. We purposely chose a larger than needed region about the HXF and the ridge in order to spectrally distinguish between the thermal and non-thermal spectra.

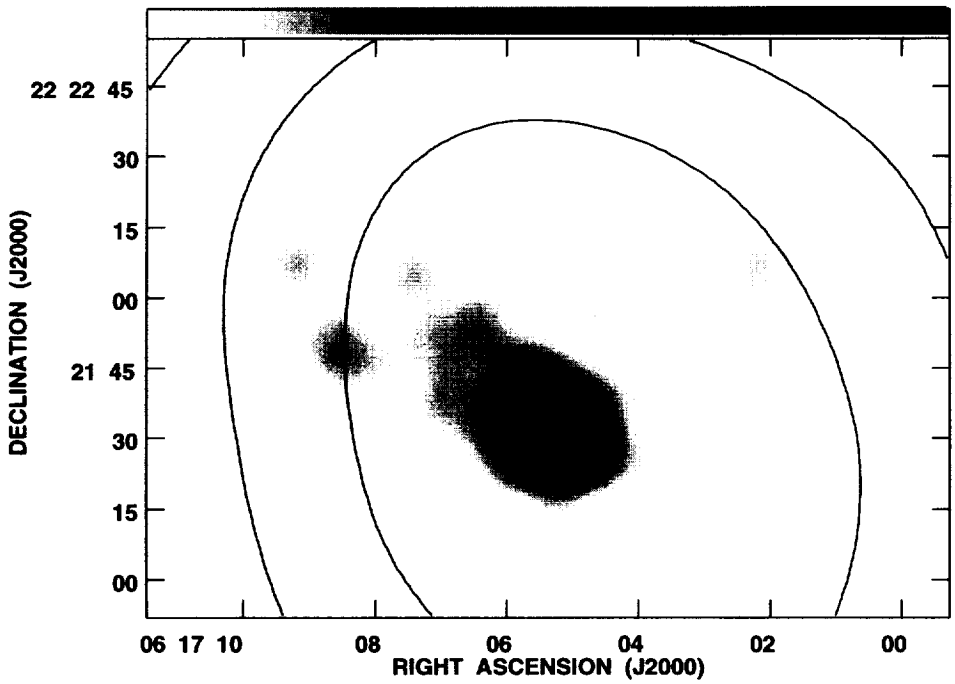

Figure 8.4: The 10″ FWHM Gaussian smoothed ROSAT HRI (grey-scale) and the 60″ resolution hardness ASCA hardness ratio map shown with the same contour levels as figure 8.2C. The grey-scale range is 10-45 counts per 10″ diameter circular "beam."

the HRI point spread function, so we believe it to be resolved.

8.2.3 Spatial Correlations with Other Bands

In Fig. 8.2 we overlay on the GIS spectral hardness ratio map possibly related spatial information from other bands: the EGRET 95 percent confidence error circle (EKHS), contours of H_2 emission (BGBW) which locate the sites of the most intense SNR shock/cloud interaction, and the region in which the $\lambda\lambda$20–200 cm spectral index is appreciably flatter than elsewhere in IC 443 (G86). The HXF is just outside a concave arc of H_2 emission, but correlates well with the region of flat radio index. Interestingly, it is well outside the EGRET error circle. In the Digitized Sky Survey (Lasker et al. 1990), there are some faint filaments in this region, but no obvious unresolved sources near the hard feature. A search of the most recent on-line pulsar catalog (Taylor, Manchester, & Lyne 1993) reveals none near the feature.

In addition to the main hard feature, the ridge of hard emission overlaps the H_2 emission region, but does not appear coincident with any region of radio spectral index flattening. However, it does lie along the bright radio rim.

8.2.4 The ASCA Spectrum

The HXF and the ridge are embedded within the diffuse emission of IC 443 — at least in projection. Thus in order to determine the spectral properties of these features, one must first adequately characterize the "background" thermal emission. We therefore extracted a spectrum from the adjacent larger region shown in figure 8.2.1. We assume, based on the smoothness of the spectral hardness ratio map, that the spectrum of the diffuse emission does not vary appreciably in the neighborhood of the HXF; based on the previous X-ray observations the spectral variations in the diffuse emission would be most significant below 1 keV, outside the effective GIS band. To this "background"

Table 8.2: Spectral Fits to Background Field and Hard X-ray Features

	Model	Data Sets	χ^2	χ^2_ν	$T_{\rm soft}$ keV	$N_{\rm H}$ $10^{22}{\rm cm}^{-2}$	Hard Component
1	S-T[a]	Background	781	0.71	0.89 ± 0.03	0.12 ± 0.03	N/A
2	S-T[a]	On HXF	793	0.73	1.9 ± 0.1	0	N/A
3	S-T[b]	On HXF	1407	1.28	0.89	0.31 ± 0.03	N/A
4	P-L[c] + S-T[b]	On HXF	769	0.70	0.89	0.18 ± 0.03	$\Gamma = 2.3 \pm 0.2$
5	P-L + S-T[d]	On HXF	766	0.70	$1.1^{+0.3}_{-0.1}$	0.12	$\Gamma = 2.4^{+0.2}_{-0.4}$
6	H-B + S-T[b]	On HXF	763	0.70	0.89	0.13 ± 0.03	kT=$3.9^{+1.7}_{-0.6}$ keV
7	S-T[d]	The Ridge	778	0.40	0.74 ± 0.08	0.12	N/A
8	P-L + S-T[b]	The Ridge	755	0.39	0.89	$0^{<0.03}$	$\Gamma = 0.1 \pm 1.3$
9	P-L + S-T[d]	The Ridge	748	0.38	$0.54^{+0.07}_{-0.16}$	0.12	$\Gamma = 1.6^{+1.4}_{-0.7}$

Fits are to the energy range 0.5–12 keV

S-T = Soft Thermal *ad hoc* model described in the text

P-L = Power Law

H-B = Hot thermal Bremsstrahlung

[a] Letting the scaling (GIS2 & GIS3), column density, temperature and line strengths vary

[b] We froze the line strengths and temperature to the off source (model #1) values, but fit the column density and scaling.

[c] The best-fit 5 keV flux density is $(7 \pm 3) \times 10^{-13} \frac{\rm erg}{\rm s\,cm^2\,keV}$.

[d] We froze the column density and line strengths to the off source (model #1) values, but fit the temperature and scaling.

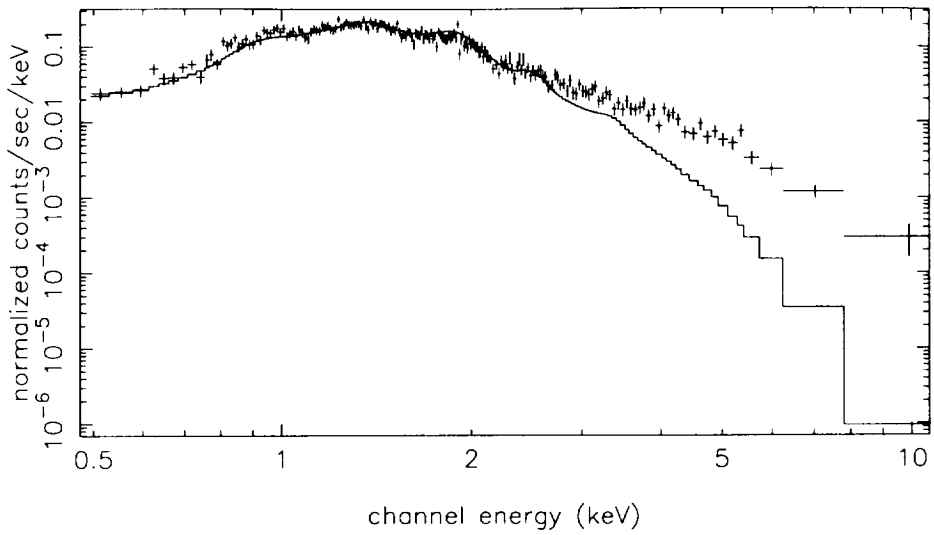

Figure 8.5: The ASCA GIS2 spectrum of the hard feature in IC 443 with the best-fit *ad hoc* thermal model. By adding a hard power law component to this model we reduce the combined GIS2 and GIS3 χ^2 by $\Delta\chi^2 = 640$.

spectrum we fit an *ad hoc* thermal emission model, comprised of a thermal bremsstrahlung continuum and narrow Gaussians to represent the most prominent emission lines (the Heα transitions of Ne, Mg, Si, S and Ar). Such *ad hoc* models have been used previously to model ASCA spectra from other remnants (e.g., Miyata et al. 1994; Holt et al. 1994). The best fit model yields kT$\sim$0.9 keV, comparable with published temperatures for IC 443 (PSSW, WAHK). However, it is important not to over-interpret our thermal results, because we have made no attempt to distinguish the Heα transitions from weaker nearby spectral lines (including each element's corresponding H-like Lyα transition) or to develop a physically self-consistent thermal model.

We next applied this same model to the GIS spectrum of the region containing the HXF (also shown in figure 8.2.1), allowing only the normalization to vary. As shown in table 8.2, this yields an unacceptable fit. As indicated in Fig. 8.2.4, the "background" model provides a good fit to the data below $\sim$2 keV, but there is a substantial flux excess

at higher energies. An acceptable fit to the "on HXF" spectrum is obtained by adding a second continuum component. The current data do not allow us to distinguish between a power law with Γ=2.3±0.2 and thermal bremsstrahlung with kT=$3.9^{+1.7}_{-0.6}$ keV.

We also performed this same analysis using a smaller on-source region, tightly drawn around the HXF. However, this was less effective: because of the lack of thermal background counts, it is harder to spectrally distinguish the background from the non-thermal source emission. Nevertheless we measure a photon index of Γ=$2.2^{+0.1}_{-0.4}$, using the technique described above.

We applied the same spectral analysis procedure as described above for the HXF to the hard ridge. Since the ridge is farther from the "background" region than the HXF (see Fig. 8.2.1) and we fit the thermal model using the AO-1 data, we were uncertain if it was appropriate to use the same background thermal model for both the HXF and the ridge. To test this, we performed our analysis using both the AO-1 "background" region shown in Fig. 8.2.1 and one using PV phase data closer to the ridge. We do not detect any significant difference in the spectral index or flux of the hard ridge region as a function of the chosen background region.

Because of its larger extent and lower surface brightness, the ridge spectrum has lower signal to noise than the HXF. As with the HXF, fitting the spectrum with the background model yielded a clear excess above 2 keV. It was not possible, however, to constrain the spectral properties of the ridge's hard component. While we have no evidence suggesting a different spectral form, we cannot eliminate the possibility that the hard emission from the ridge has a different origin.

The GIS spectral parameters for this region are similar to those obtained using the non-imaging (1°field of view) Ginga LAC. WAHK reported the presence of a hard component that was fit by a thermal model with kT=$11^{+7.5}_{-2.0}$ keV (from their Fig. 3) or a power-law with photon index $\Gamma = 2.2 \pm 0.13$. Assuming a uniform surface brightness inside the shell and an absorbing column density of $N_{\rm H} = 10^{21.9}\,{\rm cm}^{-2}$, WAHK found the

total 2–20 keV emitted flux from IC 443 to be 9×10^{-11} erg cm^{-2} s^{-1}. As the total flux is dominated by the $\sim$ 1 keV thermal component, a comparison between the broad band Ginga flux and the GIS flux from the hard features is inappropriate. A more reasonable quantity to compare is the flux density at 7 keV, where the relative contribution of the $\sim$ 1 keV component is negligible. Using Figure 2 in WAHK, and assuming that the Ginga LAC has an effective area of 3000 cm^2 and near unity quantum efficiency at 7 keV, we estimate the Ginga flux density at 7 keV to be 20×10^{-5} photons s^{-1} keV^{-1} cm^{-2}. From the GIS data, we find the HXF flux density at 7 keV to be approximately 4×10^{-5} photons s^{-1} keV^{-1} cm^{-2}, and the flux density of the portion of the hard ridge within the field of view to be about 2×10^{-5} photons s^{-1} keV^{-1} cm^{-2}. Thus the detected flux in the hard regions seems to account for only 30% of the hard flux detected by Ginga, despite their prominence in the GIS images. Moreover, integration over the rest of the surface of the remnant contained in the GIS fields (about 90 percent of the total) yields a flux density of no more than 4×10^{-5} photons s^{-1} keV^{-1} cm^{-2}, leaving a factor of two discrepancy between the GIS and Ginga 7 keV flux densities.

Two possible resolutions of this discrepancy are that there is significant hard flux from the small fraction of IC 443 unobserved by the GIS, or there is a calibration discrepancy between the GIS and Ginga. To check this latter possibility, we compare the broad band flux from all of IC 443 in the common 2-10 keV band. The 2-20 keV Ginga flux is 9×10^{-11} ergs cm^{-2} s^{-1} (WAHK). The 2-10 keV flux from IC 443 as measured by HEAO1 A-2 is $7 \pm 1 \times 10^{-11}$ ergs cm^{-2} s^{-1} (PSSW), consistent with the Ginga measurement. Integrating the 2-10 keV flux within the field of view of the two GIS pointings, we find $5 \pm 1 \times 10^{-11}$ ergs cm^{-2} s^{-1}; this represents 90 percent or more of the total flux from the remnant. The consistency of these numbers indicates that contribution of cross calibration uncertainties to the discrepancy is probably small, but could be as large as a factor of 2. Thus while it is possible that the GIS has observed all the regions in IC 443 producing hard flux, we cannot rule out the possibility that

the unobserved portion of the IC 443 rim to the south and east of the ridge contribute significantly to the hard flux.

A key conclusion about the spatial distribution of the hard X-ray emission in IC 443, independent of a resolution of this discrepancy, is that the hard emission is highly localized. The flux density from the bulk of the remnant surface area is at most 40 percent of the total hard flux. This provides a strict upper limit on the luminosity of a hard thermal component, distributed throughout the remnant. WAHK inferred that IC 443 is a very young (1200 y) remnant based on their interpretation of the hard component as hot gas arising from a high velocity shock, and IC 443's coincidence with the guest star of 837 A.D. Despite the restrictive limit we have placed on the flux of a hot thermal component, we nevertheless cannot rule out their conclusion about the age of IC 443. Moreover, high shock velocities may also be required to accelerate electrons to the relativistic energies required for the emission of X-ray synchrotron radiation, and WAHK's historical evidence is naturally unaffected by our observations.

8.2.5 Pulsation Search

In order to search for periodicity from the unresolved HXF, we performed coherent fast Fourier transforms (FFTs) on the ROSAT HRI and ASCA events recorded from the region used for spectral analysis (after applying the standard barycenter corrections). All our results are consistent with a non-periodic signal.

The temporal resolution of the GIS is 0.0625 s, so we cannot use the GIS data to search for a frequency faster than 8 Hz. On the other hand, the ROSAT HRI data have millisecond resolution. We therefore performed summed FFTs on the combined data set (ROSAT + ASCA) in the low frequency range 0.05–8 Hz, and only the ROSAT data in the high frequency range 10–1000 Hz. We find 99% confidence pulsed fraction upper limits of $\sim$15% and $\sim$33% in the low and high frequency ranges respectively.

8.3 Discussion

8.3.1 Summary of Results

We have discovered an isolated hard X-ray emitting feature and a ridge of hard emission in the southeast of the SNR IC 443 using the ASCA GIS. The HXF's X-ray spectrum can be characterized by either a power law of energy spectral index α=1.3±0.2 or thermal bremsstrahlung with kT=$3.9^{+1.7}_{-0.6}$ keV; the ridge spectrum appears similar. The features can account for most of the hard X-ray flux from IC 443 (§8.2.4). The core of the HXF is marginally resolved with the ROSAT HRI, but the low level surrounding emission extends about 10′ along the radio-bright shell. (§8.2.2, fig. 8.2.1). It is spatially coincident with the $\lambda\lambda$20–200 cm flat spectral ($\alpha \approx 0.2$) region (G86; fig. 8.2), and in the general region of, but not uniquely coincident with, regions of cloud/shock interactions (DeNoyer, 1979; fig. 8.2). It is located outside the 95 percent confidence error circle of the nearby EGRET source (EHKS; fig. 8.2). No strong periodicity is observed from the feature, with a pulse fraction upper limit of 33% (§8.2.5), and there is no known pulsar near it.

8.3.2 Origin of the Emission

We focus here on the origin of the emission from the HXF. Because of the uncertainty of the spectral parameters we know substantially less about the ridge. While some of our discussion below applies to all the emission (e.g. our conclusion that it is non-thermal), a more definitive understanding of the nature of the ridge emission (which could be different from that of the HXF) awaits a better quality X-ray spectrum.

The data suggest that the most likely mechanism for producing hard X-rays is synchrotron emission. Before addressing whether this emission arises from a plerion or shock accelerated electrons, we first discuss our rationale for ruling out alternative mechanisms, including bremsstrahlung from a thermal and a non-thermal population

of electrons, and inverse-Compton scattering.

Thermal Bremsstrahlung A thermal bremsstrahlung model provides an adequate fit to the ASCA and the Ginga spectra separately. The inferred temperatures are discrepant, however ($\approx$ 15 keV for Ginga versus $\approx$ 4 keV for ASCA). In contrast, a power law model yields the same photon index. If the 2–20 keV spectrum is better characterized by a power law, then the temperature obtained from a thermal model fit from each instrument would yield a temperature characteristic of the instrumental bandpass, which is exactly the case here. Thus, a thermal bremsstrahlung model is inconsistent with the ASCA and GINGA observations taken together.

Inverse Compton One possibility discussed by WAHK is that X-rays are produced by inverse-Compton scattering of infrared photons off electrons. Gaisser, Protheroe, & Stanev (1998) found that an inverse-Compton component, scattering off the microwave background, would have a photon index of Γ=1.5. On the other hand, if the scattering photons were locally produced, one would expect the hard X-ray emission to arise from IR-bright regions. The localization of the hard X-ray emission a restricted region, the brightest part of which has no IR counterpart argues against an inverse-Compton origin.

Accelerated Bremsstrahlung It has been suggested that electrons accelerated in the shock to MeV energies may be responsible for the generation of hard X-rays via bremsstrahlung in supernova remnants (Sturner et al. 1995; Asarov, Guseinov, & Kasumov 1990). The fact that the radio spectral index around the hard X-ray feature is flatter than elsewhere in IC 443 is strong evidence against this mechanism. If we assume that the same acceleration mechanism produces both the MeV and the GeV electrons (responsible for the radio emission), then there will be fewer MeV electrons in the hard region than elsewhere in the remnant. Thus, if this mechanism were operating efficiently, this region would be *dimmer* in hard X-rays than everywhere else in the

remnant.

Synchrotron Radiation The most straightforward mechanism for producing a power law X-ray spectrum is synchrotron radiation. None of the observations contradict this interpretation; all are consistent with it. In particular, the fact that the radio spectrum of this region is flatter than elsewhere argues that at higher energies (including the X-ray band), the synchrotron flux will be enhanced over elsewhere in the SNR. In fact, as we show below, the physical size of the HXF corresponds well with the synchrotron loss time of X-ray producing electrons.

WAHK dismissed synchrotron emission as a likely model, because an acceleration mechanism efficient enough to accelerate electrons to $\sim$10 TeV seemed unlikely and they calculated synchrotron loss times to be less than the age of the SNR. Their dismissal was based on the assumption that the hard X-ray emission is spatially uniform; we now know from this ASCA observation that the hard emission arises primarily from localized regions.

X-ray synchrotron emission in a SNR can be produced by high energy electrons accelerated and interacting with a magnetic field in one of two locations: the magnetosphere of a pulsar (giving rise to a plerion) or the forward shock of a SNR. The observations support both interpretations to some extent, but more issues arise from the presence of a plerion than from an isolated region of intense shock acceleration.

The compact size of the hard X-ray feature is the primary evidence in favor of a plerionic interpretation. The lack of X-ray pulsations is not necessarily a problem: the upper limit on the pulsed fraction is higher than other pulsars like Vela (Pravdo et al. 1976). Nor is the existence of extended emission without an obvious embedded point source unprecedented: the SNR 3C 58 has a small extent, a power law spectrum and shows no pulsations, but is generally regarded as a plerion (Helfand, Becker, & White 1995).

Difficulties with the interpretation arise when trying to associate a plerion with IC 443. Wilson (1986) has shown that the median X-ray:radio $\left(\frac{0.5\text{–}3.5\ \mathrm{keV}}{10^{7}\text{–}10^{11}\ \mathrm{Hz}}\right)$ flux ratio for plerions is about 1, with a range from about 0.1–500. The flux ratio of the HXF is about 900, which would give it the highest known X-ray:radio flux ratio of any plerion.

Furthermore, if the feature is a plerion associated with the IC 443 shell it requires an extremely high projected velocity of $5,000\left(\frac{d}{1.5\,\mathrm{kpc}}\right)\left(\frac{\theta}{10'}\right)\left(\frac{t}{1000\,\mathrm{yr}}\right)\ \mathrm{km\,s^{-1}}$, for distance d, angular distance θ from the explosion center, and age t. IC 443 is in a complex region of interstellar space, and the diffuse emission is thought to the product of multiple supernova events (AA94). The proper motion problem is circumvented if the hard X-ray feature represents the site of the most recent explosion which we can take from Chinese records to have occurred in A.D. 837 (WAHK). If that were the case, then it is surprising that this explosion has apparently not affected the temperature or surface brightness distribution of the diffuse emission. The former suggests a more centrally located explosion; the latter an explosion in the northeastern quadrant of the SNR.

On the other hand, the presence around the hard feature of many interesting structures associated with collisions between the shock front and concentrations of material suggests the hard X-ray emission is related to them. In particular, shock/cloud collisions can locally enhance particle acceleration (JK93). We consider first whether shock acceleration is a plausible source of the hard X-rays, and then how the morphology of the feature might arise.

Dickel & Milne (1976) found Faraday rotation measures in IC 443 of about 200 rad $\mathrm{m^{-2}}$ where the field is along the line of sight, and close to zero where it is perpendicular. Taking the density and path length measurements from the X-ray (PSSW), we estimate the magnetic field strength B to be:

$$B \approx 1.23 \times \left(\frac{200\ \mathrm{rad\,m^{-2}}}{5\,\mathrm{cm^{-3}} \times 0.1\,\mathrm{pc}}\right) \approx 500\,\mu\mathrm{G} \tag{8.1}$$

The synchrotron photon/electron energy relation therefore can be written:

$$E_{\rm photon} \approx 5 \text{ keV} \times \frac{B}{500\ \mu\text{G}} \times (\frac{E_e}{20 \text{ TeV}})^2 \,, \tag{8.2}$$

where $E_{\rm photon}$ is the observed photon energy produced as synchrotron radiation from an electron at energy E_e. So while radio emission ($E_{\rm photon} \approx 10^{-9}$ keV) is produced by GeV electrons, production of 5 keV X-rays requires the presence of ~20 TeV electrons.

In attempting to explain the non-thermal component dominating the X-ray emission from SN 1006 as synchrotron emission from highly relativistic electrons, Anderson & Rudnick (1996) has shown that it is possible to accelerate electrons (and ions) in SNR shocks to energies exceeding 100 TeV. While his model is not strictly applicable here, some aspects of it can be used to establish the plausibility of shock accelerated electrons as the source of the hard X-ray emission in IC 443.

In the simplest models, the synchrotron spectrum is expected to be a broken power law. The various break frequencies correspond to electron energies where two canonical times scales equate, such as the synchrotron loss time and the acceleration time scale. At each break, the spectral index increases by about 0.5. The electron diffusion time is also important in determining the steepening of the spectrum, but its influence is less straightforward to estimate.

In the IC 443 hard feature, the difference between the radio and the X-ray spectral index is approximately 1.1, suggesting the need for at least two spectral breaks between the bands. The time it takes for an electron of energy E to lose half its energy via synchrotron radiation in a magnetic field of strength B is given by:

$$\tau_{\rm loss} = \left(\frac{500\ \mu\text{G}}{B}\right)^2 \left(\frac{20 \text{ TeV}}{E_e}\right) \times 2.5 \text{ years} \,, \tag{8.3}$$

which is approximately the light crossing time of the HXF. Using Equations 8.3 and 8.2, and assuming a SNR age between 1000 and 5000 yr (WAHK, AA94), we find that the break frequency where the synchrotron loss time becomes comparable to the age of the SNR occurs in the far infrared. Additionally, by assuming a shock velocity on

the order of 1000 km s^{-1}, we find the break frequency associated with the equivalence between the acceleration and loss times is in the hard ultraviolet band. The frequencies at which these two spectral breaks occur supports the idea that the flat radio and the hard X-ray spectra are both produced by shock acceleration.

While Reynolds' (1996) formalism facilitates the plausibility argument above and is especially suggestive with regard to the ridge region, his models for producing X-rays from shock accelerated electrons from a large segment of the SNR shell clearly do not apply to the HXF in IC443. A different mechanism must be operating there. Such a mechanism has been suggested by JK93.

Figure 8.2 shows BGBW's H_2 image of shocked molecular gas. This shows that the molecular cloud has a clumpy ring structure exterior to the site of the supernova event. Dickman *et al.* (1992) found that if the ring is circular, it must be inclined $\sim 51°$ from the line of sight and have a diameter of ~ 9 pc. Doppler shift information shows the southern edge of the ring (near our HXF) expanding toward us, and the northern edge away – implying that the ring is now expanding at a deprojected velocity of 25 km/s. While, we agree with this picture in principle, we point out that to second order the ring is not circular; most noticeably there is a section of negative curvature surrounding the HXF (Fig. 8.2). It is this change of curvature that may create the HXF.

JK93 simulated cosmic-ray acceleration as shocks impact dense clouds – which is the case here. They found that after a shock/cloud impact, particle acceleration is significantly enhanced in the "tail shock" emanating from the cloud in the direction of shock propagation. Their results suggest that each clump in the molecular ring could produce enhanced shock acceleration in a long tail behind it. Because of the negative curvature of one section of the ring, the flow will be refracted, thereby "focusing" the enhanced shock acceleration at the hard X-ray feature where the tail shocks overlap. This interaction between these tail shocks will both increase the effective shock velocities and provide a complicated structure which will require further study.

The total hard flux from the diffuse emission along the shell (the ridge) is about half that from the HXF, but the ridge may extend out of the field of view. It corresponds to an arc bright in H_2, and radio continuum. While we cannot yet be certain that the emission in non-thermal, the higher ambient density as indicated by the infrared line emission argues that the temperature of shock-heated material should be lower than elsewhere in IC 443 - not higher. The arguments made above for the HXF against emission mechanisms other than synchrotron hold for the ridge region as well. While we withhold judgment until a higher quality spectrum can be obtained, we suggest that we are seeing evidence here as well for TeV electrons. Whether these arise from the JK93 mechanism or are more closely related to the forward shock is still an open question.

8.4 Conclusion

In this paper we have presented evidence for a localized region of particle acceleration to electron energies over 20 TeV, within the shell type supernova remnant IC 443. Because of the unique positions of the hard X-ray feature and shocked clouds, we believe that the HXF is caused by the focusing of tail shocks around each molecular cloud, thus enhancing particle acceleration in this location. In addition we have found a ridge of hard emission which in coincident with both the radio-synchrotron shell and shocked molecular gas, but whose spectral parameters are poorly constrained.

More observational and theoretical research is needed to fully understand this phenomenon. Multi-frequency and polarization observations with the VLA will allow us to both measure the feature's spectral index and look for other indicators of on-going particle acceleration. A deep single-dish radio observation of this area is necessary to verify that the HXF is indeed non-plerionic. The most important future observation will be to observe the full extent of the ridge and the shocked molecular gas with ASCA to better characterize the spectrum and image the full extent of the hard non-thermal

emission.

On the theoretical side, this discovery provides a nice opportunity to model particle acceleration and cloud/shock interactions with significant observational constraints.

We thank the following people for contributing to these results: Richard Mushotzky for bringing the hard feature to our attention; Michael Burton for kindly providing his H_2 emission line image in digitized form; Steve Reynolds and Tom Jones for their insights into shock acceleration; Matthew Baring and Ocker de Jager for their thoughtful comments and suggestions.

Appendix A

The X-ray Observatories

This thesis uses data from three X-ray observatories (ROSAT, ASCA and RXTE). Each of these missions are well-documented on the World Wide Web*, so this *appendix* will not attempt to thoroughly describe each observatory. However, Tab. A.1 compares a few of their basic features. ROSAT has the best soft X-ray imaging capabilities, so it was used to map the thermal emission from Cas A in PART I. ASCA and RXTE, having harder bandpasses, were used to search for non-thermal emission in PART II.

Mission	ROSAT		ASCA		RXTE	
Instruments	HRI	PSPC	SIS	GIS	PCA	HEXTE
Energy Range	0.1–2.5		0.1–10 keV	0.5–12 keV	2–50 keV	25–250
Angular Res.	2″	30″	1′	2′	1°	1°
Spectral Res.	100%	50%	2%	8%	18%	15%
Launch Date	June 1, 1990		Feb. 20, 1993		Dec. 30, 1995	

Table A.1: A quick comparison of three X-ray observatories. All the values in this table are rough estimates and should be taken as such — in fact most are energy dependent so these are simply basic estimates. Notice how ROSAT's strength is imaging, ASCA's strength is spectroscopy, and RXTE's strength is its hard bandpass.

*Information about the X-ray missions can be found at `http://heasarc.gsfc.nasa.gov/`

Appendix B

A Basic Introduction to X-ray Spectroscopy

The results presented in PART II of this thesis rely primarily on data from the Gas Imaging Spectrometer (GIS) on board ASCA. This purpose of this section is not to describe this instrument, but rather to give the reader a basic feel for how to interpret X-ray spectroscopic results, using the ASCA GIS as the example instrument.

Essentially the GIS counts photons as they arrive, measuring each one's energy and incident direction. The observer later can select out photons based on a set of criteria. For example, one might make an image by creating a histogram of counts on a sky coordinate grid, or a spectrum by creating another histogram as a function of photon energy.

Practically, the astronomer makes an image, then defines the source region and then makes a spectrum of only the photons within that region. In addition, if the source is small enough, then a background region is defined, and a background spectrum is selected. If, on the other hand, the source fills the field of view, then a standard background must be used. The background spectrum is naturally subtracted from the source spectrum before a model can be fit to it.

The sensitivity of X-ray spectrometers, such as the ASCA GIS, vary over their wavelength range. This *response function* is carefully measured and is now well known for ASCA. Emission models must be *folded* through the response function before they can be compared to the data. The bottom plot in each of the figures B.1–B.6 is this *folded* spectrum. In general, folded spectra show best how well the model fits the data.

Alternatively, the data can be *unfolded* back through the response function to be compared with the model. This *unfolded* spectrum shows the model in real flux density units (i.e. photons $cm^{-2} s^{-1} keV^{-1}$), and each term in the overall model is plotted separately on the unfolded spectra, so one can easily see the relative importance of each component. Note that these terms represent absorbed model components, so each term in the real spectrum (e.g., those in chapter 7) falls off toward low energies. However the *unfolding* process is less robust than the *folding* process, so close comparisons between the model and data are not advised with unfolded spectra.

In order to give the reader a feel for folded X-ray spectra, I have plotted model spectra, and corresponding simulated ASCA observations.

Figs. B.1–B.4 show equilibrium thermal spectra (Raymond & Smith 1977). Notice how the ASCA GIS cannot resolve each emission line, so nearby line ratios are not a viable temperature or metallicity diagnostic.

Fig. B.5, on the other hand, shows a model synchrotron spectrum like those used in chapter 7 (Reynolds 1998). Notice the difference in curvature between the model and the simulated ASCA spectrum – – as the effective area changes with photon energy.

Fig. B.6 shows the same model as plotted in Fig. B.5, but absorbed with a typical interstellar column density, using the standard absorption model (Morrison & McCammon 1983). Notice how much structure is produced by the changing transparency of the ISM at the softer energies.

The overall purpose of this appendix is two fold:

- To provide the reader the basic skills needed to interpret ASCA spectra, such as

how to interpret a folded spectrum.

- To show the reader how simple plasmas appear as a function of parameters such as metallicity, temperature and absorption.

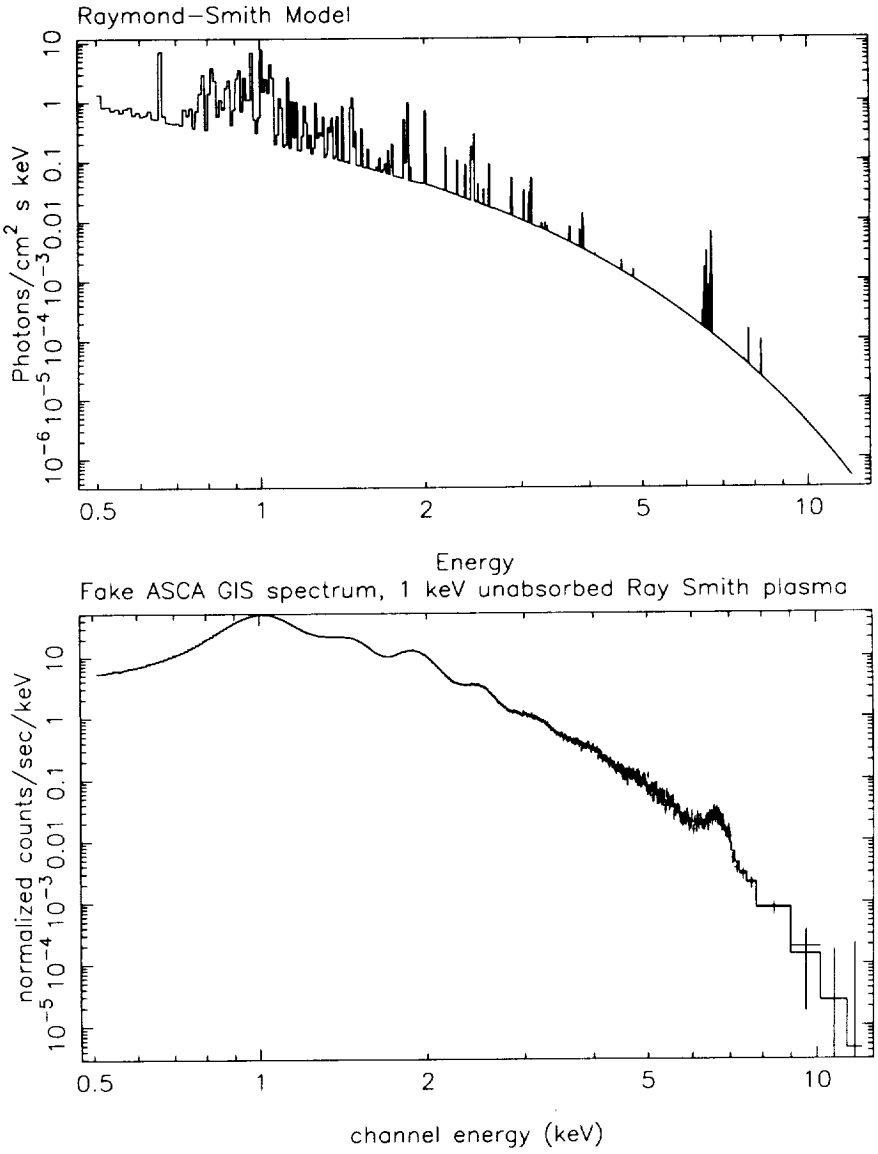

Figure B.1: A 1 keV model Raymond-Smith plasma (top) assuming solar abundances and a simulated ASCA spectrum of the same model (bottom).

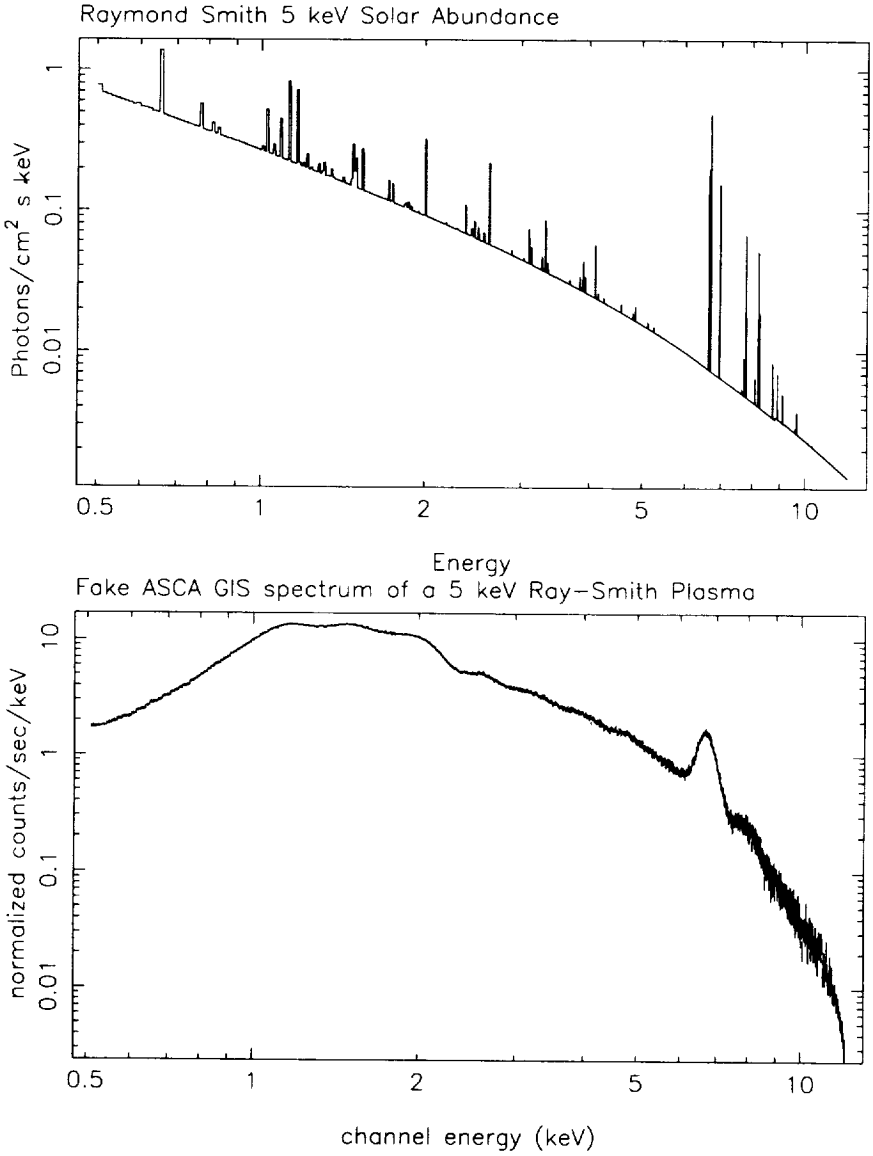

Figure B.2: A 5 keV model Raymond-Smith plasma (top) assuming solar abundances and a simulated ASCA spectrum of the same model (bottom).

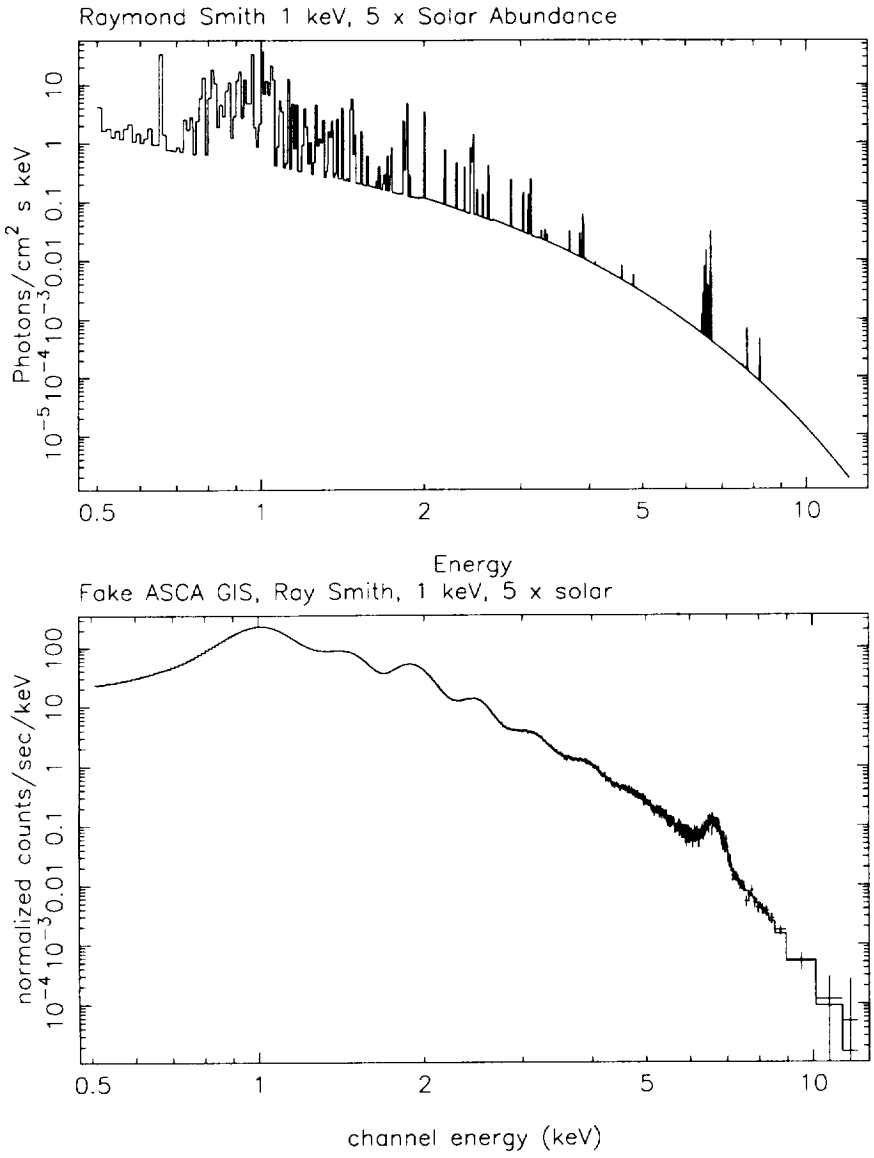

Figure B.3: A 1 keV model Raymond-Smith plasma (top) assuming 5× solar abundances and a simulated ASCA spectrum of the same model (bottom).

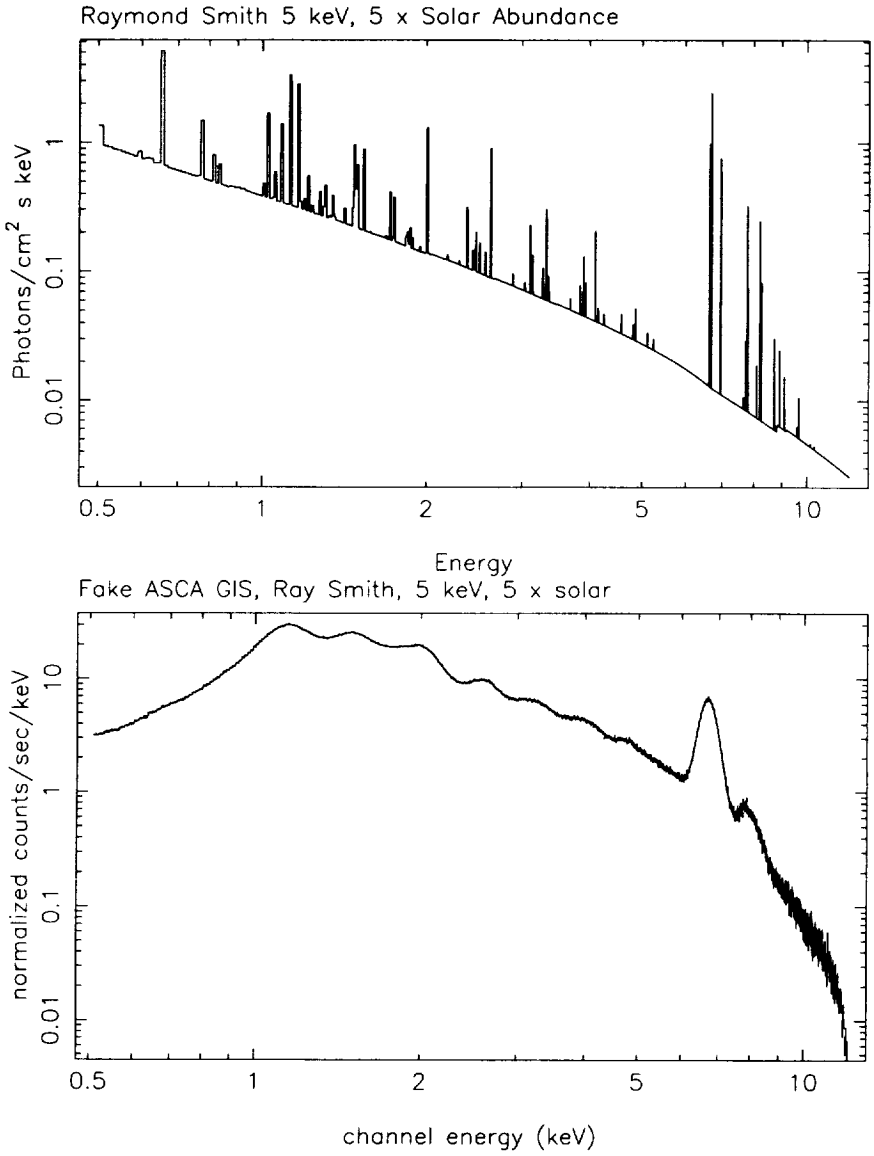

Figure B.4: A 5 keV model Raymond-Smith plasma (top) assuming 5× solar abundances and a simulated ASCA spectrum of the same model (bottom).

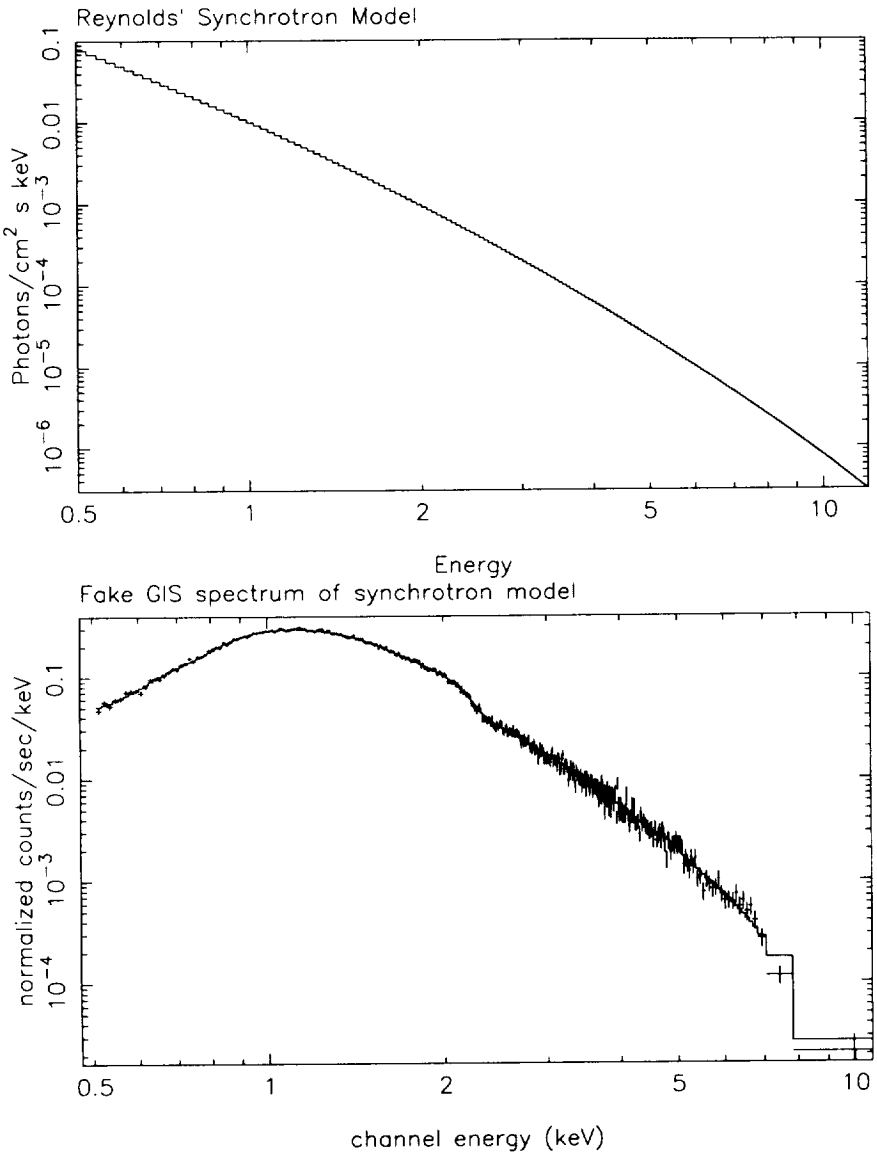

Figure B.5: Synchrotron plasma assuming a 1 GHz flux density of 1 Jy and a break frequency of 1×10^{16} Hz (top) and a simulated ASCA spectrum of the same model (bottom).

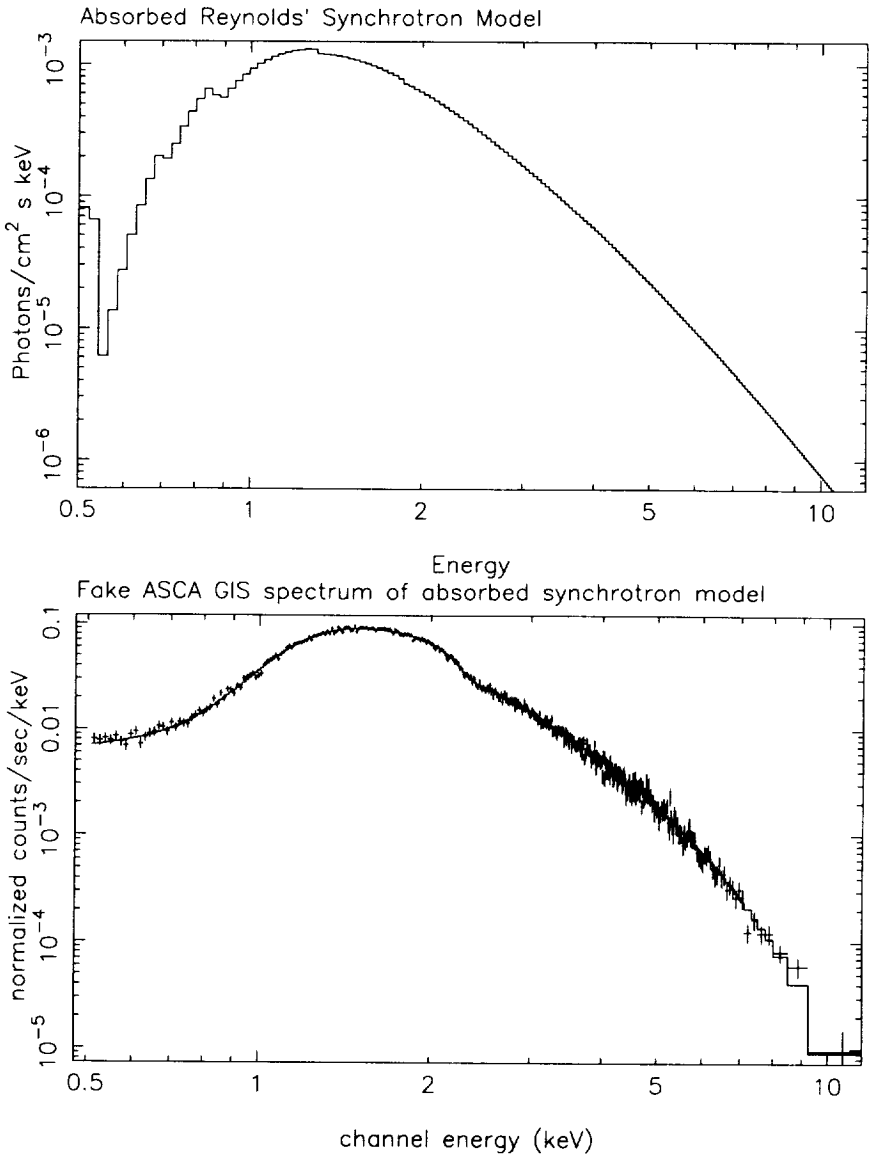

Figure B.6: An synchrotron plasma like in figure B.5, but absorbed with an effective hydrogen column density of $10^{22}\,\mathrm{cm}^{-1}$, and a simulated ASCA spectrum of the same model (bottom).

Bibliography

Allen, G. E., Berley, D., Biller, S., Burman, R. L., Cavalli-Sforza, M., Chang, C. Y., Chen, M. L., Chumney, P., Coyne, D., Dion, C. L., Dorfan, D., Ellsworth, R. W., Goodman, J. A., Haines, T. J., Hoffman, C. M., Kelley, L., Klein, S., Schmidt, D. M., Schnee, R., Shoup, A., Sinnis, C., Stark, M. J., Williams, D. A., Wu, J. P., Yang, T., & Yodh, G. B. 1995, ApJ, 448, L25

Allen, G. E., Keohane, J. W., Gotthelf, E. V., Petre, R., Jahoda, K., Rothschild, R. E., Lingenfelter, R. E., Heindl, W. A., Marsden, D., Gruber, D. E., Pelling, M. R., & Blanco, P. R. 1997, ApJ, 487, L97

Ammosov, A. E., Ksenofontov, L. T., Nikolaev, V. S., & Petukhov, S. I. 1994, Astr. Letters, 22, 157

Anantharamaiah, K. R., Erickson, W. C., Payne, H. E., & Kantharia, N. G. 1994, ApJ, 430, 682–689

Anderson, M. C., & Rudnick, L. 1993, ApJ, 408, 514–529

Anderson, M. C., & Rudnick, L. 1995, ApJ, 441, 307–333

Anderson, M. C., & Rudnick, L. 1996, ApJ, 456, 234

Anderson, M. C., Jones, T. W., Rudnick, L., Tregillis, I. L., & Kang, H. 1994, ApJ, 421, L31–L34

Arendt, R. G., Dwek, E., Petre, R., Dickel, J. R., Roger, R. S., Milne, D. K., & Kesteven, M. J. 1990, ApJ, 350, 266–274

Asaoka, I., & Aschenbach, B. 1994, A&A, 284, 573–582

Asarov, A. I., Guseinov, O. H., & Kasumov, F. K. Dogel, V. A. 1990, A&A, 229, 196–200

Ashworth, Jr., W. B. 1980, J. for the History of Astronomy, 11, 1

Axford, W. I. 1992. Particle acceleration on Galactic scales. In Particle acceleration in cosmic plasmas; Proceedings of the Workshop, Bartol Research Inst., Newark, DE, Dec. 4-6, 1991 (A93-39976 16-93), p. 45-56., pages 45–56

Axford, W. I. 1994, ApJS, 90, 937–944

Baars, J. W. M., Genzel, R., Pauliny-Toth, I. I. K., & Witzel, A. 1977, A&A, 61, 99–106

Baring, M., Ellison, D., Grenier, I., & Goret, P. 1998, ApJ *submitted*

Bassett, G. M., & Woodward, P. R. 1995, ApJ, 441, 582–602

Batrla, W., Walmsley, C. M., & Wilson, T. L. 1984, A&A, 136, 127–132

Becker, R. H., Smith, B. W., White, N. E., Holt, S. S., Boldt, E. A., Mushotzky, R. F., & Serlemitsos, P. J. 1979, ApJ, 234, L73–L76

Becker, R. H., Markert, T., & Donahue, M. 1985, ApJ, 296, 461–468

Bell, A. R. 1978, MNRAS, 182, 147–156

Bevington, P. R., & Robinson, D. K. 1992. *Data Reduction and Error Analysis in the Physical Sciences*, McGraw-Hill, Inc., second edition

Bieging, J. H., & Crutcher, R. M. 1986, ApJ, 310, 853–871

Bieging, J. H., Goss, W. M., & Wilcots, E. M. 1991, ApJS, 75, 999–1010

Biermann, P. L. 1995, Space Science Reviews, v. 74, p. 385-396., 74, 385–396

Blandford, R., & Eichler, D. 1987, Phys. Rep., 154, 1

Blandford, R. D., & Ostriker, J. P. 1978, ApJ, 221, L29–L32

Borkowski, K., Szymkowiak, A. E., Blondin, J. M., & Sarazin, C. L. 1996, ApJ, 466, 866

Borkowski, K. J., Blondin, J. M., & Sarazin, C. L. 1992, ApJ, 400, 222–237

Borkowski, K. J., Sarazin, C. L., & Blondin, J. M. 1994, ApJ, 429, 710–725

Brahe, T. 1573. *De Nova Stella*

Braun, R. 1987, A&A, 171, 233–251

Brinkmann, W., Fink, H. H., Smith, A., & Haberl, F. 1989, A&A, 221, 385–395

Burton, M. G., Geballe, T. R., Brand, P. W. J. L., & Webster, A. S. 1988, MNRAS, 231, 617–634

Burton, M. G., Hollenbach, D. J., Haas, M. R., & Erickson, E. F. 1990, ApJ, 355, 197–209

Chevalier, R. A. 1982, ApJ, 258, 790–797

Clark, D. H., & Stephenson, F. R. 1977. *The Historical Supernovae*, Pergamon, Oxford

Cliffe, J. A., & Jones, T. W. 1994, BAAS, 184, #41.07, 184, 4107

Cowsik, R., & Sarkar, S. 1980, MNRAS, 191, 855–861

Decourchelle, A., & Ballet, J. 1994, A&A, 287, 206–218

Denoyer, L. K. 1979, ApJ, 232, L165–L168

Dickel, J. R., & Milne, D. K. 1976, Australian Journal of Physics, 29, 435–460

Dickel, J. R., Murray, S. S., Morris, J., & Wells, D. C. 1982, ApJ, 257, 145–150

Dickel, J. R., Eilek, J. A., Jones, E. M., & Reynolds, S. P. 1989, ApJS, 70, 497–538

Dickel, J. R., Van Breugel, W. J. M., & Strom, R. G. 1991, AJ, 101, 2151–2159

Dickman, R. L., Snell, R. L., Ziurys, L. M., & Huang, Y.-L. 1992, ApJ, 400, 203–213

Dohm-Palmer, R. C., & Jones, T. W. 1996, ApJ, 471, 279

Drury, L. O., Aharonian, F. A., & Voelk, H. J. 1994, A&A, 287, 959–971

Dyer, K. K., & Reynolds, S. P. 1998, *in preparation*

Ellison, D. C., Reynolds, S. P., Borkowski, K., Chevalier, R., Cox, D. P., Dickel, J. R., Pisarski, R., Raymond, J., Spangler, S. R., Volk, H. J., & Wefel, J. P. 1994, PASP, 106, 780–797

Esposito, J. A., Hunter, S. D., Kanbach, G., & Sreekumar, P. 1996, ApJ, 461, 820

Fabian, A. C., Willingale, R., Pye, J. P., Murray, S. S., & Fabbiano, G. 1980, MNRAS, 193, 175–188

Favata, F., Vink, J., Dal Fiume, D., Parmar, A. N., Santangelo, A., Mineo, T., Preite-Martinez, A., Kaastra, J. S., & Bleeker, J. A. M. 1997, A&A, 324, L49–L52

Fermi, E. 1949, Physical Review, 75, 1169–1174

Fesen, R. A., Becker, R. H., & Goodrich, R. W. 1988, ApJ, 329, L89–L92

Frail, D. A., Goss, W. M., Reynoso, E. M., Giacani, E. B., Green, A. J., & Otrupcek, R. 1996, AJ, 111, 1651

Fujimoto, R., Tanaka, Y., Inoue, H., Ishida, M., Itoh, M., Mitsuda, K., Sonobe, T., Tsunemi, H., Murakami, H., Koyama, K., Hayashi, I., Ikeda, K., Rasmussen, A., Ricker, G., & Becker, C. M. 1995, PASJ, 47, L31

Gaisser, T. K., Protheroe, R. J., & Stanev, T. 1998, ApJ, 492, 219

Gaume, R. A., Wilson, T. L., & Johnston, K. J. 1994, ApJ, 425, 127–131

Goss, W. M., Kalberla, P. M. W., & Dickel, H. R. 1984, A&A, 139, 317–329

Gotthelf, E. V., & Vasisht, G. 1997, ApJ, 486, L133

Gotthelf, E. V., Petre, R., & Hwang, U. 1997, ApJ, 487, L175

Green, D. A. 1986, MNRAS, 221, 473–482

Green, D. A. 1988, Ap&SS, 148, 3–74

Green, D. A., Gull, S. F., Tan, S. M., & Simon, A. J. B. 1988, MNRAS, 231, 735–738

Gull, S. F. 1973a, MNRAS, 162, 135

Gull, S. F. 1973b, MNRAS, 161, 47

Hamilton, A. J. S., Chevalier, R. A., & Sarazin, C. L. 1983, ApJS, 51, 115–147

Hamilton, A. J. S., Sarazin, C. L., & Szymkowiak, A. E. 1986a, ApJ, 300, 698–712

Hamilton, A. J. S., Sarazin, C. L., & Szymkowiak, A. E. 1986b, ApJ, 300, 713–721

Helfand, D. J., Becker, R. H., & White, R. L. 1995, ApJ, 453, 741

Holt, S. S., Gotthelf, E. V., Tsunemi, H., & Negoro, H. 1994, PASJ, 46, L151–L155

Hughes, J. P., & Helfand, D. J. 1985, ApJ, 291, 544–560

Hwang, U., & Gotthelf, E. V. 1997, ApJ, 475, 665

Hwang, U., Hughes, J. P., & Petre, R. 1998, ApJ, 497, 833

Isobe, T., Feigelson, E. D., Akritas, M. G., & Babu, G. J. 1990, ApJ, 364, 104–113

Jansen, F., Smith, A., Bleeker, J. A. M., De Korte, P. A. J., Peacock, A., & White, N. E. 1988, ApJ, 331, 949–957

Jones, T. W., & Kang, H. 1993, ApJ, 402, 560–573

Jones, T. W., Kang, H., & Tregillis, I. L. 1994, ApJ, 432, 194–206

Jun, B. I. 1995. Numerical Modeling of Radio Emission from Young Supernova Remnants. Ph.D. thesis, University of Illinois

Jun, B. I., & Norman, M. L. 1995, Ap&SS, 233, 267–272

Jun, B.-I., & Norman, M. L. 1996a, ApJ, 472, 245

Jun, B.-I., & Norman, M. L. 1996b, ApJ, 465, 800

Jun, B.-I., Norman, M. L., & Stone, J. M. 1995, ApJ, 453, 332

Kalberla, P. M. W., Schwarz, U. J., & Goss, W. M. 1985, A&A, 144, 27–36

Keohane, J. W., Rudnick, L., & Anderson, M. C. 1996, ApJ, 466, 309

Keohane, J. W., Petre, R., Gotthelf, E. V., Ozaki, M., & Koyama, K. 1997, ApJ, 484, 350

Kepler, J. 1606. *De Stella Nova*

Koralesky, B. T., & Rudnick, L. 1998, *in preparation*

Koyama, K., Petre, R., Gotthelf, E. V., Hwang, U., Matsura, M., Ozaki, M., & Holt, S. S. 1995, Nature, 378, 255

Koyama, K., Kinugasa, K., Matsuzaki, K., Nishiuchi, M., Sugizaki, M., Torii, K., Yamauchi, S., & Aschenbach, B. 1997, PASJ, 49, L7–L11

Lacey, C., Duric, N., & Goss, W. M. 1997, ApJS, 109, 417

Laming, J. M. 1998, ApJ, 499, 309

Lasker, B. M., Sturch, C. R., McLean, B. J., Russell, J. L., Jenkner, H., & Shara, M. M. 1990, AJ, 99, 2019–2058

Lozinskaya, T. 1992. *Supernovae and Stellar Wind in the Interstellar Medium*, New York : American Institute of Physics ©1992

Lucy, L. B. 1974, AJ, 79, 745

Malagoli, A., Bodo, G., & Rosner, R. 1996, ApJ, 456, 708

Marschall, L. A. 1988. *The Supernova Story*, Plenum Press

Masai, K. 1994, ApJ, 437, 770–780

Matsui, Y., Long, K. S., Dickel, J. R., & Greisen, E. W. 1984, ApJ, 287, 295–306

Mebold, U., & Hills, D. L. 1975, A&A, 42, 187–194

Miyata, E., Tsunemi, H., Pisarski, R., & Kissel, S. E. 1994, PASJ, 46, L101–L104

Morrison, R., & McCammon, D. 1983, ApJ, 270, 119–122

Payne, H. E., Anantharamaiah, K. R., & Erickson, W. C. 1994, ApJ, 430, 690–705

Petre, R., Szymkowiak, A. E., Seward, F. D., & Willingale, R. 1988, ApJ, 335, 215–238

Petre, R., Hwang, U., Keohane, J. W., & Gotthelf, E. V. 1997, American Astronomical Society Meeting, 191, 4002

Pier, E. A. 1997. *ASCA Getting Started Guide for Revision 2 Data: Version 6.1.* The ASCA Processing Team, Code 631, NASA/Goddard Space Flight Center, Greenbelt, MD 20771, `http://adfwww.gsfc.nasa.gov/asca/ascaDF.html`

Pravdo, S. H., Becker, R. H., Boldt, E. A., Holt, S. S., Rothschild, R. E., Serlemitsos, P. J., & Swank, J. H. 1976, ApJ, 206, L41–L44

Torii, K., Tsunemi, H., Dotani, T., & Mitsuda, K. 1997, ApJ, 489, L145

Troland, T. H., Crutcher, R. M., & Heiles, C. 1985, ApJ, 298, 808–817

Tuffs, R. J. 1986, MNRAS, 219, 13–38

Van Dishoeck, E. F., Jansen, D. J., & Phillips, T. G. 1993, A&A, 279, 541–566

Vancura, O., Gorenstein, P., & Hughes, J. P. 1995, ApJ, 441, 680–688

Vasisht, G., & Gotthelf, E. V. 1997, ApJ, 486, L129

Vasisht, G., Aoki, T., Dotani, T., Kulkarni, S. R., & Nagase, F. 1996, ApJ, 456, L59

Wang, Z. R., Asaoka, I., Hayakawa, S., & Koyama, K. 1992, PASJ, 44, 303–308

Wang, Z. R., Qu, Q. Y., & Chen, Y. 1997, A&A, 318, L59–L61

Wilson, A. S. 1986, ApJ, 302, 718–726

Wilson, T. L., & Mauersberger, R. 1994, A&A, 282, L41–L44

Wilson, T. L., Mauersberger, R., Muders, D., Przewodnik, A., & Olano, C. A. 1993, A&A, 280, 221–230

Woosley, S. E., & Weaver, T. A. 1986, ARA&A, 24, 205–253

Index